TOWARDS THE APPLICATION OF THE ISOGEOMETRIC BOUNDARY ELEMENT ANALYSIS TO FLUID MECHANICS: NON-LINEAR GRAVITY WAVES AND DYNAMICS OF DEFORMABLE CAPSULES IN SHEAR FLOWS

Jorge Maestre Heredia

UNIVERSITAT ROVIRA I VIRGILI
TOWARDS THE APPLICATION OF THE ISOGEOMETRIC BOUNDARY ELEMENT ANALYSIS TO FLUID MECHANICS:
NON-LINEAR GRAVITY WAVES AND DYNAMICS OF DEFORMABLE CAPSULES IN SHEAR FLOWS
Jorge Maestre Heredia

UNIVERSITAT ROVIRA i VIRGILI

TOWARDS THE APPLICATION OF THE ISOGEOMETRIC BOUNDARY ELEMENT ANALYSIS TO FLUID MECHANICS: NON-LINEAR GRAVITY WAVES AND DYNAMICS OF DEFORMABLE CAPSULES IN SHEAR FLOWS

JORGE MAESTRE HEREDIA

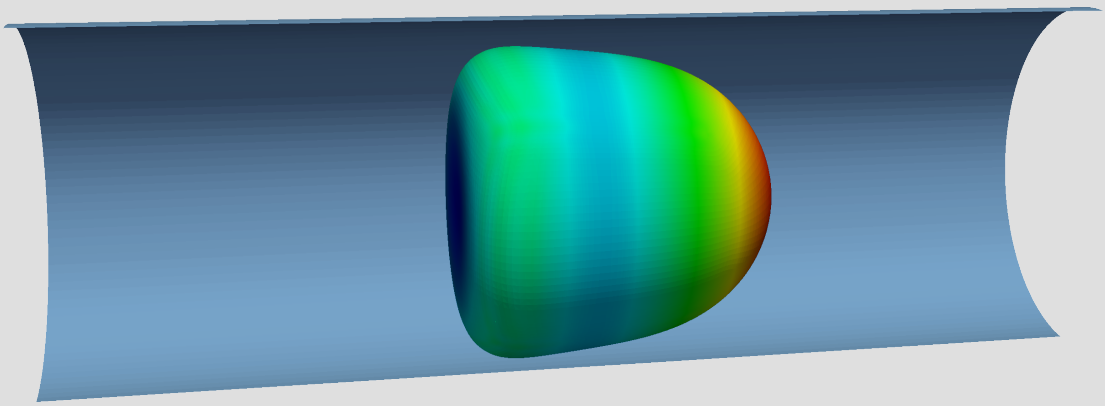

DOCTORAL THESIS

2016

UNIVERSITAT ROVIRA I VIRGILI
TOWARDS THE APPLICATION OF THE ISOGEOMETRIC BOUNDARY ELEMENT ANALYSIS TO FLUID MECHANICS:
NON-LINEAR GRAVITY WAVES AND DYNAMICS OF DEFORMABLE CAPSULES IN SHEAR FLOWS
Jorge Maestre Heredia

UNIVERSITAT ROVIRA I VIRGILI
TOWARDS THE APPLICATION OF THE ISOGEOMETRIC BOUNDARY ELEMENT ANALYSIS TO FLUID MECHANICS:
NON-LINEAR GRAVITY WAVES AND DYNAMICS OF DEFORMABLE CAPSULES IN SHEAR FLOWS
Jorge Maestre Heredia

UNIVERSITAT ROVIRA I VIRGILI
TOWARDS THE APPLICATION OF THE ISOGEOMETRIC BOUNDARY ELEMENT ANALYSIS TO FLUID MECHANICS:
NON-LINEAR GRAVITY WAVES AND DYNAMICS OF DEFORMABLE CAPSULES IN SHEAR FLOWS
Jorge Maestre Heredia

Jorge Maestre Heredia

TOWARDS THE APPLICATION OF THE ISOGEOMETRIC BOUNDARY ELEMENT ANALYSIS TO FLUID MECHANICS: NON-LINEAR GRAVITY WAVES AND DYNAMICS OF DEFORMABLE CAPSULES IN SHEAR FLOWS

Doctoral Thesis

Supervised by:
Dr. Jordi Pallarès
Dr. Ildefonso Cuesta

Department of Mechanical Engineering

Tarragona 2016

UNIVERSITAT ROVIRA i VIRGILI

UNIVERSITAT ROVIRA I VIRGILI
TOWARDS THE APPLICATION OF THE ISOGEOMETRIC BOUNDARY ELEMENT ANALYSIS TO FLUID MECHANICS:
NON-LINEAR GRAVITY WAVES AND DYNAMICS OF DEFORMABLE CAPSULES IN SHEAR FLOWS
Jorge Maestre Heredia

UNIVERSITAT ROVIRA I VIRGILI

Dr. Jordi Pallarès and Dr. Ildefonso Cuesta, Professors of the Mechanical Engineering Department of Universitat Rovira i Virgili,

CERTIFY:

That the present study, entitled:

TOWARDS THE APPLICATION OF THE ISOGEOMETRIC BOUNDARY ELEMENT ANALYSIS TO FLUID MECHANICS: NON-LINEAR GRAVITY WAVES AND DYNAMICS OF DEFORMABLE CAPSULES IN SHEAR FLOWS

presented by Jorge Maestre Heredia for the award of the degree of Doctor, has been carried out under our supervision at the Department of the Mechanical Engineering of this university and it fulfils all requirements to be eligible for the International Mention Award.

And, to inform you of that and in order for it to have the needed effects, we sign this certification

Tarragona, 25th November, 2016

Dr. Jordi Pallarès

Dr. Ildefonso Cuesta

UNIVERSITAT ROVIRA I VIRGILI
TOWARDS THE APPLICATION OF THE ISOGEOMETRIC BOUNDARY ELEMENT ANALYSIS TO FLUID MECHANICS:
NON-LINEAR GRAVITY WAVES AND DYNAMICS OF DEFORMABLE CAPSULES IN SHEAR FLOWS
Jorge Maestre Heredia

Contents

UNIVERSITAT ROVIRA I VIRGILI
TOWARDS THE APPLICATION OF THE ISOGEOMETRIC BOUNDARY ELEMENT ANALYSIS TO FLUID MECHANICS:
NON-LINEAR GRAVITY WAVES AND DYNAMICS OF DEFORMABLE CAPSULES IN SHEAR FLOWS
Jorge Maestre Heredia

Abstract

In this Thesis an efficient and robust numerical model for the analysis of fluid dynamic problems has been developed, validated and applied to two novel fluid flow configurations: (1) the waves generated by a submerged foil and (2) the dynamics of microcapsules in pulsating shear flows. The model is based on the Boundary Element Method (BEM). The fluid equations are formulated in a boundary integral form and, therefore, the model is completely defined by the boundary surfaces that enclose the fluid domain. Unlike numerical domain methods, as Finite Element Method, only the boundary surfaces need to be discretized and this reduces significantly the complexity of the model and the computational requirements. The Non Uniform Rational B-splines (NURBS) and the T-spline frameworks are used to represent both, the geometry and the physical variables. This technique is known as Isogeometrical Analysis (IGA) and it offers several advantages. The most attractive is that it allows a direct integration between modern Computer Aid Design geometric systems and numerical engineering analysis tools. This technique removes intermediate steps, as the generation of the mesh, and it allows the analysis of the exact geometry. In addition, the high order and smoothness of the basis functions make the NURBS and the T-spline to be suitable to deal with complex non-linear dynamic problems. This Thesis is divided into two blocks in which different applications of the IGA-BEM are analyzed.

The first block deals with the simulation of the propagation of non-linear gravity waves and of the wave-structure interactions. Wave propagation is a topic of great interest in the coastal and marine engineering. The analysis of this phenomenon is useful to predict the generation and propagation of tsunamis and it is indispensable for the design of breakwaters and floating structures. The flow is assumed to be inviscid and irrotational and the resulting Laplace's equation is solved using BEM. A mixed

Eulerian-Lagrangian technique in combination with a 4th-order explicit integration scheme is used to update the free surface and the hydrodynamic force is efficiently computed using an auxiliary boundary equation. Some benchmark examples are considered to show the accuracy and stability of the method. In addition, simulations of the waves generated by submerged foils are reported and analyzed. This system has important implications in some wave generator mechanisms installed in surf parks.

In the second block of this Thesis the IGA is applied to analyze the behavior of deformable microcapsules in shear flows. The dynamics of deformable capsules, which are constituted by a liquid enclosed by a deformable membrane, have important implications in a wide range of biological and industrial applications. For instance, capsules are being used for sophisticated therapeutic treatments and many cells, as red blood cells, can be modelled as capsules. In microcirculation problems the Reynolds number is very low and the flow can be modelled with the Stokes equation. For the simulations, the IGA-BEM is used to solve the flow equation and an IGA-FEM is developed for the analysis of the capsule mechanics. Both formulations are coupled in the time domain using a 2nd-order implicit integration scheme. Some benchmark examples are solved to demonstrate the accuracy and stability of the approach, even for large deformations of the capsule. This is achieved thanks to the suitable properties of the basis functions and to the ability to dynamically adapt the mesh according to the needs of the problem. Finally, the dynamics of a capsule in a tube under a pulsatile flow is analyzed with focus on the determination of the influence of capillarity number and frequency of the pulse in the deformation of the capsule.

Resumen

En esta tesis se desarrolla un modelo numérico eficiente y robusto para el análisis de problemas fluido-dinámicos, que posteriormente se valida y se aplica a dos nuevas configuraciones: (1) la generación de ondas de gravedad mediante una hidroala sumergida y (2) la dinámica de una microcápsula en un flujo cortante pulsátil. El modelo se basa en el Método de los Elementos de Contorno (MEC). La ecuación que gobierna el fluido se formula en una forma de integral de contorno, por tanto el modelo numérico queda completamente definido por las superficies de contorno que encierran el volumen fluídico. A diferencia de los métodos basados en el dominio, como por ejemplo el Método de los Elementos Finitos (MEF), solamente las superficies de contorno necesitan ser discretizadas, lo que reduce significativamente la complejidad del modelo y el coste computacional. La tecnología basada en NURBS and T-spline se use para discretizar tanto la geometría como las variables físicas del problema. Esta técnica es conocida como Análisis Isogeométrico (AIG) y tiene ciertas ventajas. La más atractiva es que permite una directa integración entre modernos programas de diseño grafico (CAD) y herramientas de análisis numérico. Esta técnica elimina así laboriosos pasos intermedios, como la generación de la malla, y permite realizar un análisis sobre la geometría exacta del modelo. Además, el alto orden y suavidad de las funciones bases hacen que la tecnología basada en NURBS and T-spline sea idónea para tratar con problemas dinámicos complejos. Esta tesis se divide en dos bloques en los cuales se describen diferentes aplicaciones del método AIG-MEC.

El primer bloque trata sobre la simulación de propagación de ondas de gravedad (olas) e interacción olas-estructuras. La propagación de ondas de gravedad es un tema de gran interés en el campo de la ingeniería de costas e industria marítima. El análisis de este fenómeno es útil para predecir la generación y propagación de tsunamis así como también es indispensable para el diseño de rompeolas o sistemas flotantes. Se

asume que el fluido es inviscido e irrotacional, resultando una ecuación de Laplace que se resuelve mediante el MEC. Se usa una fomulación mixta Euleriana-Lagrangiana en combinación con un esquema de integración explicito de 4º orden para actualizar la superficie libre, mientras que las fuerzas hidrodinámicas se calculan eficientemente mediante una ecuación auxiliar de contorno. Se resuelven varios ejemplos en los que se demuestra la precisión y estabilidad temporal del modelo numérico. Adicionalmente se simula el frente de olas generados por una hidrala sumergida. Este sistema tiene importantes implicaciones en el diseño del mecanismo generador de olas en parques de surf.

En el segundo bloque el AIG se aplica al estudio del comportamiento de microcápsulas deformables suspendidas en flujos cortantes. La dinámica de microcápsules deformables, las cuales están constituidas por un liquido encerrado por una deformable membrana, conlleva importantes implicaciones en un amplio rango de aplicaciones biológicas e industriales. Por ejemplo, las cápsulas están siendo usadas en avanzadas tratamientos farmacológicos y muchas células, como los glóbulos rojos, pueden ser modelados como cápsulas. En el campo de la micro-fluídica el número de Reynold suele ser muy bajo y el flujo puede ser simplificado a la ecuación de Stokes. Para las simulaciones, el AIG-MEC se usa para resolver la ecuación del fluido mientras que se desarrolla una formulación basada en el AIG-MEF para el análisis de la mecánica de la membrana. Ambas formulaciones se acoplan en el dominio del tiempo usando un esquema de integración implícito de 2º orden. Se resuelven varios ejemplos en los que se demuestran la estabilidad y precisión del método, incluso para largas deformaciones de la cápsula. Esto se debe en parte a las inherentes propiedades del las funciones de forma, y en otra parte a la capacidad adaptativa de la malla de acuerdo con las necesidades del problema. Finalmente, se estudia la dinámica de una capsule encerrada en un tubo e implusada por un flujo pulsátil, con el interés de determinar la influencia de la capilaridad y frecuencia del pulso en el comportamiento de la cápsula.

List of Publications and Conferences

Publications in Journal Papers

- Jorge Maestre, Ildefonso Cuesta and Jordi Pallares. An unsteady 3D Isogeometrical Boundary Element Analysis applied to nonlinear gravity waves. Computer Methods in Applied Mechanics and Engineering, (2016), **310**, 112 - 133.
- Jorge Maestre, Jordi Pallares, Ildefonso Cuesta and Michael A. Scott. A 3D Isogeometrical BE-FE Analysis with dynamic remeshing for the simulation of deformable particles in shear flows. Computer Methods in Applied Mechanics and Engineering. (Submitted)
- Jorge Maestre, Jordi Pallares, Ildefonso Cuesta and Michael A. Scott. Dynamics of a capsule in a tube with pulsatile flow. (In process)

Contribution to Conferences

- Jorge Maestre, Jordi Pallares, Ildefonso Cuesta. A 3D Isogeometrical Boundary Element Analysis for nonlinear gravity wave propagation. VII European Congress on Computational Methods in Applied Sciences and Engineering (ECCOMAS Congress 2016). Crete, Greece. (Paper presentation)

UNIVERSITAT ROVIRA I VIRGILI
TOWARDS THE APPLICATION OF THE ISOGEOMETRIC BOUNDARY ELEMENT ANALYSIS TO FLUID MECHANICS:
NON-LINEAR GRAVITY WAVES AND DYNAMICS OF DEFORMABLE CAPSULES IN SHEAR FLOWS
Jorge Maestre Heredia

Internship

Institution: Brigham Young University, Utah (EEUU)
Advisor: Dr. Michael A. Scott
Dates: 2nd February 2015 - 2nd August 2015
Objective:
Development and implementation of an efficient code based on the Isogeometric Boundary Element Analysis for the simulation of biological flows with red blood cells and vesicles.

UNIVERSITAT ROVIRA I VIRGILI
TOWARDS THE APPLICATION OF THE ISOGEOMETRIC BOUNDARY ELEMENT ANALYSIS TO FLUID MECHANICS:
NON-LINEAR GRAVITY WAVES AND DYNAMICS OF DEFORMABLE CAPSULES IN SHEAR FLOWS
Jorge Maestre Heredia

Agradecimientos

Esta tesis doctoral ha sido llevada a cabo dentro del grupo de investigación *Experiments, Computation and Modelization in Fluid Mechanics and Turbulence* (ECoMMFiT), adscrito al Departamento de Ingeniería Mecánica de la Universitat Rovira i Virgili y bajo la dirección de los Drs. Jordi Pallarès e Ildefonso Cuesta.

Quisiera dar mis más sinceros agradecimientos a:

Jordi Pallarès e Ildefonso Cuesta, por su inestimable ayuda, dedicación y paciencia. Sin ellos esta tesis difícilmente hubiera sido posible terminarla. Gracias por todo lo que habéis hecho por mi.

A Michael A. Scott, por haberme dado la oportunidad de realizar una estancia en su grupo de investigación y por toda su ayuda y atención.

Matthias Taus, por su predisposición y sus consejos siempre que lo he necesitado.

A todos mis compañeros del laboratorio, con los que he compartido muchos momentos, a veces reflexionando sobre temas científicos, otras simplemente disfrutando de la amistad.

A mi familia y a María, por su apoyo y sobre todo, por su infinita paciencia.

Y a todos aquellos que habéis participado directa o indirectamente en el desarrollo de este trabajo.

Finalmente agradecer a la Universitat Rovira i Virgili por el soporte financiero.

UNIVERSITAT ROVIRA I VIRGILI
TOWARDS THE APPLICATION OF THE ISOGEOMETRIC BOUNDARY ELEMENT ANALYSIS TO FLUID MECHANICS:
NON-LINEAR GRAVITY WAVES AND DYNAMICS OF DEFORMABLE CAPSULES IN SHEAR FLOWS
Jorge Maestre Heredia

List of Figures

List of Tables

UNIVERSITAT ROVIRA I VIRGILI
TOWARDS THE APPLICATION OF THE ISOGEOMETRIC BOUNDARY ELEMENT ANALYSIS TO FLUID MECHANICS:
NON-LINEAR GRAVITY WAVES AND DYNAMICS OF DEFORMABLE CAPSULES IN SHEAR FLOWS
Jorge Maestre Heredia

Conventions

The main notational conventions used through this dissertation are:

$\cdot_{i,j,k}$	Tensor index
$\cdot_{\alpha,\beta}$	Tensor index ($\alpha, \beta = 1, 2$)
Γ	Physical space
$\widehat{\Gamma}$	Parametric space
$\widetilde{\Gamma}$	Parent domain
Ω	Fluid domain
$\boldsymbol{\Xi}$	Knot vector
$\Delta\boldsymbol{\Xi}$	Knot interval vector
ξ	Parametric coordinate
$\tilde{\xi}$	Parent coordinate
$\mathbf{P}$	T-spline or NURBS control point
$\mathbf{Q}$	Bézier control point for quadrilateral elements
$\mathbf{T}$	Bézier control point for triangular elements
w	Control weight
N	B-spline basis functions
R	Rational basis function (NURBS or T-spline)
B	Bernstein basis function
$\mathbf{C}$	Bézier extraction operator
$\mathbf{C}^{TQ}$	Transformation matrix from triangular to quadrilateral Bézier elements and vice versa
$\mathbf{C}^{QQ}$	Transformation matrix from quadrilateral degenerated Bézier element to quadrilateral non degenerated elements
ϕ	Potential
q	Potential flux

$\mathbf{x}$	Cartesian coordinate vector
$\mathbf{n}$	Normal vector
$\mathbf{v}$	Velocity vector
$\mathbf{a}$	Acceleration vector
$\mathbf{u}$	Displacement vector
$\mathbf{e}$	Euler-Almansi strain tensor
$\boldsymbol{\sigma}$	Fluid stress tensor
$\boldsymbol{\tau}$	In-plane Cauchy stress tensor
$\mathbf{f}$	Force vector
$\mathbf{m}$	Momentum vector
$\mathbf{t}$	Traction vector
p	Pressure
ΔP	Pressure drop
t	Time
$\mathbb{v}$	Volume
$\boldsymbol{\lambda}$	Cartesian bases
$\mathbf{g}_i$	Local covariant bases
$\mathbf{g}^i$	Local contravariant bases
$\mathbf{F}$	Deformation gradient tensor
Q	Flow rate
$\mathcal{G}$	Single-layer kernel
$\mathcal{H}$	Double-layer kernel
$\mathfrak{C}$	Solid angle
$\mathfrak{G}$ and $\mathfrak{T}$	Fundamental solution
Ca	Capillarity number
ς	Damping factor
ω	Angular velocity
μ	Fluid dynamic viscosity
ρ	Fluid density
κ	Viscosity ratio
g	Gravity
$\dot{\gamma}$	Shear rate
D_{12}	Taylor parameter (measurement of the deformation)
R_T	Equivalent radius of the tube
R_C	Equivalent radius of the capsule

δ	Ratio between radius of the capsule and the radius of the tube
G_s	Shear elastic modulus
C	Constant parameter that measures the ratio of area dilation modulus to shear modulus
Ψ	Deformation energy function
J_s	Surface dilatation
I_i	Strain invariants

The most common acronyms and abbreviations are listed as follows:

IGA	Isogeometric Analysis
NURBS	Non-Uniform Rational B-splines
FE	Finite Element
CAD	Computer Aid Design
BEM	Boundary Element Method
FEM	Finite Element Method
FDM	Finite Difference Method
LBM	Lattice Boltzmann Method
VFM	Volume Finite Method
CFD	Computational Fluid Dynamics
IBM	Immersed Boundary Method
DoF	Degrees of Freedom
2D	Bi-dimensional
3D	Three-dimensional
RBC	Red Blood Cell
MEL	Mixed Eulerian-Langrangian
BIE	Boundary Integral Equation
CPV	Cauchy Principal Value
PVW	Principle of Virtual Works
GMRES	Generalized Minimal Residual

UNIVERSITAT ROVIRA I VIRGILI
TOWARDS THE APPLICATION OF THE ISOGEOMETRIC BOUNDARY ELEMENT ANALYSIS TO FLUID MECHANICS:
NON-LINEAR GRAVITY WAVES AND DYNAMICS OF DEFORMABLE CAPSULES IN SHEAR FLOWS
Jorge Maestre Heredia

Chapter 1

Introduction

1.1 Isogeometric analysis applied to the fluid dynamics

In the last decades the use of the Isogeometric Analysis (IGA) has experienced a fast grown in the engineering analysis field. The concept of IGA was originally introduced by Hughes et al. [7, 8] and Cottrell et al. [9, 10] in the Finite Element Method (FEM) context. Initially based on the Non-Uniform Rational B-spline (NURBS), the idea consists in using the same class of functions for the discretization of the geometry and the physical variables of the numerical model. This establishes a tight link between the Computer Aided Design (CAD) geometry and the engineering analysis tools. This technique presents multiple advantages. The most promising one is related to the fact that the geometry is directly embedded in the numerical analysis. This is, the geometry is preserved and no additional steps are needed to translate the CAD geometry to the numerical analysis. Other advantages emanate from the NURBS, such as: (1) quadratic and cubic surfaces can be represented exactly; (2) advanced construction techniques and shape modification tools are available; (3) the high continuity and smoothness of the basis can be managed via knot vector (4) h, p and k-refinement can be applied without modifying the geometry. These characteristics, in combination with other mathematical properties, give to NURBS the ability to handle complex geometries and provide suitable basis for numerical analysis.

While the research community has paid much attention to the IGA based on the FEM, few works based on the IGA-Boundary Element Method (BEM) has been

reported in the literature. The BEM is an elegant alternative to solve partial differential equations (PDE). The key of the BEM is that only the boundary surfaces enclosing the domain of the problem have to be discretized. This feature has important implications in the engineering analysis as: (1) the dimensionality of the model is reduced and the computational requirement is considerably lower than the FEM; (2) the complexity of the geometric model is simplified to the boundary surfaces which are precisely the data imported from the CAD systems; (3) refinements and modifications of the mesh can be applied without excessive computational cost; (4) 3D dynamic meshes can be easily managed; and (5) the Sommerfeld condition is implicitly satisfied in the formulation that simplifies the applications of the boundary conditions in external problems with infinite phsysical domain. In Fig. 1.1 it is shown a typical mesh for a generic solid using the BEM. These features make the IGA-BEM analysis to be especially attractive in the engineering analysis. The extension of the NURBS-based IGA to the BEM was introduced by Politis et al.[11] and Simpson et al. [12], who applied the technique to the 2D potential flow and elastostatic field, respectively. Recent advances of the IGA-BEM analysis have appeared in the literature applied to acoustics [13, 14], Laplace's equation [15, 16], elastostatic [12], wave resistance [17, 18] and fluid-structure interaction [19]. These studies have demonstrated the higher accuracy of the IGA-BEM in comparison with the traditional formulation of the BEM based on the Lagrange polynomials. This advantage is based on the superior geometric approximation and high order of continuity of the basis functions .

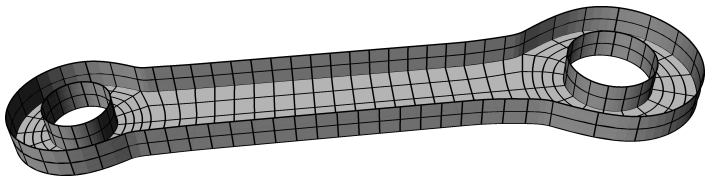

Figure 1.1: Mesh of a solid connecting rod for the BEM. The view represents a horizontal cut of the solid. Note that only the boundary surfaces have to be discretized.

Although the NURBS is widely used by the CAD industry, it has some limitations associated with the fact that only surfaces with four edges can be represented. This causes that the representation of complicated geometries may require many NURBS patches and the smoothness between patches can be lost. The T-spline technology has been introduced to overcome these limitations [20]. T-splines are a generalization of the NURBS, in which several NURBS patches can be integrated into a unique T-spline. Moreover, unlike the NURBS, T-splines allow local refinements and unstructured

meshes. In Fig. 1.2 a example of mesh on an air-foil is shown. The mesh is unstructured and a local refinement has been applied to the trailing edge where the curvature is very high and complex phenomenons are expected to happen.

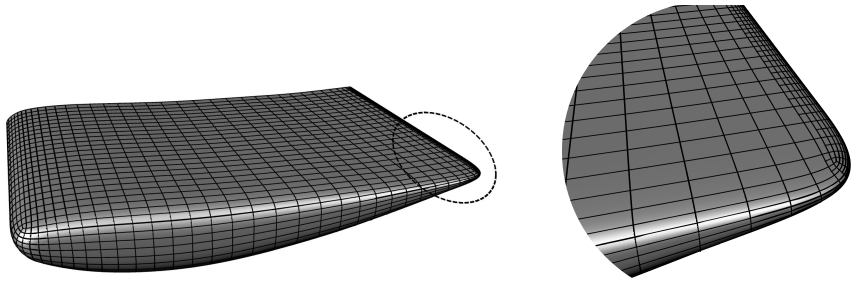

(a) (b)

Figure 1.2: (a) Asymmetric foil modeled with a T-spline surface. (b) Detail of refinement on the trailing edge

The implementation of T-spline in the IGA requires a more advanced development. Scott et al. [21] and Li et al. [22] formulated the analysis-suitable T-spline in which the necessary mathematical properties of the basis (as the linear independence) are guaranteed. Adopting the idea of the Bézier extraction operation, presented by Borden et al. [23] and Scott et al. [24], the T-spline and NURBS can be incorporated efficiently via modifying the shape functions in the classical BEM and FEM. Thomas et al. [25] developed a generalization of this technique. In recent years, the application of the T-spline in the IGA framework to different areas has been developed [26–30]. In the context of IGA-BEM analysis, Scott et al. [24] extended the analysis-suitable T-spline to unstructured meshes for elastostatic problems and developed a collocation procedure based on a generalization of the Grenville abscissae. Simpson et al.[31] applied this method to acoustic problems and demonstrated the higher accuracy in comparison with the conventional Lagrange discretization. Ginnis et al. [32] used an IGA-BEM analysis, based on the T-spline, to analyse the ship wave resistance problem and Kostas et al. [33] used this method to optimize the hull shape.

Other alternatives to the analysis-suitable T-spline are appearing in the literature. These alternatives include hierarchical spline (B-splines, NURBS and T-spline), PHT-splines and LR-splines. In addition to the limited works cited above, the interested reader can be found an overview of the IGA in [34].

The link between the T-spline and the BEM form has several advantages for the numerical analysis. Very complex geometric models can be constructed using

T-splines. The geometry can be directly imported from CAD systems and few degrees of freedom (DoF) are needed due to the high geometric approximation of the T-spline basis. On the other hand, the BEM has been demonstrated to be a very accurate numerical method when it is suitable formulated and implemented. Nevertheless, the formulation of the BEM has to be well understood. The accuracy of the method is very sensitive to small numerical errors in the implementation of the code. It should be noted that the method involves the computation of singular integrals. A suitable treatment should be applied in order to obtain accurate results. An other important aspect is related to the corners produced by the intersection of several surface because in this locations the normal is not uniquely defined and it can lead to numerical problems. A detailed study of the BEM in the context of IGA is addressed in this document.

An additional advantage is found when the IGA-BEM approach is used in dynamic problems with large distortions and displacements of the mesh. In this case, the mesh is more simple in comparison with the domain methods (as the FEM, Volume Finite Method (VFM), Finite Difference Method (FDM), etc.) and the geometric model is more easily managed, especially in 3D problems. Several studies of dynamic problems using the conventional BEM based on Lagrange elements [35–38] have revealed instabilities associated to the lack of continuity between elements and saw-tooth effects have been observed between elements (see Fig. 1.3). The control of the error during the simulation is an important issue because it is stored along the time and it can lead to instabilities or inaccurate results. Artificial techniques have been proposed to alleviate these instabilities but they involve the modification of the geometry and they are made ad-hoc. Although based on the FEM, Lipton et al. [39] demonstrated the robustness and accuracy of the IGA approach under severe distortions of the mesh thanks to the high continuity of the Splines basis functions. Recently, Abbasniaa and Ghiasia [40] developed a 2D NURBS-based BEM approach in the time domain for the analysis of non linear wave-structure interaction and they showed stability of the approach for long time simulations. These studies demonstrate the potential of the IGA to be applied to dynamic problems with large distortions of the mesh.

The literature review shows that the IGA–BEM based on the NURBS and T-spline is a very recent topic. This Thesis is focused on the study of selected fluid mechanics problems using the IGA-BEM based on the NURBS and T-spline framework in the time domain. The method is developed for two different applications where the fluid equation can be expressed in a boundary integral form. The first application consists

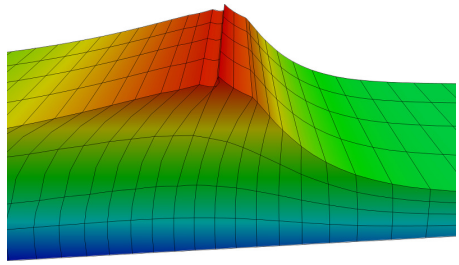

Figure 1.3: Typical instability of dynamic problems with large distortion of the mesh when C^0 picewise continuous elements are used.

in the study of the propagation of gravity waves and wave-structure interactions. Nowadays, this field is very active due to the increasing interest on the ocean renovable energy in which the generation systems are installed near-shore or off-shore. A suitable design of the floating and anchorage systems has to consider the wave-structure interaction. Different numerical models have been presented, most of them are based on the potential flow theory (see for example [41–48]). In this line, the fluid is assumed to be incompressible, inviscid and irrotational. In spite of these simplifications, experiments have demonstrated agreement with the numerical predictions [49–51]. The simplicity and low computational cost make this model to be ideal in the first phases of the design process. Moreover, invoking the IGA paradigm complex 3D geometric models can be simulated with reduced effort due to the integration with CAD systems. Fig. 1.4 shows the typical waves radiated from a moving submerged sphere. The figure represents a vertical section of the model. Note that only the boundary surfaces are discretized.

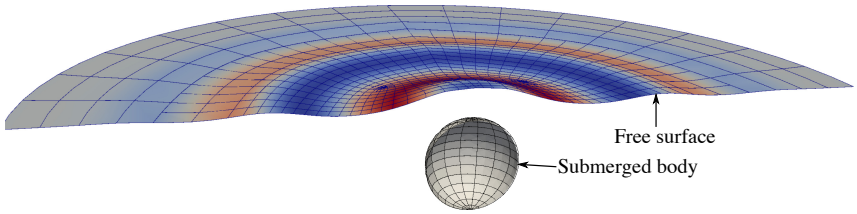

Figure 1.4: Waves generated by a submerged sphere with a sinusoidal vertical movement

As a second application, the hydrodynamic movement of a deformable micro-capsule in shear flows is analysed. A microcapsule consist in a very thin deformable membrane enclosing an internal liquid (see Fig. 1.5). Capsules are present in nature and in the industrial applications. Red blood cells (or erythrocytes) (RBC)

are a example of a biological capsule. The membrane is a complex structure that usually is simplified as a thin elastic shell. This membrane separates and protects the internal hemoglobin from the external plasma. The main function of the RBC is the transportation of the respiratory gases (oxygen and carbon dioxide) to the cells through the circulatory system. In this way, RBCs can passes through micro-capillaries of small diameters involving large deformation. This deformability is essential for the correct function of RBCs. Some types of bacteria and other micro-organisms can be also modelled as biological capsules. In the industry, the micro-encapsulation is a very common technique. Artificial capsules are made to isolate and protect the internal active substance from the external ambient. As pharmacologic treatments, these capsules are used for the transportation of therapeutic substances and the sustained release to targeted areas. The capsule membrane protects from the attack of the immune system and it reduces possible secondary effects. This technique has been extended to other industrial areas as the cosmetics or food industry. Therefore, the understanding of the dynamic of deformable capsules is fundamental for the development of these applications.

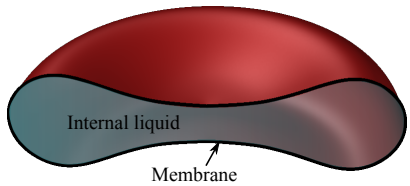

Figure 1.5: Schematic illustration of the section of a capsule

1.2 Objectives

The main objective of this thesis is the development and implementation of an efficient and robust IGA-BEM model, based on the analysis suitable T-spline and NURBS framework and formulated in the context of the Bézier extraction operation, to analyse two fluid mechanics problems:

- The propagation of gravity waves and wave-structure interaction.
- The Dynamics of deformable capsules in shear flows

A detailed study is carried out in this document and various aspects are treated to check the ability and accuracy of T-spline and NURBS-based IGA-BEM approach:

- Study of the spatial converge for different mesh configuration (structured and unstructured mesh) and order of the basis.
- Analysis of the temporal stability and accuracy under large movements and distortions of the mesh.
- Comparison with the standard formulation based on the Lagrange elements
- Application to several examples of engineering and biomedical interest.

Fig. 1.6 synthesize the basic ideas of the T-spline-based IGA-BEM. The example consists on the flowing of a initial capsules through a cylindrical micro-channel. For clarity purposes, a vertical section of the pipe is shown. Note that only the boundary surfaces are discretized, this is, the pipe and the membrane. This reduces considerably the complexity and size of the mesh. An unstructured mesh is used to represent the membrane whereas the pipe is built with a structured mesh. The geometry of the pipe is exact thanks to the ability of the T-spline to represent quadratic surfaces and a refinement is applied in the central region where the capsule is placed. The geometry is generated using the commercial CAD software Rhinoceros [52] and it is imported directly to the numerical analysis code. Fig 1.6b shows the deformation of the capsule at a specific instant when the capsule acquires the typical asymmetrical parachute shape. Despite the large deformation of the capsule, no signs of instability are observed and the membrane surface remains smooth during the simulation. This example demonstrates the potential of the T-spline-based IGA-BEM approach to simulate dynamic problems with large deformations of the mesh as well as its versatility due to the integration with modern CAD software.

1.3 Structure of the document

The organization of this thesis is as follows:

- *Chapter 1*: It contains an introduction and the main objectives of this thesis.
- *Chapter 2*: It includes a brief overview of the NURBS and T-spline formulation.
- *Chapter 3*: It describes the formulation of the IGA-BEM based on the T-spline and NURBS framework applied to the analysis of wave propagation and wave-structure interaction. Simulations of the waves generated by the movement of submerged foils is reported which have implications in some wave generator systems installed in surf parks. The chapter contains a more specific introduction and conclusion relative to this field.

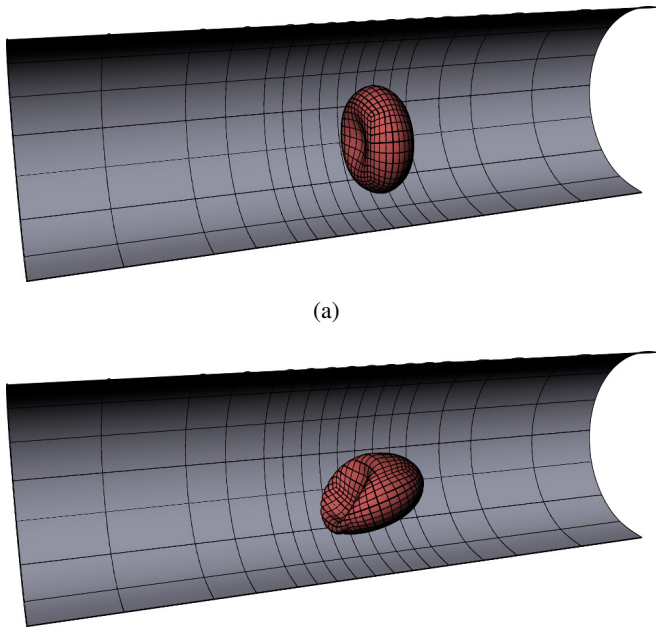

(a)

(b)

Figure 1.6: Movement of a deformable capsule in a cylindrical tube due to a pressure-driven flow: (a) Initial state and (b) deformation at the dimensionless time $t = 7.15$ when the capsule acquires the typical asymmetrical parachute shape.

- *Chapter 4*: The T-spline-based IGA-BEM approach is applied to microfluics. A IGA-FEM formulation is developed for the analysis of the membrane mechanics and it is coupled with the IGA-BEM fluid model. The approach is applied to simulate the behaviour of a deformable capsule in a confining pulsating shear flow. A specific short introduction and conclusions are included.
- *Chapter 5*: The main conclusions are drawn and potential directions for the future research are outlined.

Chapter 2

Geometric fundamentals

In this chapter we present briefly the basic concepts of the NURBS and T-spline in the context of IGA. For more details, the reader is refereed to [20, 53–56]

Considering that the formulation shown in this thesis is developed for 3D geometric models, we focus on 3D surfaces. In this case, the physical space is defined by $\Gamma \in \Re^{d_s}$ with $d_s = 3$ and the parameter space is reduced to $\widehat{\Gamma} \in \Re^{d_p}$ with $d_p = 2$.

2.1 NURBS and T-Spline surfaces

A NURBS surface is described in terms of a control mesh and a valid pair of knot vectors. A valid knot vector is a non-decreasing sequence of real numbers that parametrizes the surface in each topological direction. A knot vector is denoted by $\boldsymbol{\Xi}^i = \{\xi_1^i, \xi_2^i, ..., \xi_{1+m_i+p_i}^i\}$, where $\xi_k^i \in \Re$ is the kth knot value, and m_i is the number of B-spline basis functions of degree p_i in the i direction. Hereinafter, we denote the multi-index $\mathbf{p} = \{p_1, p_2\}$, $\mathbf{m} = \{m_1, m_2\}$ and the parametric coordinate $\boldsymbol{\xi} = \{\xi^1, \xi^2\}$. The control mesh is a set of vertices that forms a structured set of quadrilateral elements. Each vertex has associated a control point $\mathbf{P}_A \in \Re^{d_s}$ and a weight $w_A \in \Re$, where $A = 1, 2, ..., m_{cp}$ is the global index that denotes all vertices $m_{cp} = \prod_{i=1}^{d_p} m_i$ (see Fig. 2.1a).

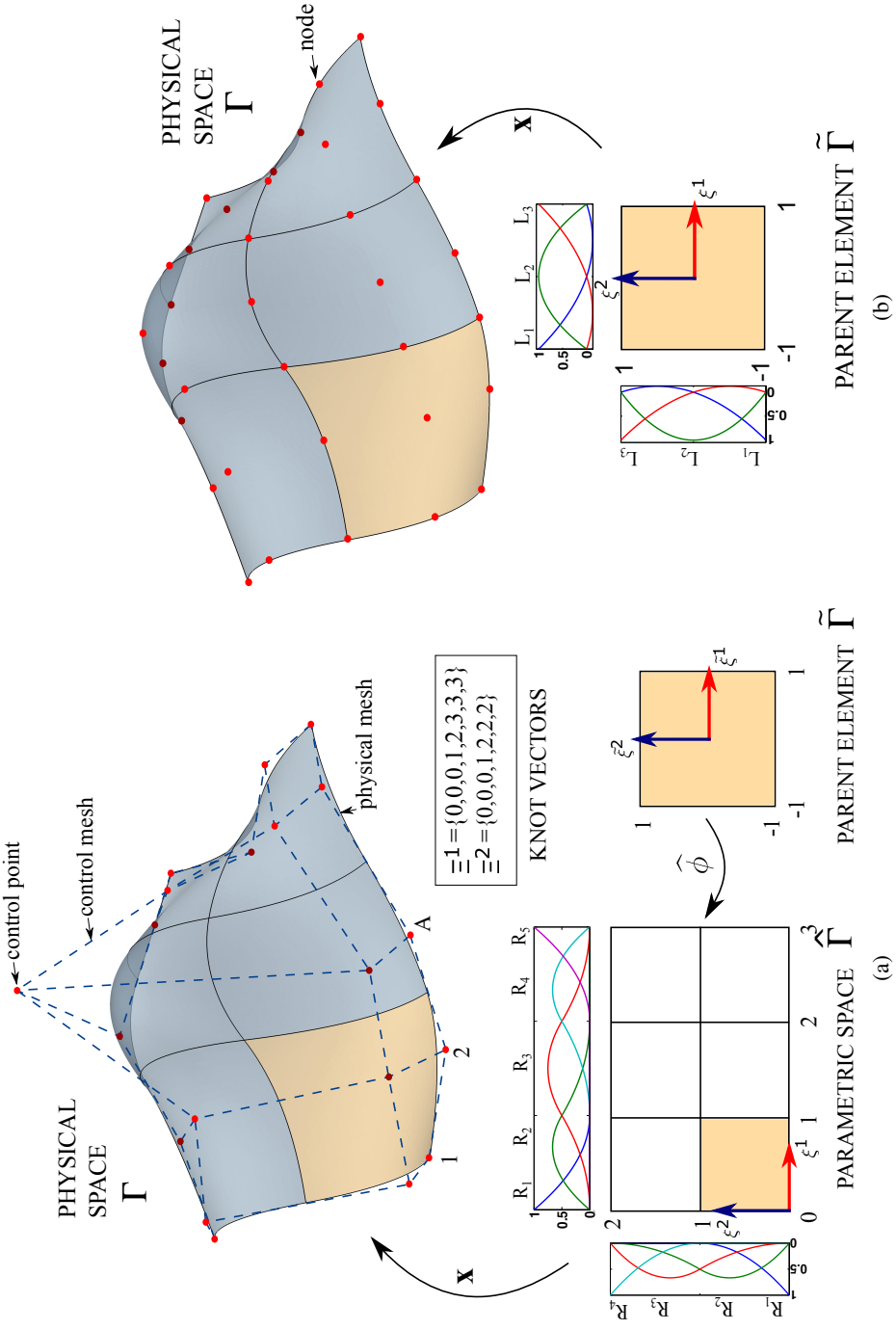

Figure 2.1: Schematic illustration of a (a) 3D quadratic NURBS, and (b) a quadratic Lagrange surface.

If we define the parametric space by $\widehat{\Gamma} = [\xi_1^1, \xi_{1+m_1+p_1}^1] \times [\xi_1^2, \xi_{1+m_2+p_2}^2]$ (as shown in Fig. 2.1a), the NURBS surface that maps the parametric space to the physical space $\mathbf{x} : \widehat{\Gamma} \rightarrow \Gamma$ can be expressed as:

$$\mathbf{x}(\boldsymbol{\xi}) = \frac{\sum_{A=1}^{m_{cp}} \mathbf{P}_A w_A N_{A,\mathbf{p}}(\boldsymbol{\xi})}{\sum_{A=1}^{m_{cp}} w_A N_{A,\mathbf{p}}(\boldsymbol{\xi})} = \sum_{A=1}^{m_{cp}} \mathbf{P}_A R_A(\boldsymbol{\xi}) \qquad \boldsymbol{\xi} \in \widehat{\Gamma} \tag{2.1}$$

where $N_{A,\mathbf{p}}(\boldsymbol{\xi})$ is the bivariate B-spline basis functions of $\mathbf{p}$ degree associated with the global vertex A and $R_{A,\mathbf{p}}(\boldsymbol{\xi})$ denotes the rational basis functions construct with the weights and the B-spline basis functions. The bivariate B-spline basis functions are built by forming a tensor product of univariate basis functions ($N_{A,p_i}^i(\xi^i)$) as:

$$N_{A,\mathbf{p}}(\boldsymbol{\xi}) = \prod_{i=1}^{d_p} N_{A,p_i}^i(\xi^i) \tag{2.2}$$

The univariate B-spline basis function is inferred uniquely from the corresponding knot vector. Using the following recurrence relation, the kth univariate B-spline basis is defined as:

$$\begin{aligned} N_{k,0}^i(\xi^i) &= \begin{cases} 1 & \text{if } \xi_k^i \leq \xi^i < \xi_{k+1}^i \\ 0 & \text{otherwise} \end{cases} \\ N_{k,p_i}^i(\xi^i) &= \frac{\xi^i - \xi_k^i}{\xi_{k+p_i}^i - \xi_k^i} N_{k,p_i-1}^i(\xi^i) + \frac{\xi_{k+p_i+1}^i - \xi^i}{\xi_{k+p_i+1}^i - \xi_{k+1}^i} N_{k,p_i-1}^i(\xi^i) \end{aligned} \tag{2.3}$$

Hereinafter we drop the sub-index $\mathbf{p}$ from the basis functions.

Note that the NURBS is limited to surfaces defined by four edges. To represent more complex geometries it is necessary to divide the models in different rectangular patches. In the context of the BEM, a C^0 continuity is required across the patch. This is not guaranteed in all the cases and in this work we satisfy this condition by choosing the same knot vector, weight and control points along the shared edge between adjacent patches. In this case, if a refinement is performed in a patch, it affects globally to the rest of the patches.

This limitation can be overcome naturally using the T-spline framework which allows the existence of hanging and extraordinary points within the control mesh. For a cubic T-spline, the mapping is expressed in a similar way as in Eq. 2.1. However,

unlike NURBS, the surface is locally parametrized by defining of a local pair of knot interval vectors $\Delta\Xi^i_A = \{\Delta\xi^i_{A,1}, \Delta\xi^i_{A,2}, ..., \Delta\xi^i_{A,1+p_i}\}$ with $\Delta\xi_i = \xi_{i+1} - \xi_i$, associated to each vertex A where the T-spline basis functions is restricted to be non-null. This provides the capacity of making unstructured meshes and local refinements. An example is shown in Fig. 2.2. A simple geometry is represent using a T-spline and a NURBS surface. Despite the simplicity, three NURBS patches are required whereas the T-spline surface is reduced to an unique patch. Moreover a refinement is made to both geometric model. While a local refinement can be applied to the T-spline surface, the NURBS refinement is globally extended throughout the entire domain and patches.

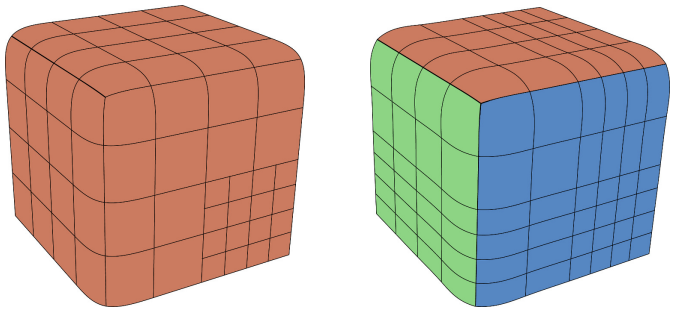

(a) Local refinement (b) Global refinement

Figure 2.2: Representation of the half of a smooth cube using (a) a T-spline and (b) a NURBS surface. A refinenent is applied at the right corner.

Some important properties of the T-spline and NURBS basis functions are:

- Partition unity: $\sum_{A=1}^{m_{cp}} R_A(\boldsymbol{\xi}) = 1$ for all $\boldsymbol{\xi}$.
- Pointwise nonegativity: $R_A(\boldsymbol{\xi}) \geq 0$ for all A and $\boldsymbol{\xi}$.
- Compact support: $R_A(\boldsymbol{\xi}) > 0$ for all $\boldsymbol{\xi} \in [0, \sum_{i=1}^{p_1+1} \Delta\xi^1_{A,i}] \times [0, \sum_{i=1}^{p_2+1} \Delta\xi^2_{A,i}]$ and A.
- Linear independence: $\sum_{A=1}^{m_{cp}} c_A R_A(\boldsymbol{\xi}) = 0$ if $c_A = 0$ for all A and $\boldsymbol{\xi}$.
- Control of continuity: the basis are $C^{(p-k)}$ continuous with k being the multiplicity of a knot.

2.2 A finite element structure

The idea is to discretize the physical domain with a series of independent elements $\mathbf{x}^e(\tilde{\boldsymbol{\xi}})$ (T-spline element) defined over a parent domain $\tilde{\boldsymbol{\xi}} \in \widetilde{\Gamma}$ [23]. Considering the compact support property of the basis functions, there exists a number of them, m_e, which are non-null over each element e. Then, we can construct a matrix $A = IEN(e, a)$, that maps the local basis functions number a in the element e to the global function A.

The local geometry, restricted to each element domain, is defined as:

$$\mathbf{x}^e(\tilde{\boldsymbol{\xi}}) = \frac{\sum_{a=1}^{m_e} \mathbf{P}_a^e w_a^e N_a^e(\tilde{\boldsymbol{\xi}})}{\sum_{a=1}^{m_e} w_a^e N_a^e(\tilde{\boldsymbol{\xi}})} \qquad \tilde{\boldsymbol{\xi}} \in \widetilde{\Gamma} \tag{2.4}$$

and in compact form it can be rewritten as:

$$\mathbf{x}^e(\tilde{\boldsymbol{\xi}}) = \frac{(\mathbf{P}^e)^T \mathbf{W}^e \mathbf{N}^e(\tilde{\boldsymbol{\xi}})}{(\mathbf{w}^e)^T \mathbf{N}^e(\tilde{\boldsymbol{\xi}})} \qquad \tilde{\boldsymbol{\xi}} \in \widetilde{\Gamma} \tag{2.5}$$

where $\mathbf{P}^e = \{\mathbf{P}_a^e\}_{a=1}^{m_e}$ is a set of the control points, $\mathbf{w}^e = \{W_a^e\}_{a=1}^{m_e}$ is a vector of weights, $\mathbf{W}^e = diag(\mathbf{w}^e)$ is a diagonal matrix and $\mathbf{N}^e(\tilde{\boldsymbol{\xi}}) = \{N_a^e(\tilde{\boldsymbol{\xi}})\}_{a=1}^{m_e}$ is a vector of the basis functions relative to the element e.

Fig. 2.1 shows the comparison between a quadratic NURBS and a quadratic Lagrange representation. In the context of NURBS, the image of the parametric space to the physical space defines a physical mesh. This entails that each physical element e can be described over a parent element domain by defining a mapping from the parent domain to the parametric space $\widehat{\Phi}^e : \widetilde{\Gamma} \rightarrow \widehat{\Gamma}$. This description can be considered analogous to the traditional FEA, but with some differences. The control points do not have to lie on the physical space, unlike the nodes defined in the Lagrange model. The geometry is continuous even across elements, and this continuity can be managed using the knot vectors. Moreover, natural global h, p and k refinement can be performed without modifying the geometry.

Fig. 2.3 we show a example of the construction of the IEN array. This figure represents the T-spline elements of a generic plane surface. The highlighted quadrilateral denoted the T-spline element number 1 which is supported by the highlighted control points. The control points are in one-to-one correspondence with the basis functions, therefore they denote the non-zero basis functions over the

element. The Table 2.2 contains the IEN matrix relative to this example. Each row reveals the actives basis function over the corresponding element and maps the local index to the global index.

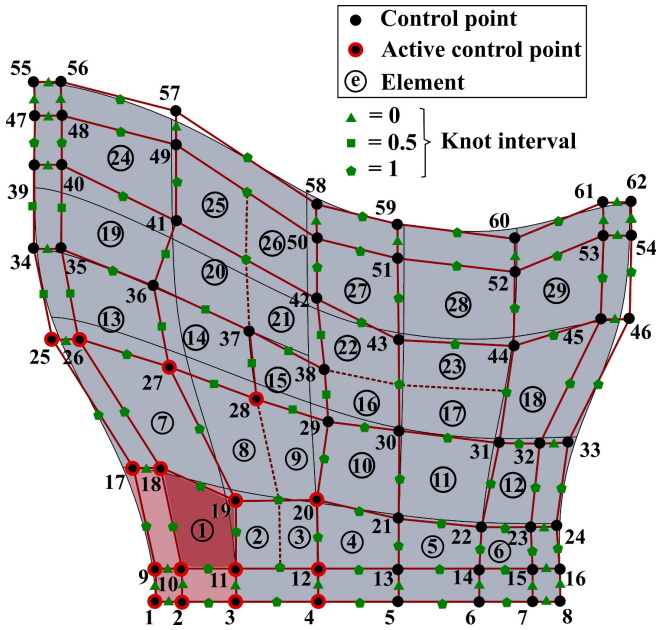

Figure 2.3: T-spline elements in the T-spline control mesh. The sublayer corresponds to the physical space. The dark highlighted quadrilateral denotes the T-mesh element number 1 which is maped over the physical space (soft highlighted quadrilateral). The highlighted circles correspond to the basis functions non-zero over the T-spline element 1. Note that there exist a one-to-one correspondence between control points and basis functions.

It should be noted that the number of T-spline basis functions contained in each element can be different, while in the case of NURBS are exactly equal to $\prod_{i=1}^{d_p}(p_i+1)$. Furthermore, the T-spline and NURBS basis functions affect to different elements and their definition depends on the topology. As proposed by Scott et al. [57], we draw on the Bézier extraction concept as an elegant method to standardize the T-spline and NURBS framework in isogeometric analysis.

The Bézier extraction is a linear operator that maps the NURBS or T-spline basis functions over each element to a same set of Bernstein polynomials. Let us define a set of bivarite Bernstein basis $\mathbf{B}(\tilde{\boldsymbol{\xi}}) = \{B_{a,\mathbf{p}}(\tilde{\boldsymbol{\xi}})\}_{a=1}^{m_b}$ with $m_b = \prod_{i=1}^{d_p}(p_i+1)$ (in case of cubic T-spline $m_b = 16$). The NURBS or T-spline basis can be expressed as,

$$\mathbf{N}^e = \mathbf{C}^e\mathbf{B} \tag{2.6}$$

	A=IEN(e,a)																
$e \setminus a$	1	2	3	4	5	6	7	8	9	10	11	12	13	14	15	16	17
1	1	2	3	4	9	10	11	12	17	18	19	20	25	26	27	28	
2	2	3	4	5	10	11	12	13	18	19	20	21	26	27	29	28	
3	2	3	4	5	10	11	12	13	18	19	20	21	27	29	30	28	
4	3	4	5	6	11	12	13	14	19	20	21	22	29	30	31	28	
5	4	5	6	7	12	13	14	15	20	21	22	23	29	30	31	32	
6	5	6	7	8	13	14	15	16	21	22	23	24	30	31	32	33	
7	9	10	11	12	17	18	19	20	25	26	27	34	35	36	28	37	
8	10	11	12	13	18	19	20	21	26	27	29	43	35	36	38	28	37
9	10	11	12	13	18	19	20	21	27	29	30	43	36	38	28	37	
10	11	12	13	14	19	20	21	22	29	30	31	43	44	38	28	37	
11	12	13	14	15	20	21	22	23	29	30	31	32	43	44	45	38	
12	13	14	15	16	21	22	23	24	30	31	32	33	43	44	45	46	
13	17	18	19	20	25	26	27	39	40	41	42	34	35	36	28	37	
14	18	19	20	21	26	27	29	40	41	42	43	51	35	36	38	28	37
15	18	19	20	21	27	29	30	40	41	42	43	51	36	38	28	37	
16	19	20	21	22	29	30	31	41	42	43	44	51	52	38	28	37	
17	20	21	22	23	29	30	31	32	42	43	44	45	51	52	53	38	
18	21	22	23	24	30	31	32	33	43	44	45	46	51	52	53	54	
19	25	26	27	39	40	41	42	47	48	49	50	34	35	36	28	37	
20	21	26	27	29	40	41	42	43	48	49	50	51	35	36	38	28	37
21	21	27	29	30	40	41	42	43	48	49	50	51	36	38	28	37	
22	21	22	29	30	31	41	42	43	44	49	50	51	52	38	28	37	
23	21	22	23	29	30	31	32	42	43	44	45	50	51	52	53	38	
24	39	40	41	42	47	48	49	50	55	56	57	58	34	35	36	37	
25	40	41	42	43	48	49	50	51	56	57	58	59	35	36	38	37	
26	30	40	41	42	43	48	49	50	51	56	57	58	59	36	38	37	
27	30	31	41	42	43	44	49	50	51	52	57	58	59	60	38	37	
28	30	31	32	42	43	44	45	50	51	52	53	58	59	60	61	38	
29	30	31	32	33	43	44	45	46	51	52	53	54	59	60	61	62	

Table 2.1: IEN array constructed for the example 2.3. The IEN array maps the local basis function a relative to the element e to the global basis function A.

in which $\mathbf{C}^e \in \Re^{m_e \times m_b}$ is the matrix extraction operator corresponding to the element e.

Introducing the Eq. 2.6 in the Eq. 2.5 each element can be written in terms of an independent Bézier patch as follows,

$$\mathbf{x}^e(\tilde{\boldsymbol{\xi}}) = \frac{(\mathbf{P}^e)^T \mathbf{W}^e \mathbf{C}^e \mathbf{B}(\tilde{\boldsymbol{\xi}})}{(\mathbf{w}^e)^T \mathbf{C}^e \mathbf{B}(\tilde{\boldsymbol{\xi}})} = \frac{(\mathbf{Q}^e)^T \mathbf{W}^{b,e} \mathbf{B}(\tilde{\boldsymbol{\xi}})}{(\mathbf{w}^{b,e})^T \mathbf{B}(\tilde{\boldsymbol{\xi}})} \qquad \tilde{\boldsymbol{\xi}} \in \widetilde{\Gamma} \tag{2.7}$$

where $\mathbf{Q}^e = \{\mathbf{Q}_b^e\}_{b=1}^{m_b}$ is the vector of Bézier control points and $\mathbf{w}^{b,e} = \{W_b^e\}_{b=1}^{m_b}$ is the vector of Bézier weights, which can be expressed as,

$$\mathbf{Q}^e = (\mathbf{W}^{b,e})^{-1} (\mathbf{C}^e)^T \mathbf{W}^e \mathbf{P}^e \tag{2.8}$$

$$\mathbf{w}^{b,e} = (\mathbf{C}^e)^T \mathbf{w}^e \tag{2.9}$$

Alternatively, Eq. 2.7 can be expressed in reduced form as,

$$\mathbf{x}^e(\tilde{\boldsymbol{\xi}}) = (\mathbf{P}^e)^T\mathbf{R}^e(\tilde{\boldsymbol{\xi}}) = (\mathbf{R}^e)^T(\tilde{\boldsymbol{\xi}})\mathbf{P}^e \qquad \tilde{\boldsymbol{\xi}} \in \widetilde{\Gamma} \tag{2.10}$$

being $\mathbf{R}^e(\tilde{\boldsymbol{\xi}}) = \{R_a^e\}_{a=1}^{m_e}$ a vector of local rational basis function.

Fig. 2.2 shows a schematic illustration of the Bézier extraction operation applied to a NURBS curve. For details about the construction of Bézier operators see [23, 57]. In Appendix A we shown briefly the concepts of the Bézier elements.

2.3 Extraordinary points and degenerate elements

In this thesis we deal with surfaces that require extraordinary points and degenerated elements (see Fig. 2.5). In both cases the continuity of the geometry is locally reduced. An extraordinary point is a vertex which shares a number of edges different to four. In the present work, we employ the constrained Bézier framework reported in [24] that forces the G^1 continuity in the one-ring neighbourhood elements adjacent to extraordinary points. The continuity is increased across the succeeding rings neighbourhood elements to reach the desirable C^2 continuity in the third-ring neighbourhood.

In degenerated elements, one of the edges of the quadrilateral element collapses in a point forming a triangular element. Usually, there are several elements that collapse in the same point (as in the typical case of a sphere). This point is called pole. The continuity across poles can be chosen to be C^0 if a continuous basis function is constructed as the sum of all the coincident basis functions. It should be consider that these elements become singular since the differentiability of the geometry vanishes when approaching to the degeneration. Therefore, it is not possible to compute the surface normal and the curvature in the poles. In computational analyses although these particular elements are admisibles, they are not desirable because they can affect to the accuracy of the results as well as they are sources of numerical problems [31, 58, 59]. Regarding that issue, we suggest to carry out a simple transformation to obtain non-singular elements. The procedure is as follows:

1. Given a degenerated cubic quadrilateral Bézier element defined by the homogeneous coordinates $\mathbf{Q}^w = \{w_i^b\mathbf{Q}_i, w_i^b\}_{i=1}^{m_b}$, the element is approximated

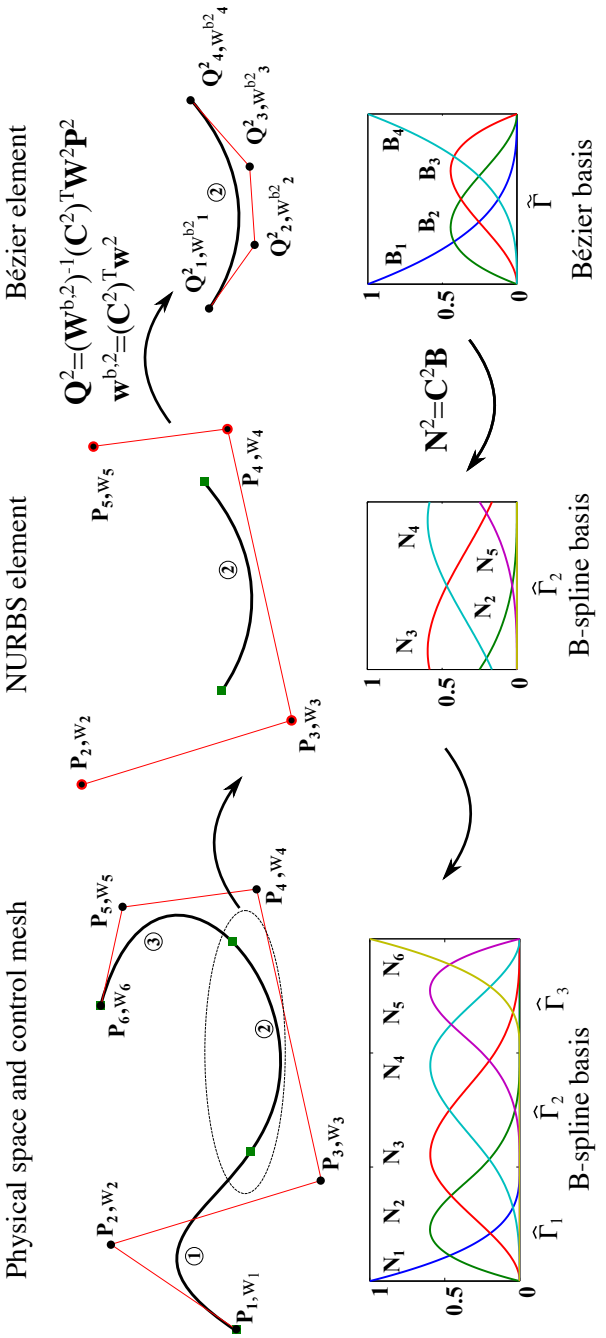

Figure 2.4: (a) Schematic illustration of the Bézier extraction operation applied to a cubic NURBS curve. (b) The Bézier extraction operator corresponding to the three Bézier elements.

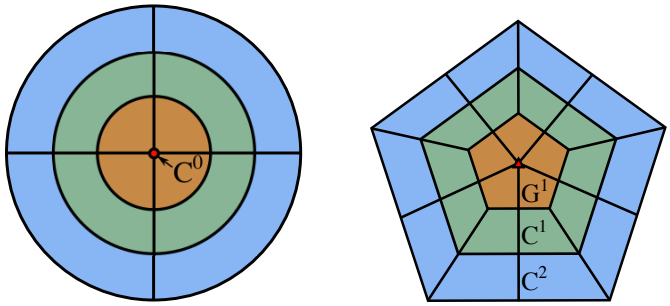

(a) (b)

Figure 2.5: Representation of (a) a structured mesh with degenerated elements and (b) a unstructured mesh. The pole is marked with a red circle and the start point with a red triangle. Each color strip corresponds to one ring of neighbour elements.

to a triangular cubic Bézier element $\mathbf{T}^w$. This operation can be expressed in a matrix form as,

$$\mathbf{T}^w = \mathbf{C}^{QT}\mathbf{Q}^w \tag{2.11}$$

In Eq. 2.11 $\mathbf{C}^{QT} \in \Re^{m_T \times m_b}$ is the matrix conversion from quadrilateral to triangular patch and $m_T = 9$ is the number of control points of the cubic triangular Bézier element. The triangular Bézier patch is not singular but its formulation and properties are different with respect to the standard quadrilateral Bézier patch. Therefore, that patch is not appropriated for the T-spline framework.

2. Then, the cubic triangular Bézier element is divided into three cubic non degenerated quadrilateral Bézier elements $(\widehat{\mathbf{Q}}_1^w, \widehat{\mathbf{Q}}_2^w, \widehat{\mathbf{Q}}_3^w)$ as follows,

$$\widehat{\mathbf{Q}}_i^w = \mathbf{C}_i^{TQ}\mathbf{T}^w \qquad i = 1, 2, 3 \tag{2.12}$$

where $\mathbf{C}_i^{TQ} \in \Re^{m_b \times m_T}$ are the conversion matrices from triangular Bézier patches to quadrilateral Bézier patches.

See Appendix B for a complete expansion of these matrix operations.

The original idea was developed for CAD systems in order to homogenize and unify the use of different Bézier formulations towards regular quadrilateral patches [60]. We extend that idea to the isogeometric analysis to avoid the presence of singular elements. Note that the first step produces an approximation of the original degenerated quadrilateral Bézier element since the number of control points

is reduced to a triangular Bézier element. To improve the geometrical approximation, a subdivision scheme can previously be applied to the first step and the discrepance can be controlled under a tolerance as shown in [60]. The second step generates a geometrically exact surface representation [61]. After this transformation, the one-ring neighbourhood Bézier elements around the poles are modified such that are C^0 with each other as well as with the adjoining two-ring neighbourhood elements. Although the continuity is locally reduced, it is enough to be used in the isogeometric analysis while the under-laying T-spline that supports them retains the continuity properties. Moreover, in the context of the Bézier-extraction, the above procedure is relatively easy to implement in the T-spline framework by a simple matrix multiplication of the matrix extraction operator with the transformation matrices. An schematic of the transformation process to non-degenerated Bézier elements is shown in Fig. 2.6.

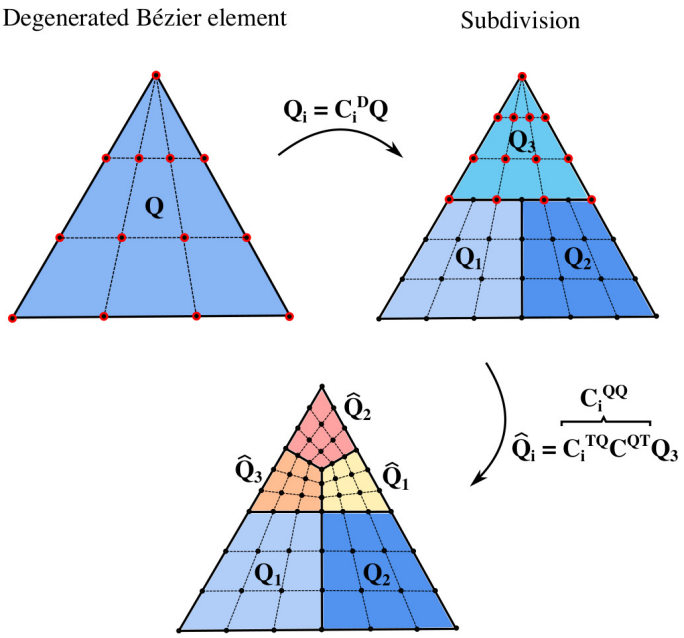

Figure 2.6: Schematic illustration of the transformation process from a cubic degenerated Bézier element to non degenerated cubic Bézier elements. A subdivision operation is previosly applied that is informed by the matrix operation C^D. The matrix C^{QQ} condenses the two cited operations to convert it to non degenerated Bézier elements. The matrices corresponding to this example are found in the Appendix C.

UNIVERSITAT ROVIRA I VIRGILI
TOWARDS THE APPLICATION OF THE ISOGEOMETRIC BOUNDARY ELEMENT ANALYSIS TO FLUID MECHANICS:
NON-LINEAR GRAVITY WAVES AND DYNAMICS OF DEFORMABLE CAPSULES IN SHEAR FLOWS
Jorge Maestre Heredia

Chapter 3

Wave propagation and wave-structure interaction

3.1 Introduction

In the last decades, numerical models have been developed for the prediction of the propagation of gravity waves in the time domain. These models have been applied to simulate tsunami generation and [62] overturning waves [1, 42, 43], to design breakwaters [63, 64], to predict the wave pressure impact on structures [65], or to study radiation and diffraction waves produced by a wave-maker [44, 66–68]. Nowadays, because of the increasing interest on the ocean renewable energy, in which the generation systems are installed near-shore or off-shore, new applications of such models are being used to study the fluid-structure interaction considering the effect of the waves [69–73].

Early numerical studies on the non-linear wave propagation appeared in 1976 when Longuet-Higguin and Cokelet [74] presented their bi-dimensional (2D) approach to simulate the transient surface waves. Their approach was based on the potential flow theory and used the BEM to solve the Laplace's equation in conjunction with a Mixed Eulerian-Lagrange (MEL) technique to update the free surface. Similar models were used to study a wide variety of non-linear water waves problems [75–79], but it was the study of Dommermuth et al. [49] that demonstrated the validity of the potential flow theory applied to the unsteady gravity wave propagation. These authors presented

a successful comparison between the numerical results obtained by a 2D-BEM model and experimental results obtained in a water tank. It is worth to mention the studies reported by Grilli et al. [1, 80, 81] who developed an advanced approach using 2D high order BEM. Later, Grilli et al. [42] and Guyenne and Grilli [43] extended the model to three-dimensional (3D) geometries to analyse overturning waves over an arbitrary bottom.

Some full non-linear high-order 3D BEM models have been proposed to simulate the unsteady interaction of the wave with a rigid body. An overview of such works can be found in Tanizawa [82]. Among them, Lee et al. [41] studied the non-linear waves and the hydrodynamic force generated by the movement of a submerged sphere. Bai and Taylor [44] investigated the wave radiation produced by a moving submerged truncated cylinder and the wave diffraction around a vertical cylinder [83]. They used an unstructured triangular mesh constructed with second order Lagrange elements in order to obtain a good approximation of the geometry. Later, these authors extended the model to flared floating structures [45]. Sung and Grilli [84] analysed the waves generated by an advancing surface disturbance. Following the Grilli's works, these authors used a structured mesh formed by isoparametric bi-cubic piecewise overlapping elements that provided a local smoothness of the geometry and of the physical variables. More recently, Hannan et al. [47, 85] studied the interactions between water waves and fully submerged fixed or moving structures. In the same line, but limited to 2D, Dombre et al. [48] extended the early work presented in [46] to study the dynamics of free fully submerged structures.

In addition, other models have been proposed to analyse more specific problems such as the post-breaking phenomenon, the violent wave impact against structures, the large fluid movement in a confined space with steep non-linear waves or the viscous and the vortex force in the context of floating structures. In such cases, the potential flow theory is not valid and other tools based on CFD solvers, to resolve the full Navier-Stokes equations, or the Lattice Boltzmann method (LBM) have been used [86–91]. Most of these problems have been formulated in 2D, and despite the increase of computational power, the full 3D models require a considerable computational cost. Therefore, unless in such specific cases, the potential theory together with BEM provides good results for non-linear gravity waves problems with a reduced computational time.

In this chapter we develop a 3D formulation of the the IGA-BEM based on the NURBS and T-spline framework to solve non-linear unsteady gravity wave

propagation problems and wave-structure interaction problems in the time domain. We consider the full non-linear potential flow theory in combination with the MEL procedure. We exploit the advantages of the IGA-BEM based on T-spline and NURBS basis in the context of the Bézier extraction procedure. The high continuity of the basis functions allows to deal with large mesh distortions [39] in the Lagrange formulation as well as it prevents numerical instabilities, as the saw-tooth effect that occurs when classical C^0 piecewise basis are used. In addition, we employ direct integration with CAD software [52] to make and handle 3D geometrical models in a easy way.

3.2 Formulation of the problem

We consider a fluid volume $\Omega(t)$ defined by an arbitrary lateral boundary $\Gamma_W(t)$, composed by one or several surfaces, a bottom surface $\Gamma_S(t)$ and a free surface $\Gamma_F(t)$ located at the top. The fluid can move freely with the time (t) by the action of a submerged moving rigid body $\Gamma_B(t)$ or by imposing a specific initial condition. In Fig. 3.1 we show a sketch of the domain and the Cartesian coordinate adopted. The plane $z = 0$ corresponds to the free surface at rest.

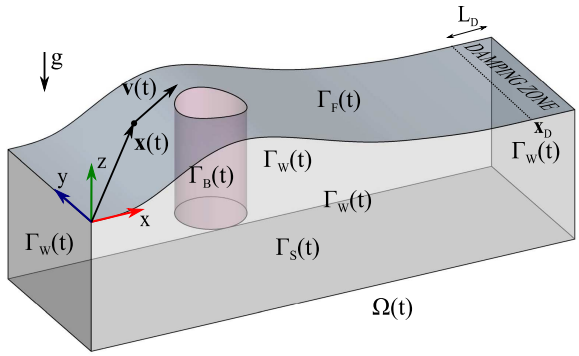

Figure 3.1: Sketch of the problem

The flow is assumed to be incompressible, inviscid and irrotational. Under these hypotheses, the movement of a fluid particle $\mathbf{x}(t)$ can be described in terms of a velocity potential $(\phi(x, y, z, t))$, such that the velocity of a fluid particle can be expressed as:

$$\mathbf{v} = \boldsymbol{\nabla}\phi \tag{3.1}$$

The continuity equation in the a fluid domain $\Omega(t)$ can be reduced to a Laplace equation:

$$\nabla^2\phi = 0 \qquad \text{in } \Omega(t) \tag{3.2}$$

that is subjected to different boundary conditions on the surfaces $\Gamma(t)$ that define the domain.

On the free surface $\Gamma_F(t)$, the kinematic and dynamic conditions in the Lagrangian description are expressed as:

$$\frac{D\mathbf{x}}{Dt} = \boldsymbol{\nabla}\phi \qquad \text{on } \Gamma_F(t) \tag{3.3}$$

$$\frac{D\phi}{Dt} = -gz + \frac{1}{2}\boldsymbol{\nabla}\phi\cdot\boldsymbol{\nabla}\phi - \frac{p_a}{\rho} \qquad \text{on } \Gamma_F(t) \tag{3.4}$$

respectively. In Eqs. (3.3-3.4) D/Dt denotes the material derivative, g is the gravity acceleration, p_a is the atmospheric pressure and ρ is the density of the fluid.

The instantaneous kinematic conditions on the lateral boundaries $\Gamma_W(t)$, the bottom $\Gamma_S(t)$ and wetted body surfaces $\Gamma_B(t)$ are:

$$\frac{\partial\phi}{\partial n} = 0 \qquad \text{on } \Gamma_W(t) \text{ and } \Gamma_S(t) \tag{3.5}$$

$$\frac{\partial\phi}{\partial n} = \mathbf{v}_B\cdot\mathbf{n} \qquad \text{on } \Gamma_B(t) \tag{3.6}$$

with $\mathbf{n}$ the normal pointing out of fluid and $\mathbf{v}_B$ the velocity vector of the rigid body. In the case of a free floating body, the velocity should be computed using the second Newton's law. Here we consider the rigid body motion given by $\mathbf{v}_B = \dot{\mathbf{x}}_G + \dot{\boldsymbol{\theta}}_G \times \mathbf{r}_B$, where $\dot{\mathbf{x}}_G$ and $\dot{\boldsymbol{\theta}}_G$ are the velocity and rotation vectors referred to the center of mass, and $\mathbf{r}_B = \mathbf{x}_B - \mathbf{x}_G$ is the location of a body particle with respect to the center of mass.

As it can be noted in the formulation expressed above, the lateral boundaries are considered solid and impermeable. This means that waves are reflected and kept into the domain as it would occur in a tank. In some cases treated in this study, we are interested in the simulation of infinite domains. For these cases, an artificial damping method is used to absorb the wave energy near the boundaries [44, 92]. This is done by modifying the kinematic and dynamic boundary conditions over a finite zone of the

free surface, known as damping zone, located near the boundaries as follows:

$$\frac{D\mathbf{x}}{Dt} = \boldsymbol{\nabla}\phi - \varsigma(\mathbf{x})(\mathbf{x} - \mathbf{x}_0) \qquad \text{on } \Gamma_F(t) \tag{3.7}$$

$$\frac{D\phi}{Dt} = -gz + \frac{1}{2}\boldsymbol{\nabla}\phi \cdot \boldsymbol{\nabla}\phi - \frac{p_a}{\rho} - \varsigma(\mathbf{x})(\phi - \phi_0) \qquad \text{on } \Gamma_F(t) \tag{3.8}$$

where $\mathbf{x}_0$ and ϕ_0 are reference values at the rest state, and $\varsigma(\mathbf{x})$ is the damping factor, which is gradually increasing along the damping zone as:

$$\varsigma(\mathbf{x}) = \begin{cases} \alpha \left(\frac{l_D(\mathbf{x})}{L_D}\right)^2 & \text{in the damping zone} \\ 0 & \text{otherwise} \end{cases} \tag{3.9}$$

In Eq. 3.9, $\alpha \in \Re_{\geq 0}$ is the maximum damping factor, L_D is the length of the zone and $l_D(\mathbf{x})$ is the distance between $\mathbf{x}_D$ and the specific location considered in vertical projection (see Fig. 3.1).

3.3 Formulation of the method

3.3.1 Isogeometric Boundary Element Method

Given the domain $\Omega(t)$ delimited for a piecewise smooth boundary $\Gamma(t)$, the external Boundary Integral Equation (BIE) applied to the potential problem can be written as:

$$\mathfrak{C}(\mathbf{x}_0)\phi(\mathbf{x}_0, t) = \int_{\Gamma(t)} \left[\mathfrak{G}(\mathbf{x}, \mathbf{x}_0)\frac{\partial\phi(\mathbf{x}, t)}{\partial n}\right] d\Gamma$$
$$- \fint_{\Gamma(t)} \left[\phi(\mathbf{x}, t)\frac{\partial\mathfrak{G}(\mathbf{x}, \mathbf{x}_0)}{\partial n}\right] d\Gamma \tag{3.10}$$

The symbol $\fint$ denotes that the integral is evaluated in the Cauchy Principal Value sense (CPV), $\mathfrak{C}(\mathbf{x}_0)$ is the solid angle defined at the source point $\mathbf{x}_0 \in \Gamma$, that can be calculated directly with the expression proposed by Mantic [93] or indirectly as described in Section 3.3.2, and $\mathfrak{G}(\mathbf{x}, \mathbf{x}_0)$ is the fundamental solution of the Laplace's problem. In the examples treated here, we consider three possible orthogonal symmetric planes parallel to the Cartesian planes, such that the geometric complexity

and computational costs can be reduced. Using the method of the images, the Green function can be expressed as:

$$\mathfrak{G}(\mathbf{x},\mathbf{x}_0) = \frac{-1}{4\pi}\sum_{i=1}^{8}\left[\frac{1}{\|\mathbf{x}-\mathbf{x}\prime_i\|}\right] \tag{3.11}$$

where:

$$\begin{cases} \mathbf{x}\prime_1 = \mathbf{x}_0 \\ \mathbf{x}\prime_2 = \{x_0, y_0, 2z_{sym} - z_0\} \\ \mathbf{x}\prime_3 = \{x_0, 2y_{sym} - y_0, z_0\} \\ \mathbf{x}\prime_4 = \{x_0, 2y_{sym} - y_0, 2z_{sym} - z_0\} \\ \mathbf{x}\prime_5 = \{2x_{sym} - x_0, y_0, z_0\} \\ \mathbf{x}\prime_6 = \{2x_{sym} - x_0, y_0, 2z_{sym} - z_0\} \\ \mathbf{x}\prime_7 = \{2x_{sym} - x_0, 2y_{sym} - y_0, z_0\} \\ \mathbf{x}\prime_8 = \{2x_{sym} - x_0, 2y_{sym} - y_0, 2z_{sym} - z_0\} \end{cases} \tag{3.12}$$

with $x = x_{sym}$, $y = y_{sym}$ and $z = z_{sym}$ being the location of the symmetric planes.

Considering an Isogeometric Analysis (IGA), the variables introduced in the BIE (i.e. the potential and the flux) are defined in a finite dimensional space given by the same basis functions than the geometry. This provides the BIE variables and the geometry the intrinsic properties of the T-spline (or NURBS) as demonstrated in the previous chapter. The BIE variables can be written as:

$$\phi^e(\tilde{\boldsymbol{\xi}}, t) = \mathbf{R}^e(\tilde{\boldsymbol{\xi}})^T \boldsymbol{\phi}^e(t) \tag{3.13}$$

$$\frac{\partial \phi^e}{\partial n}(\tilde{\boldsymbol{\xi}}, t) = q^e(\tilde{\boldsymbol{\xi}}, t) = \mathbf{R}^e(\tilde{\boldsymbol{\xi}})^T \boldsymbol{q}^e(t) \tag{3.14}$$

where $\boldsymbol{\phi}^e(t) = \{\phi^e_a(t)\}_{a=1}^{m_e}$ and $\boldsymbol{q}^e(t) = \{q^e_a(t)\}_{a=1}^{m_e}$ are the temporal potential and temporal flux vector corresponding to the local basis functions of each element, respectively.

Introducing Eqs. 3.13 and 2.7 into Eq. 3.10, and applying the result on a particular source point $\mathbf{x}_i^{e_i} = \mathbf{R}_i^{e_i}(\tilde{\boldsymbol{\xi}}_i^{e_i})^T \mathbf{P}^{e_i}$ contained in the element e_i, we obtain the discrete IGA BIE:

$$\begin{aligned} \mathfrak{C}(\mathbf{x}_i^{e_i})(\mathbf{R}_i^{e_i})^T \boldsymbol{\phi}^{e_i} = \sum_{e=1}^{N} \Bigg[& \int_{\Gamma^e(t)} \left[\mathfrak{G}(\mathbf{x}^e, \mathbf{x}_i^{e_i})(\mathbf{R}^e)^T \boldsymbol{q}^e\right] \left|\frac{\partial \mathbf{x}^e}{\partial \tilde{\boldsymbol{\xi}}}\right| d\Gamma(\tilde{\boldsymbol{\xi}}) \\ & - \fint_{\Gamma^e(t)} \left[(\mathbf{R}^e)^T \boldsymbol{\phi}^e \frac{\partial \mathfrak{G}(\mathbf{x}^e, \mathbf{x}_i^{e_i})}{\partial n}\right] \left|\frac{\partial \mathbf{x}^e}{\partial \tilde{\boldsymbol{\xi}}}\right| d\Gamma(\tilde{\boldsymbol{\xi}}) \Bigg] \end{aligned} \tag{3.15}$$

In Eq. 3.15 $\left|\frac{\partial \mathbf{x}^e}{\partial \tilde{\boldsymbol{\xi}}}\right|$ is the Jacobian determinant of the geometrical mapping, N is the number of elements. For more details about the calculation of the Jacobian and the tangential derivatives, the reader is referred to [23, 57]. Hereinafter, we drop the upper index e_i and for convenience we keep the subindex i to refer to the source point.

In this study we employ a collocational method, such that the BIE must be satisfied for a set of $i = 1, 2, ..., m_{cp}$ specific source points known as collocation points. Particularly, we use a generalization of the Greville abscissae as presented in Scott et al. [24], since it provides accurate results in the context of the IGA BEM. However, we relax the continuity condition for the position of control points such as these are allowed to lie in sharp edges and corners. As demonstrated in [31], this relaxation does not reduce the accuracy of the results and it facilitates the special treatment of the velocity in these locations, as shown in Section 3.3.4.

3.3.2 Numerical integration

It is well known that the first and second kernel of the BIE (see Eq. 3.10) contain a weak and a strong singularity, respectively, when the point of evaluation approaches to the collocation point. The integrals are defined, but they have to be suitably evaluated to avoid numerical problems. This topic has been studied intensively and an overview of the available techniques can be found in [94–104].

In this study we regularize the second kernel using the rigid body method [94, 104], that provides an indirect way to calculate the jump term as:

$$\mathfrak{C}(\mathbf{x}_0) = -\!\!\!\!\!\!\int_{\Gamma(t)} \frac{\partial \mathfrak{G}(\mathbf{x}, \mathbf{x}_0)}{\partial n} d\Gamma \tag{3.16}$$

Introducing Eq. 3.16 in Eq. 3.10 gives:

$$\int_{\Gamma(t)} \left[(\phi(\mathbf{x}, t) - \phi(\mathbf{x}_0, t)) \frac{\partial \mathfrak{G}(\mathbf{x}, \mathbf{x}_0)}{\partial n} \right] d\Gamma = \int_{\Gamma(t)} \left[\mathfrak{G}(\mathbf{x}, \mathbf{x}_0) \frac{\partial \phi(\mathbf{x}, t)}{\partial n} \right] d\Gamma \tag{3.17}$$

Note that this regularization technique avoids the computation of the CPV and the jump term in Eq. 3.15, and both integrals are weakly singular. The weak singularity is solved using a local change of variables over the element containing the collocation point, as proposed by Lachat and Watson [95]. Once regularized, these kernels can be numerically evaluated by applying the quadrature rule to each element in the parent

domain. We use the standard Gauss-Legendre quadrature. Recently, new specific quadrature rules for NURBS have been proposed to take into account the continuity of the basis functions [96]. In addition, if the collocation point is not located on the element but very close, the integrals become nearly singular and their calculation can exhibit numerical instability. In these cases, we use an adaptive regular element subdivision on the parent domain.

3.3.3 System of equations

The discretization of the BIE in all collocation points leads to a set of m_{cp} equations with $2m_{cp}$ variables corresponding to the potential and the flux at the control points. This set of equations can be written compactly as,

$$\hat{\boldsymbol{\mathcal{H}}}\boldsymbol{\phi} = \boldsymbol{\mathcal{G}}\mathbf{q} \tag{3.18}$$

in which, using the global notation, $\boldsymbol{\phi} = \{\phi\}_{A=1}^{m_{cp}}$ is the potential vector, $\mathbf{q} = \{q\}_{A=1}^{m_{cp}}$ is the flux vector, and the matrices $\hat{\boldsymbol{\mathcal{H}}}$ and $\boldsymbol{\mathcal{G}} \in \Re^{m_{cp}\times m_{cp}}$ are given by:

$$\hat{\boldsymbol{\mathcal{H}}}_{iA} = \int_{\Gamma(t)} \frac{\partial \mathfrak{G}(\mathbf{x}, \mathbf{x}_i)}{\partial n} \left(R_A(\mathbf{x}) - R_A(\mathbf{x}_i)\right) d\Gamma \tag{3.19}$$

$$\boldsymbol{\mathcal{G}}_{iA} = \int_{\Gamma(t)} \mathfrak{G}(\mathbf{x}, \mathbf{x}_i) R_A(\mathbf{x}) d\Gamma \tag{3.20}$$

As it has been shown in Section 3.2, the problem under consideration consists in a mixed boundary problem in which the potential, once integrated in time, is known on the free surface and its flux on the rest of the boundaries. The discretization of the boundary conditions on the set of collocation points yields,

$$\mathbf{R}(\mathbf{x}_i)^T \boldsymbol{\phi} = \bar{\phi}(\mathbf{x}_i) \qquad \forall \mathbf{x}_i \in \Gamma_F(t) \tag{3.21}$$

$$\mathbf{R}(\mathbf{x}_i)^T \mathbf{q} = \bar{q}(\mathbf{x}_i) \qquad \forall \mathbf{x}_i \in \Gamma_W(t) \cup \Gamma_S(t) \cup \Gamma_B(t) \tag{3.22}$$

We reorder the system of equations (3.18), (3.21) and (3.22) to obtain a linear system that can be written as $\mathbf{Ka} = \mathbf{b}$, where $\mathbf{a} \in \Re^{2m_{cp}}$ is a vector containing the control variables, $\mathbf{b} \in \Re^{2m_{cp}}$ is a vector with the boundary conditions at the collocation points and $\mathbf{K} \in \Re^{2m_{cp}\times 2m_{cp}}$ is in general a dense non-symmetric matrix. The minimum residual method (GMRES) has been found to be efficient and suitable for solving the

system of equations [44, 105]. In the present study the tolerance has been set to 10^{-12}. Moreover, to correctly model the physical variables at the sharp edges and corners, we use the semi-discontinuous basis technique, as presented in [24], such that the flux is allowed to be discontinuous while the potential is continuous. Fig3.2 shown an example of the collocation points strategy used in the present work.

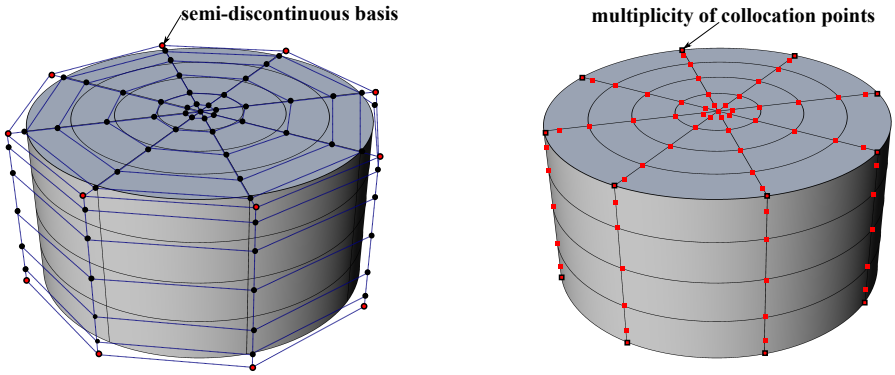

Figure 3.2: T-spline model for a cylindrical tank: (a) control point positions and (b) collocation points positions. In both cases the Bézier elements are represented. On sharp edges the semi-discontinuous basis technique is used (highlight circles). The potential is continuous whereas the flux is allowed to be discontinuous across the edges that requires adding collocations points on the edges (highlight quadrilateral). This technique is known as multiplicity of control points.

3.3.4 Velocity field

Following the idea of the IGA, we use the same set of T-spline (or NURBS) basis functions to approximate the velocity field, which is expressed as,

$$\mathbf{v}(\tilde{\boldsymbol{\xi}}, t) = \mathbf{R}(\boldsymbol{\xi})^T \mathbf{v}(t) \tag{3.23}$$

where $\mathbf{v}(t) = \{\mathbf{v}_A(t)\}_{A=1}^{m_{cp}}$ is the global velocity vector.

The global velocity vector has not a real physical meaning and it represents a fictitious velocity which is used to calculate the real velocity field. Using a collocation method this global velocity vector can be computed as:

$$\mathbf{v}(t) = \boldsymbol{\mathcal{T}}^{-1} \boldsymbol{\mathcal{V}} \tag{3.24}$$

In Eq. 3.24 $\boldsymbol{\mathcal{V}} = \{\mathbf{v}_i(\boldsymbol{\xi}_i, t)\}_{i=1}^{m_{cp}}$ is the velocity vector at the collocation points and $\boldsymbol{\mathcal{T}}_{iA} = R_A(\mathbf{x}_i)$ is the invertible and well conditioned interpolation matrix.

An ambiguous definition of the local velocity can be found in the collocation points located in sharp edges or corners due to the discontinuity of the derivatives. This ambiguity is a source of numerical instabilities and it should be solved to obtain a continuous velocity field. An usual procedure to overcome this problem is the calculation of an average velocity [44]. In this work we employ an alternative procedure that consists in the determination of a unique velocity, which is compatible with the normal velocity of each concurrent surface. We consider two possible cases as shown in Fig. 3.3. The first one (Fig. 3.3a) corresponds to a corner at the intersection of three surfaces. In this case, the velocity can be determined using the following equation:

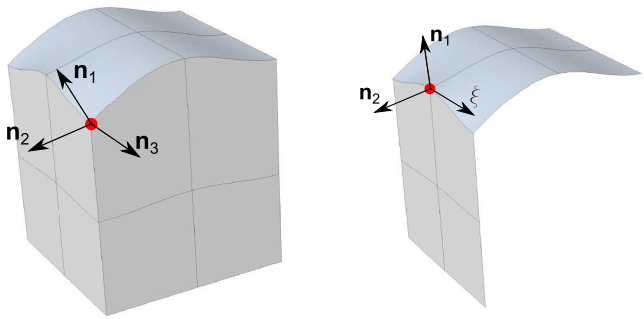

(a) (b)

Figure 3.3: (a) Corner at the intersection of three surfaces and (b) edge defined by the intersection two surfaces.

$$\begin{bmatrix} v_x \\ v_y \\ v_z \end{bmatrix} = \begin{bmatrix} n_x^1 & n_y^1 & n_z^1 \\ n_x^2 & n_y^2 & n_z^2 \\ n_x^3 & n_y^3 & n_z^3 \end{bmatrix}^{-1} \begin{bmatrix} \frac{\partial \phi}{\partial n^1} \\ \frac{\partial \phi}{\partial n^2} \\ \frac{\partial \phi}{\partial n^3} \end{bmatrix} \tag{3.25}$$

where n^i are the normals corresponding to each surface.

The second case (Fig. 3.3b) is found in the edge defined by the intersection of two surfaces. The velocity can be computed as,

$$\begin{bmatrix} v_x \\ v_y \\ v_z \end{bmatrix} = \begin{bmatrix} n_x^1 & n_y^1 & n_z^1 \\ n_x^2 & n_y^2 & n_z^2 \\ \frac{\partial x}{\partial \xi} & \frac{\partial y}{\partial \xi} & \frac{\partial z}{\partial \xi} \end{bmatrix}^{-1} \begin{bmatrix} \frac{\partial \phi}{\partial n^1} \\ \frac{\partial \phi}{\partial n^2} \\ \frac{\partial \phi}{\partial \xi} \end{bmatrix} \tag{3.26}$$

In Eq. (3.26) ξ represents the common axis along the direction of the edge. Note that, since ϕ is continuous, its derivative along the edge is unique.

3.3.5 Hydrodynamic pressure

The pressure force, $\hat{\mathbf{f}} = [f_x, f_y, f_z, \mathsf{m}_x, \mathsf{m}_y, \mathsf{m}_z]$, exerted by the fluid on the surface of a body can be computed as,

$$\hat{\mathbf{f}} = \int_{\Gamma_B(t)} p\hat{\mathbf{n}} d\Gamma \tag{3.27}$$

where $\hat{\mathbf{n}} = [\mathbf{n}, \mathbf{r}_B \times \mathbf{n}]$ is a six-component vector. The pressure field at any point can be calculated using the Bernoulli equation:

$$p = -\rho \left(\frac{\partial \phi}{\partial t} + gz + \frac{1}{2} \boldsymbol{\nabla}\phi \cdot \boldsymbol{\nabla}\phi \right) \tag{3.28}$$

The term $\frac{\partial \phi}{\partial t}$ can be approximated by using temporal integration schemes. However, this can produce numerical instabilities. Dombre et al. [42, 48] proposed a method to compute directly this term using an auxiliary BIE. This method requires the calculation of second derivatives of the potential and the geometry variables that leads to complex formulations. Here we use the method proposed by Wu and Taylor [106] in which the $\frac{\partial \phi}{\partial t}$ is calculated indirectly such as the pressure force vector is given as:

$$\begin{aligned} \hat{f}_i/\rho = &- \int_{\Gamma_B(t) \cup \Gamma_F(t)} \frac{\partial \psi_i}{\partial n} \left(gz + \frac{1}{2} \boldsymbol{\nabla}\phi \cdot \boldsymbol{\nabla}\phi \right) d\Gamma - \int_{\Gamma_B(t)} \psi_i \left(\hat{\mathbf{a}}_b \cdot \mathbf{n} \right) d\Gamma \\ &+ \int_{\Gamma_B(t)} \boldsymbol{\nabla}\psi_i \left(\mathbf{v}_B \cdot \mathbf{n} \right) \cdot \left(\boldsymbol{\nabla}\phi - \mathbf{v}_B \right) d\Gamma \end{aligned} \tag{3.29}$$

In Eq. 3.29 $\mathbf{v}_B$ is the velocity of the body, as defined in Section 3.2, $\hat{\mathbf{a}}_B = \ddot{\mathbf{x}}_G + \ddot{\boldsymbol{\theta}}_G \times \mathbf{r}_B - \dot{\boldsymbol{\theta}}_G \times \dot{\mathbf{x}}_G$ and ψ_i are six auxiliary functions ($i = 1, 2, ..., 6$) that satisfy the Laplace equation. These new variables can be computed using an auxiliary BIE as following:

$$\begin{cases} \nabla^2 \psi_i = 0 & \text{in } \Omega(t) \\ \psi_i = 0 & \text{on } \Gamma_F(t) \\ \frac{\partial \psi_i}{\partial n} = 0 & \text{on } \Gamma_W(t) \text{ and } \Gamma_S(t) \\ \frac{\partial \psi}{\partial n} = \hat{n}_i & \text{on } \Gamma_B(t) \end{cases} \tag{3.30}$$

3.3.6 Time marching

As shown in the formulation of the problem, the position of the fluid particles and the physical variables, Eq. 3.3 and Eq. 3.4, depend on time. Therefore, to obtain the temporal evolution of the free surface, a temporal integration scheme is needed. In the context of strong non-linear gravity waves, several schemes have been proposed [42, 45, 92, 107]. In this study, we use the standard 4th order Runge Kutta method (RK4), which has been shown to be numerically stable and accurate.

An important aspect of the temporal integration is the adequate selection of the time step to provide an accurate and stable temporal resolution. This depends on the integration scheme, physical discretization and the particular problem under consideration. For periodic wave problems the time step is usually chosen as a fraction of the wave period such that the physical phenomenon is represented accurately [92]. For a solitary wave, Grilli et al. [42] proposed an adaptive time steeping method as a function of the spatial discretization and the Courant number, $\mathcal{C}$ (Eq. 3.31). They demonstrated that there exists an optimal Courant number such that the error is minimum. We use this method, adapted to the IGA-BEM, and investigate about the optimal value of the Courant number.

$$\Delta t = \mathcal{C} Le_{min} / \sqrt{gh} \tag{3.31}$$

In Eq 3.31 Le_{min} is the minimum characteristic element size defined as the square root of its surface and h is the depth of the bottom surface.

The steps for the time marching procedure are:

1. The initial geometrical model is defined and an initial boundary condition for the potential ($\bar{\phi}_0$) and the flux ($\bar{q}_0$) are specified on the free surface and on the rest of the surfaces, respectively.

2. A time step (Δt_i) is selected. This can be set dynamically at each step depending on the type of problem.

3. The time integration is carried out to update the position of the fluid particles and potential (ϕ_{i+1}, $\mathbf{x}_{i+1}$) from the actual time (t_i) to the next time step ($t_{i+1} = t_i + \Delta t_i$). Due to the non-linear behaviour, several sub-steps are required.

3.1. The BIE equation (3.18) is calculated, and the boundary conditions (Eq. 3.21 and Eq. 3.22) are applied at the each sub-step (k). A linear system of equations is obtained and solved by using the GMRES.

3.2. The velocity is computed using Eq. 3.23.

3.3. The potential is updated to the next sub-step (ϕ_{i+1}^{k+1}) by applying the integration scheme to the kinematic relation for the free surface (Eq. 3.3 or Eq. 3.8).

3.4. The positions of the fluid particles are updated to the next sub-step ($\mathbf{x}_{i+1}^{k+1}$) using the known velocity field. If fluid particles are separated from the walls or body surface, these are relocated back to the boundaries using a normal projection as proposed by Bai and Taylor [44].

3.5. The flux is computed in the next sub-step (q_{i+1}^{k+1}) using the kinematic equations for the walls, bottom surface, and body surface.

3.6. For the RK4 scheme, this process is repeated four times ($k = 1$ to $k = 4$).

4. The fluid forces on the body are computed (Eq. 3.28 and Eq. 3.27).

5. The volume and total energy is calculated in order to monitor their temporal evolution as,

$$\mathbb{v}(t) = \int_{\Gamma(t)} z(\boldsymbol{\lambda}_z \mathbf{n}) d\Gamma \tag{3.32}$$

$$e(t) = \frac{\rho g}{2} \int_{\Gamma(t)} z^2(\boldsymbol{\lambda}_z \mathbf{n}) + \phi q d\Gamma \tag{3.33}$$

where $\boldsymbol{\lambda}_z$ is the unit vertical vector.

6. Steps 2 to 5 are carried out iteratively until the maximum time is reached.

It should be noted that we are employing a collocational method and all variables are evaluated at the collocations points. The values of the variables on the control points can be obtained using the interpolation matrix.

3.4 Numerical Results

In this section we show some numerical examples to validate the present IGA-BEM formulation. Each example is focused on a particular computational aspect of the method. The first example is a train of small amplitude waves and we analyse the spatial convergence of the IGA-BEM solution. In the next example we simulate a solitary wave to evaluate the temporal stability and the accuracy of the method. In the third example we check the ability of the method to handle wave-structure problems by simulating the waves generated in a tank. Finally, we simulated the waves generated by moving submerged foils. This configuration has technological implications such as is the generation of waves in surf parks.

All T-spline models were constructed using the T-spline plugin of Rhino [52]. In the first three examples, the free surface is specified by a known function and the approximation using NURBS surfaces is not straightforward. In order to obtain the optimal approximation, a L^2-projection method is used. It consists in the minimization of the L^2-error between the given function f and its projections in a discrete space of spline basis functions (Λ). This is:

$$min\|f - \Pi[\Lambda](f)\|_{L_2} \tag{3.34}$$

in which the projection $\Pi[\Lambda](f)$ is given by:

$$\Pi[\Lambda](f) = \mathbf{R}_A^T \boldsymbol{\alpha}(f) \tag{3.35}$$

and $\boldsymbol{\alpha}(f)$ are the functionals to be found such that the L^2-error is minimized.

In all the examples considered the body is rigid. Symmetric boundary conditions are imposed at the symmetric planes of the problems. These planes have the zero flux condition and they are not discretized because symmetric conditions are implicitly incorporated in the Green function. Moreover, unless otherwise is specified, the time is made dimensionless using the time scale $\sqrt{h/g}$ with h being the depth of the water. The dimensionless variables are denoted with *.

3.4.1 Periodic wave: convergence of the spatial discretization

The objective of this example is to analyse the convergence of the IGA-BEM method presented in this study. The test consists in the simulation of a steadily propagation of a

periodic train of non-linear waves over a horizontal bottom surface. This problem has been studied by some authors [108–111]. Fenton proposed an approximation based on fifth-order Stokes theory, which assumes that all variations along the propagation direction can be represented by Fourier series. For more details see [110].

This is a 2D periodic problem where the gravity waves propagate along the x-direction and they are invariant along y-direction. Since the presented method is formulated in 3D, we study a representative domain (Ω) defined by its length $x = [-\lambda/2, \lambda/2]$, depth $z = [0, \eta]$ and width $y = [0, h]$, where λ is the wavelength and η is the elevation of the wave. The problem is closed setting the wave-number $Kh = 2\pi h/\lambda = \pi/2$, the wave height $A/h = 0.2$ and wave velocity $c = Q/h$, where Q is the vertical volume rate of flow that can be calculated by the fifth-order Stokes theory.

Considering three symmetry planes; located at $x = \lambda/2$, $y = h$ and $z = 0$; the geometry is discretized with three NURBS surfaces. Note that these surfaces can be converted into a unique T-spline patch. We set a number of regular Bézier elements that varies between 12 to 24 with an increment of 4 elements per wavelength along the three spatial directions. All weights are set to unity. Moreover, three different degrees for the basis ($p = 2, 3, 4$) are selected.

It should be noted that sinusoidal functions cannot be represented exactly by a rational spline, and numerical errors are expected to occur on the geometry and boundary conditions. To minimize these errors we use a L^2-projection method as explained above. Fig. 3.4a shows the L^2-error on the free surface. It can be seen that the model shows an optimal convergence (i.e. convergence rate $\geq p + 1$).

In Fig. 3.5 we show the point-wise error, between the analytical and numerical IGA-BEM solution ($\|w - w^h\|$ with w^h being the flux or potential), on the free surface for the more refined model using quartic basis. The error on the Neumann boundaries is considerable lower (one order of magnitude smaller) than on the Dirichlet boundary (free surface). Moreover, small fluctuations are detected near the intersections of the free surface due to lateral boundary effects. The convergence study is given in Fig. 3.6 where an optimal ratio is shown for all the polynomial degrees.

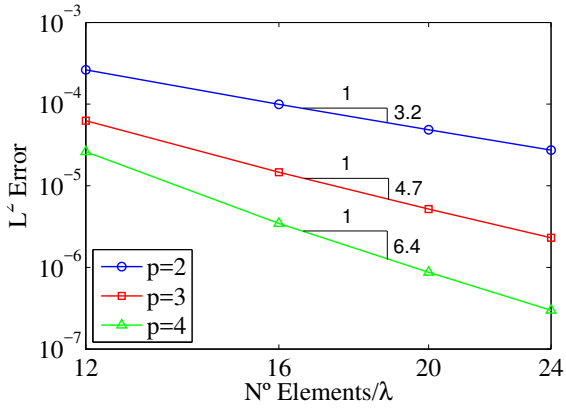

(a)

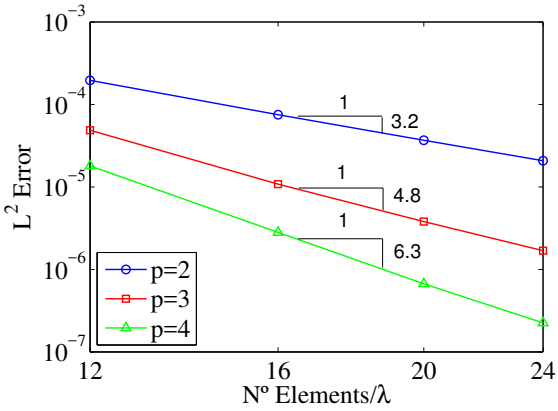

(b)

Figure 3.4: (a) L^2-Error between the analytical elevation function and the NURBS surface that represents the free surface. (b) L^2-Error between the analytical potential function and the boundary conditions applied on the free surface.

3.4.2 Solitary wave: temporal accuracy

Our next benchmark example consists in a solitary wave propagating over constant depth. This example has been studied by Tanaka [112], who obtained a 2D full non-linear numerical solution, and used by other authors for validation purposes [42, 81, 113]. In this subsection we analyse the temporal stability and accuracy of the present method by computing the numerical errors along the time with respect to the steady solution presented by Dutykh and Clamond [113].

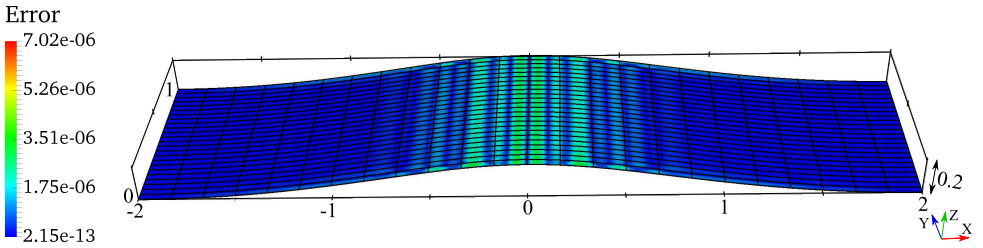

Figure 3.5: Point-wise error between the analytical and numerical (IGA-BEM) solutions on the free surface using quartic basis functions and 24 elements/λ.

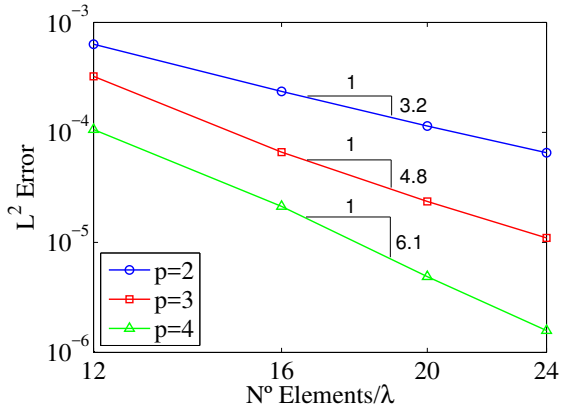

Figure 3.6: L^2-Error between the analytical and numerical (IGA-BEM) solutions on the free surface.

We consider a wave of amplitude $A = 0.6h$, where h is the depth of the free surface at the rest. The domain is given by a length $x = [0, 20h]$, width $y = [0, 2h]$ and depth $z = [0, -h]$. The wave is propagated along the longitudinal direction (x-direction) and at the initial stage the crest is located at $x = 7.5h$.

As in the previous example, we set three symmetric planes at $x = 20h$, $y = 2h$ and $z = -h$ and the model is represented by three NURBS surfaces with weight unity. The free surface elevation and the potential are established with the L^2-projection method applied over the solution proposed by Dutykh and Clamond [113]. We consider two longitudinal discretizations with element lengths of 0.25 and 0.5. The element length along y-direction is 0.5 and 0.25 along z-direction. We use quadratic and cubic NURBS basis functions. Moreover, simulations with an equivalent model using the standard quadratic Lagrangian basis functions has been performed for comparison.

We carried out some simulations for different Courant numbers (calculated based on the length of the elements of the free surface along x-direction, given the invariance

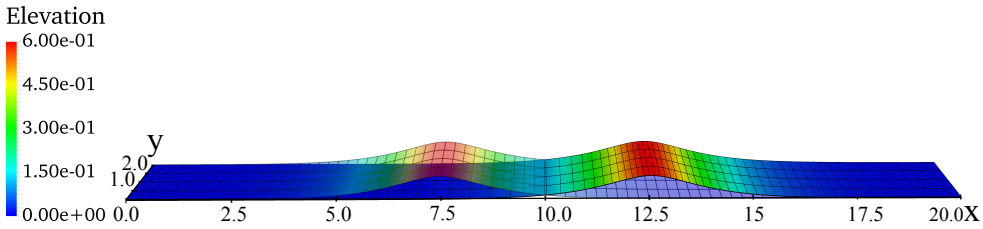

Figure 3.7: Time evolution of the wave shape. The translucent surface correpond to he initial condition and the solid surface to $t^* = 4$. Simulation with the fine mesh using cubic NURBS basis functions.

along y-direction) in the range of $0.3 \leq \mathcal{C} \leq 1.0$. The instantaneous shape, energy and volume of the wave have been monitored during a period of $\Delta t^* = 4$. We found that the wave is kept stable during the simulation for all cases and the elements are concentrated around the crest, as it can be seen in Fig.3.7. Moreover, the average errors are mostly constant for the complete range of Courant numbers considered (Fig.3.8). This demonstrates the robustness and stability of the scheme of integration.

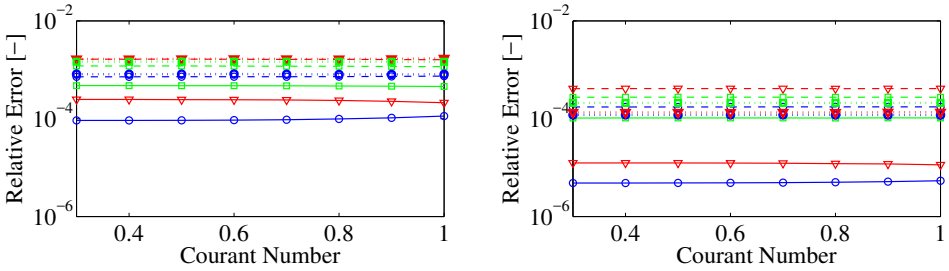

Figure 3.8: Relative energy (triangle), volumen (circle) and shape (square) errors for a cubic NURBS (continuouos line), quadratic NURBS (dash line) and cuadratic Lagrangian (dotted line) model, for (a) the case of a coarse mesh and (b) the fine mesh .

We have also analysed the numerical stability of the same solitary wave propagating over a 1:15 slope that starts at the initial position of the crest ($x = 7.5h$). This configuration, that produces the overturn of the wave, was studied in detail by Grilli et al. [1] using a 2D BEM mode. Later these results were used to validate a 3D BEM formulation [42].

Here we consider the numerical model described above for the fine mesh and a Courant number of 0.5. Additionally, we discretize the bottom surface with the same

number of uniform elements as the free surface and we extend the length of domain up to $x = 22h$. The simulation is carried out until the wave reaches the breaking point (at $t^*_{BP} = 7.78$). At larger times the lateral mesh becomes very distorted and the numerical errors increase very fast. In fact, for the quadratic Lagrange model, numerical instabilities appear before (at $t^* = 7.11$), as it can be observed in Fig. 3.9a, and the simulation stops. This problem is associated with the lack of smoothness across the elements that produces a sawtooth effect near the crest. The calculation of the dynamic and kinematic conditions depends on the gradient of the potential, that is not unique in shared nodes between neighbour elements. An average of the gradient is taken in these nodes. This introduces numerical errors which increase with time. These errors are more important in regions with a large variation of the potential, as well as, in elements considerably distorted. Eventually, the growth of these errors cause a premature stop of the simulation. These instabilities have been also reported by some authors [38, 44, 114] and some stabilization techniques have been proposed. However, the models using NURBS are stable for larger time, $t^* <= 7.78$, and the free surface remains smooth without any additional stabilization technique (see Fig. 3.9a and b). For the cubic NURBS model the wave reaches a maximum height of $6.85 \cdot 10^{-1}h$, which is very close to the reported in [1] ($6.89 \cdot 10^{-1}h$). For the quadratic NURBS model the height is slightly lower ($6.81 \cdot 10^{-1}h$) due to the lower degree of accuracy. In Fig. 3.10 we compare the central section of the cubic NURBS model and the results presented by Grilli et al. [1] at the breaking time. The relative errors for volume and energy are $\epsilon_v = 1.21 \cdot 10^{-4}$ and $\epsilon_e = 7.62 \cdot 10^{-5}$, respectively, and the shape is in very good agreement with the data reported in [1].

3.4.3 Wave in a cylindrical tank: Fluid-structure interaction

The objective of this section is to demonstrate the ability of the present formulation to reproduce fluid-structure phenomenon considering the effect of the waves propagating on the free surface of a tank. Here we test two different cases, one in which the body is stationary and another in which the body is in motion and generates the wave field.

In the first example we consider a cylindrical water tank with a solid cylindrical bar located at the center. The radius of the tank is $r_T = 10h$ and the radius of the bar is $r_B = 1h$ with h being the depth of the tank. Initially a wave is established in the middle point between the bar and the external wall of the tank. The elevation of the wave is given by the Gaussian pulse $z = Aexp[-(x - (r_B + r_T)/2)^2 - y^2]$ with

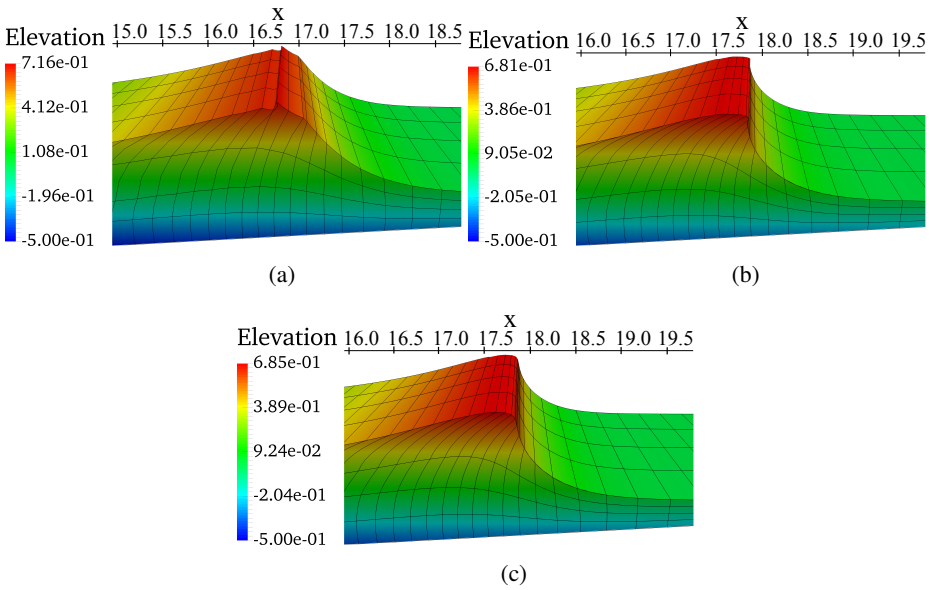

Figure 3.9: Wave shape for (a) the Lagrangian model at $t^* = 7.11$, when numerical instabilities appear, and for (b) the quadratic and c) cubic NURBS models at the breaking time (at $t^* = 7.78$.)

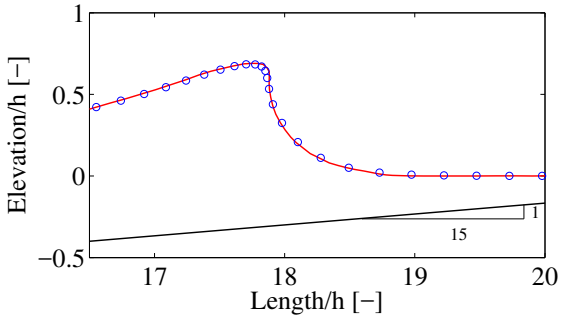

Figure 3.10: Wave shape of the central section (at $y = 1h$) for the present cubic NURBS model (circles) and for the results presented by Grilli et al. [1] using a 2D BEM model (continuous line) at the breaking time ($t^* = 7.78$).

$A = 0.1h$ being the amplitude of the wave. This problem has been solved by Chern et al. [2] using a Pseudo-Spectral Matrix Element Method and then used by Bai and Taylor [44] to validate their BEM formulation. More details about the problem can be found in [2, 44].

The geometry is discretized using three regular cubic NURBS surfaces that

represent the free surface, the bar and the external wall. Two symmetry planes are considered at $y = 0$ and $z = -h$. We set 26×25 Bézier elements (radial $\times$ circumferential) for the free surface, and 6×25 (vertical $\times$ circumferential) for the body and external wall. There are a total of 1316 control points.

A comparison of the surface elevation adjacent to the body ($[x = r_B, y = 0]$) and horizontal force as a function of the time between the present results and those reported by Chern et al. [2] is shown in Fig. 3.11. The simulation is run until $t^* = 30$ with a time step $\Delta t^* = 0.1$. As it can be seen, the present results are in good agreement with those in [2] where we have used less DoF than the required by [44] to obtain a close approximation (this is, 1316 vs 4208 DoF of the mesh b in Fig. 3a).

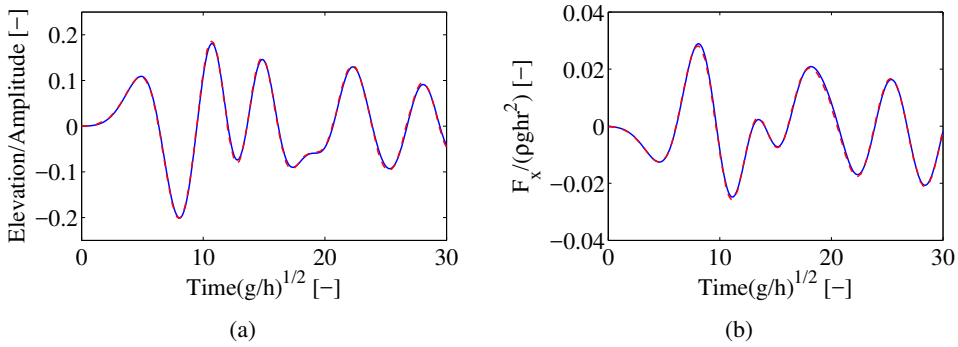

Figure 3.11: Time evolution of (a) surface elevation adjacent to the body ($[x = r_B, y = 0]$) and (b) horizontal force ($F_x/(\rho g h r^2)$). Present results: continuous line and results in [2]: dashed line.

We have also simulated the wave field radiated by a submerged sphere of radius r_B that moves vertically with an harmonic movement $z_B = z_0 + A\cos(\omega t)$ with $z_0 = -2r_B$ being the mean depth, A the amplitude and ω the frequency. This problem has been analysed by Ferrant [3] for a combination of several fundamental wave-numbers and two different amplitudes using a semi non-linear BEM. This example was also used by Hannan et al. [47] to validate a full non-linear BEM. For sake of brevity, we check the present formulation for a wave-number of $Kr_B = \omega^2 r_B/g = 2$ and two amplitudes of $A/r_B = 0.5$ and 0.7.

The problem is modelled by placing a sphere in a cylindrical water domain of radius $R = 9r_B$ and depth $h = 15r_B$. It is an axisymmetric problem and only a quarter of the model is considered. A structured axisymmetric mesh for the free surface would

have degenerate elements at the center, where the quadrilateral converge to triangular elements. In this case, the smoothness of the basis would be lost and numerical errors would appear reducing the accuracy. Alternatively, we use an unstructured T-spline surface with two levels of refinement as shown in Fig. 3.12. This mesh provides an adequate smoothness, regularity of the elements and accuracy around the center of the free surface where the sphere is located. The sphere is modelled using a cubic NURBS surface. It should be noted that the geometry is exact but there are degenerate elements around the poles. The accurate treatment of this specific case is detailed in [31]. The number of Bézier elements used for the free surface, sphere and external boundary are 350, 64 and 40, respectively and there are 640 control points with 1 extraordinary point.

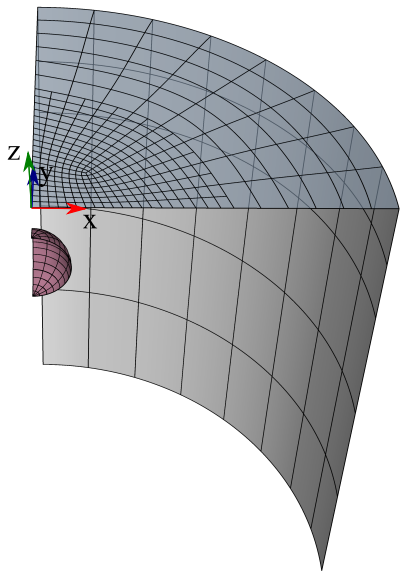

Figure 3.12: T-spline model of the cylindrical water domain with a submerged sphere.

In this example, the potential of the T-spline is shown. For that purpose, we study the vertical force on the sphere in the time domain. The time step used is $\Delta t = T/40$, with $T = 2\pi/\omega$ being the characterisic period. During the first two periods a cosine ramp function with shape $f_r = 0.5[1-\cos(\pi t/2T)]$ has been applied to the movement of the sphere to avoid an abrupt condition. Also, to minimize the wave reflections, a damping zone around the external boundary has been introduced.

First, we investigate the effect of the damping layer. Fig. 3.13 shows the wave

profiles along the radial direction produced by the amplitude $A/r_B = 0.7$ at the time $t = 7.5T$ for different parameters, this is, varying the damping length ($L_D = \lambda$ and 2λ) and the strength ($\alpha = \omega$ and $\omega/2$). For all the cases, reflective waves are not detected on the free surface. Moreover, the wave height decays along the radial direction due to the energy dispersion and the effect of the damping layer. This decay is more evident for higher values of α and the waves are absorbed at smaller radial positions for larger values of L_D.

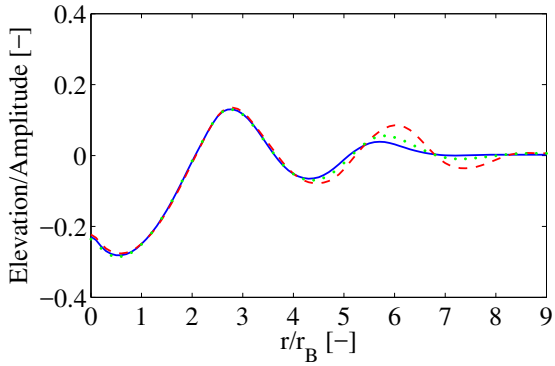

Figure 3.13: Wave profiles along radial direction for the amplitude $A/r_B = 0.7$ at the time $t = 7.5T$ considering three different absorbing layer paramenters: $\alpha = \omega$ and $L_D = 2\lambda$ (Continuous line), $\alpha = \omega$ and $L_D = \lambda$ (dashed line) and $\alpha = \omega/2$ and $L_D = 2\lambda$ (dotted line).

In Fig. 3.14 the vertical force on the sphere, considering the damping parameters $L_D = \lambda$ and $\alpha = \omega$, is shown . The results obtained by [47] are also included for comparison. It can be observed that both numerical results become coincident once the permanent state is reached, being the different transient behaviour due to the different ramp functions applied.

3.4.4 Wave-generator

In this section we show the application of the IGA-BEM to the simulation of the generation of artificial waves in a surf park. The model consists in a shallow water channel with a foil which is moved parallel to the free surface. The objective is to illustrate the ability of the method to analyse the wave field in the time domain and the forces on a complex profile.

The shape of the wave front depends on multiple parameters as the shape and the velocity of the foil, and the depth of the channel. In fact, the maximum height of

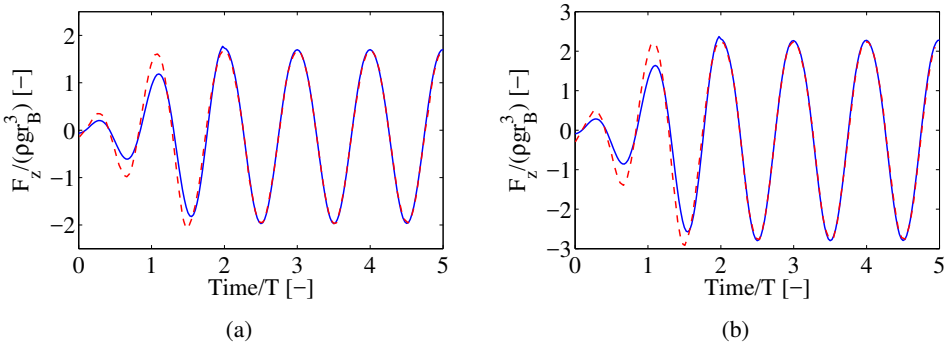

Figure 3.14: Time evolution of the vertical force (without considering hydrostatic pressure) on the sphere ($F_z/(\rho g r^3)$) for amplitudes (a) $A/R_B = 0.5$ and (b) $A/r_B = 0.7$. Present results: continuous line and reported in [3]: dashed line.

the wave front (H) can be roughly estimated with the relative thickness of the foil (h_B) as $H/h \approx h_B/h$. In addition, optimally the celerity and height of artificial waves generated should be close to those of the real waves (solitary wave). Here, we consider a rectangular cross-section channel with dimensions $[15 \times 6 \times 1]h$ (length, width and height) with h being the height. Two aerodynamic airfoils have been used, a symmetric NACA0015 and an asymmetric NACA6415 with a span of $4h$ and a chord of $3h$, in order to reduce the wave resistance. The foil is located $0.5h$ under the free surface and centered with respect to width of the channel. The estimated height of the wave front is about $0.45h$, then we set a maximum velocity (v_B) corresponding to a Froude number equal to $Fr = v_B/\sqrt{gh} = 1.2$.

In Fig. 3.15 we show the geometric discretization of the problem. The channel is modelled with three orthogonal cubic NURBS surfaces with regular elements, this is, 88×16 Bézier elements for the free surface, and 88×4 and 16×4 for the lateral walls (the other boundaries are considered implicitly in the Green function). Each foil consists in a smooth T-spline surface with 3144 elements. A local refinement is made around the trailing edge to capture with accuracy the large gradient of velocity in that location. There are a total of 5567 control points with 4 extraordinary points. It should be noted that the grid size for the free surface is finer than the used for the solitary wave. Moreover, the Courant Number is set to $\mathcal{C} = 0.4$ to obtain adequate accuracy and stability of the results.

The simulation starts from the rest and the foil is accelerated, with a sinusoidal ramp function $a_b/g = \sin(2t^*/Fr)$, until the maximum velocity is reached (at $t^* =$

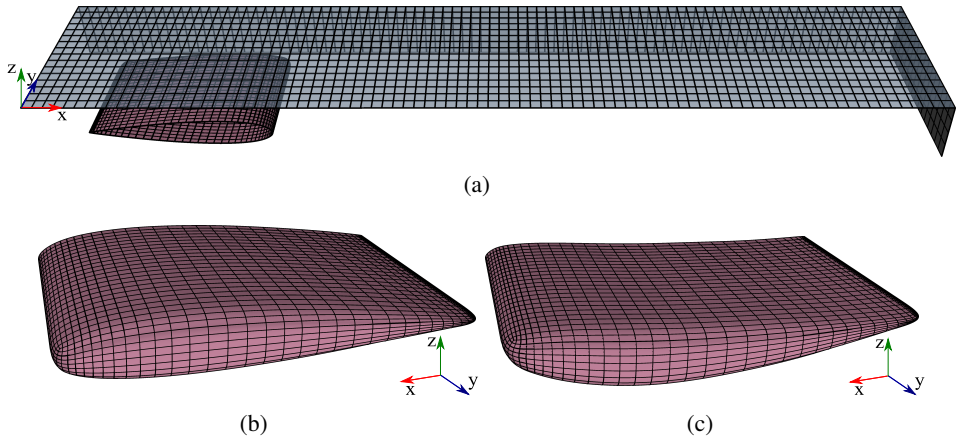

Figure 3.15: (a) Geometrical model of the full wavemaker and (b) and (c) details of the symmetric and asymmetric foils.

$Fr\pi/2$). This velocity is kept constant during the rest of the simulation. The free surfaces at $t^* = 7.56$ for both models are shown in Fig. 3.16. It can be seen that a wave front at a position slightly behind of the leading edge is formed. Moreover an overturning wave appears at the back of the symmetric foil. This is not observed for the asymmetric foil in which the wake is kept less perturbed and free of breaking. Precisely this last case is preferred in a surf park in order to generate periodically waves more regular and homogeneous. The transient process of the generation of the waves can be seen in Fig. 3.17, where three central vertical sections of the free surface are shown. The elevation of the wave front increases with time reaching a height of $4.41 \cdot 10^{-1}h$ for the symmetric and $4.25 \cdot 10^{-1}h$ for the asymmetric foil at $t^* = 7.56$, which are close to the estimated one of $H/h = 0.45$. At that time the calculated resistance coefficients are $C_D = F_x/(0.5\rho v_B^2 A_B) = 4.66 \cdot 10^{-2}$ and $5.07 \cdot 10^{-2}$ for the symmetric and asymmetric foil, respectively, with A_B being the plan area of foil (span $\times$ chord) and F the force. The lift coefficient is $C_L = F_z/(0.5\rho v_B^2 A_B) = 3.99 \cdot 10^{-1}$ for the symmetric foil and $2.29 \cdot 10^{-1}$ for the asymmetric foil. Note that these coefficients are calculated assuming the validity of the potential theory and the effects of viscosity, possible cavitation and vortex shedding are not taken into account. Although this approach, based on the potential theory, has been used extensively in wave-resistance problems [17, 18, 33, 114–116], these effects should be considered for a more accurate calculation [117, 118].

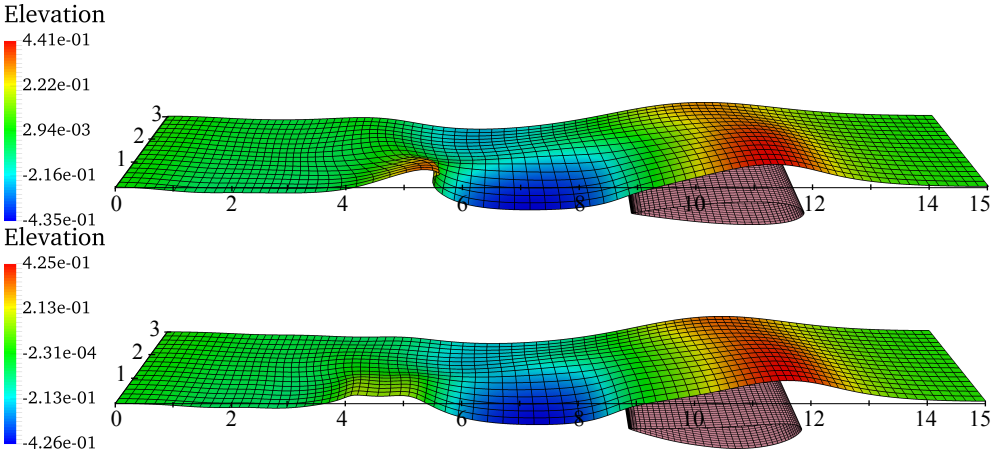

Figure 3.16: Free surface elevation (H/h) calculated at $t^* = 7.56$ for (a) the symmetric foil and (b) asymmetric foil.

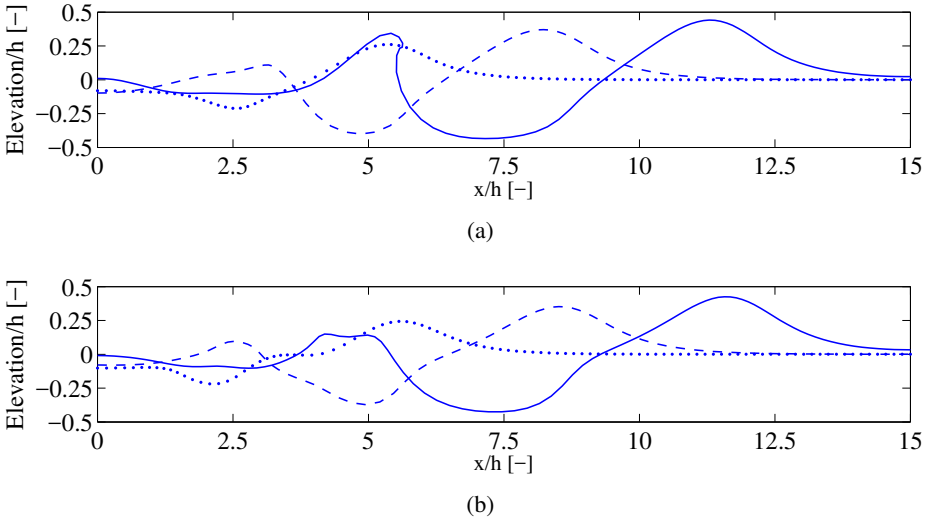

Figure 3.17: Central vertical section ($y = 0$) of the free surface (a) for the symmetric foil at $t^* = 2.52$ (dotted line), 5.00 (dashed line) and 7.56 (continuous line), and b) for the asymmeric foil at $t^* = 2.49$ (dotted line), 5.01 (dashed line) and 7.56 (continuous line)

3.5 Conclusions

In this chapter a 3D IGA-BEM formulation using T-spline and NURBS basis to study fully non-linear gravity wave propagation in the time domain has been presented. The use of splines basis provides a high geometrical approximation and it can be

directly integrated with computer aided geometrical design tools. The properties of these basis within the BEM have been analysed using numerical examples. First, an optimal spatial convergence of the method has been demonstrated in the simulation of a periodic train of waves. Following, the temporal stability and accuracy have been analysed simulating the propagation of a solitary gravity wave. The numerical errors are kept practically constant to a low order over a wide range of time steps demonstrating the robustness of the time marching scheme. Moreover, the smoothness of the basis functions provides stability to the method without the need of artificial smooth techniques, and it allows relatively large distortion of elements. In addition, the ability of the method to simulate the fluid-structure interaction with fixed or moving bodies has been shown with simulations of the waves generated in a tank. An unstructured mesh with some local levels of refinement has been used to show the potential and the efficiency of the T-spline in the simulation of the waves generated by a submerged sphere in a tank. Finally, the application of the method to simulate the wave field generated by submerged foils has been used to show the ability of the method to analyse complex models.

UNIVERSITAT ROVIRA I VIRGILI
TOWARDS THE APPLICATION OF THE ISOGEOMETRIC BOUNDARY ELEMENT ANALYSIS TO FLUID MECHANICS:
NON-LINEAR GRAVITY WAVES AND DYNAMICS OF DEFORMABLE CAPSULES IN SHEAR FLOWS
Jorge Maestre Heredia

Chapter 4

Dynamics of deformable capsules

4.1 Introduction

In the last decades, the hydrodynamic movement of suspended capsules in a flowing fluid has captured the attention of many research due to their multiple implications in industrial and biological applications. In the biomedical area, the study of the dynamic behaviour of deformable vesicles and Red Blood Cells (RBC) helps to a better understanding of some phenomenon as the thrombosis, the thalassemia or other microcirculatory diseases [119]. As pharmacologic treatments, artificial capsules are being used as an effective technique to deliver some substances or drugs through the biological system and in a sustained way. Nowadays, the micro-capsules are being applied to a wide range of areas as cosmetics, agriculture or food industry [120]. The characterization and the study of these deformable capsules can be important aspects for the suitable design and optimization of different processes connected with the capsule dynamics. Regarding this issue, experiments are indispensable but because of the small length scale, they are difficult and costly. Thanks to the rapid increase of the computational capacity, the numerical models have opened new perspectives and they offer a powerful tool to analyse the capsule deformation.

The capsules consist on a viscous internal fluid enclosed and protected by a flexible membrane. The interaction between the capsules and the external flowing fluid is a complex process. Analytical solutions have been proposed for deformable capsules in a simple shear flow [121, 122], nevertheless the application is limited to small

deformations. The capsule usually experiences large deformations changing the shape and modifying the whole behaviour of the flowing fluid. In these cases the only option is the use of numerical models. Different models have been successfully used to solve the fluid-structure interaction. Many of these models are based on CFD solvers [123, 124], FEM [125, 126], FDM [127], Immersed Boundary Methods (IBM) [128–131] and LBM [132–134]. These approaches have the advantage that are applicable to a wide range of problems (for different geometries, Reynolds numbers and fluid properties), the formulation is well mature and even there are some available in commercial software. However the whole fluid domain has to be discretized and it involves a large number of elements, a difficult management of the mesh and a high computational cost. In many microfluidics applications the Reynolds number is very low and the inertial effects are negligible. Assuming Newtonian or nearly-Newtonian fluid, the flow is governed by the Stokes equation. In such cases, the BEM is as a favourable alternative for different reasons as it has been introduced in previous chapter.

Several models for deformable capsules using the BEM have been reported in the literature. Pozrikidis [35] studied the transient large deformation of a three-dimensional spherical isoviscous capsule in a shear using a global geometric representation of the membrane based on quadrilateral elements. Ramanujan and Pozrikidis [36] extended the formulation for an unstructured mesh built with quadratic triangular elements and investigated the large deformation of various capsule shapes considering the effect of different fluid viscosities. Leyrat-Maurin and Barthès-Biesel [135] and Quéguiner and Barthès-Biesel [136] developed an axisymmetric BEM for the analysis of deformable capsules through pores, tubes and constrictions. Diaz et al. [137], Diaz and Barthè-Biesel [138] and Lefebvre and Barthès-Biesel [6] improved the previous formulation using cubic B-splines functions and they analysed the influence of various parameter in the deformation of the capsules (such as membrane properties and shapes, and fluid viscosity, or membrane pre-stress). Lac et al. [4] and Lac and Barthès-Biesel [139] presented a three dimensional formulation based on a bicubic B-spline basis functions for deformable capsules in a planar shear and an hiperbolic flow. This method offers a high order of approximation and continuity of the physical variables providing accurate results. Deformable capsules in moderate and high shear flow were also tackled by Dodson and Dimitrakopoulos [140, 141] who developed a spectral BEM. More recently, via accelerated BEM Zhu et al. [142] studied the motion of a capsule in a wall-bounded oscillating shear flow and Touchard et al. [143]

studied the deformation of a capsule flowing through a micro-channel with a localized constrain.

Following the pioneer works of Zarda et al. [144] and Skalat et al. [145, 146], the majority studios consider the membrane to be a thin hyper-elastic shell with neglected bending resistance. This model is applicable to a wide range of artificial capsules and biological cells and it is in agreement with experimental findings that reveal the relatively low bending resistance of the membrane [147–149]. It is worth to mention that other more detailed models have been developed and take into account the bending resistance, the surface incompressibility, membrane viscosity and rheology (see for example [150–154]), although they are computationally intensive. A complete review of the mechanical properties of deformable capsules can be found in [155].

The accuracy of the BEM depends on the computation of the hydrodynamic load over the membrane. Using the local equilibrium equation, a high order differentiation of the geometry is required. In the traditional BEM the basis are C^0 piecewise continuous, thus the spatial derivatives between elements are discontinuous. Pozrikisdis [35] and Ramanujan and Pozrikidis [36] found some instabilities associated with the lack of continuity on the bases. They applied a smoothing scheme to relocate the nodes and an ad-hoc average technique of the membrane stress to alleviate these numerical instabilities. A smooth technique was also employed by Dodson and Dimitrakopoulos [141] to force the continuity of the first derivatives between spectral elements. Lac et al. [4] reported some instabilities near the poles despite of the high order continuity of the B-spline functions. Regarding this issue, Walter et al. [5] formulated a coupled BEM-FEM model for deformable capsules. The loads are computed via variational principle and this reduces the continuity requirements of the basis functions and it produce more stables results. This formulation has been recently used to study the dynamics of deformable capsules [156–160].

In this chapter a formulation of the IGA based on the analysis suitable T-spline is presented for the study the dynamics of deformable capsules in suspended flows. The BEM is used to solve the fluid dynamics that is coupled with FEM to compute the membrane load. The membrane is considered to be a thin elastic shell, thus the discretization of the interface is shared for both methods. The smoothness of the bases makes the method to be stable for large deformations of the capsule. In addition, invoking the local refinability of the T-spline, the mesh can be suitable managed during

the simulation to dynamically adapt it to the specific need of the problem. These properties give the analysis suitable T-spline-based IGA the potential to be an efficient, accurate and robust tool for the analysis of deformable capsules as well as it is versatile due to the tight link with the CAD technologies.

4.2 Formulation of the problem

4.2.1 Hydrodynamic

We consider a capsule defined by the boundary Γ_C and confined in a tube $\Gamma_T = \Gamma_I \cup \Gamma_W \cup \Gamma_O$. The tube is filled with an external fluid Ω_1. The capsule is formed by a thin deformable membrane that contains an internal fluid Ω_2. The capsule moves freely by the action of the external flow in the tube, while the internal fluid is moved due to the deformation of the membrane. Both fluids are assumed to be incompressible and Newtonian, with the same density ρ and different viscosities, $\mu_1 = \mu$ and $\mu_2 = \kappa\mu$, being κ the viscosity ratio. A sketch of the problem is shown in Fig. 4.1.

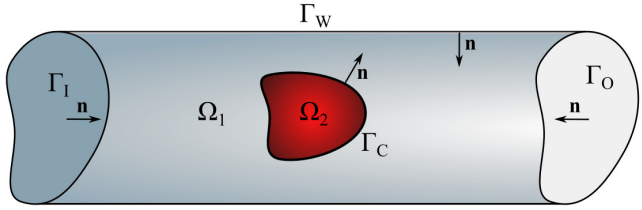

Figure 4.1: Sketch of the problem

In microcirculation problems the Reynolds number is considerably small, $Re << 1$, and the viscous effects are assumed to be dominant compared with the inertial effects. In these cases, the internal and external fluids can be described by the Stokes flow,

$$\begin{cases} \nabla \cdot \mathbf{v}_i = 0 \\ \nabla \cdot \boldsymbol{\sigma}_i = -\nabla p_i + \mu_i \nabla^2 \mathbf{v}_i = 0 \end{cases} \quad \text{in } \Omega_i \text{ and } i = 1, 2 \tag{4.1}$$

where $\boldsymbol{\sigma}_i$ is the fluid stress tensor given in terms of the velocity $\mathbf{v}_i$ and pressure p_i in the fluid domain Ω_i.

In this work we consider non slip conditions. This ensures the continuity of the velocity across the membrane. Whereas the stress on both sides of the membrane is

allowed to be discontinuous. The difference on the membrane, known as stress jump $\Delta\mathbf{f} = (\boldsymbol{\sigma}_1 - \boldsymbol{\sigma}_2)\mathbf{n}$, with $\mathbf{n}$ being the unit normal vector pointing outwards of the capsule, depends on the mechanical properties of membrane as it is discussed in the next section.

4.2.2 Mechanical properties of the membrane

The dynamical and mechanical behaviours of capsules are governed by the micro-mechanical properties of the membrane and the properties of the external and internal fluids. The biological membranes are complex systems that can experiment large deformations changing the shape and the mechanical characteristics of the capsule. Various models at different scales and levels of detail have been proposed depending on the type of biological capsule and the application [153, 161–168]. In this study we employ a general continuous elastic model. As proposed by several authors, we consider that the membrane is extremely thin and the strain and stress are constant across the membrane. Therefore, the membrane is assumed to be a bi-dimensional elastic sheet and the bending resistance is neglected.

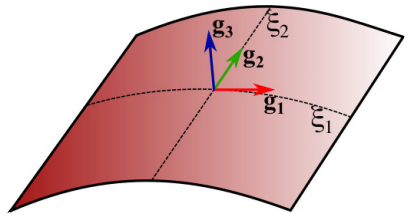

Figure 4.2: Curvilinear system

Let us describe the membrane by a curvilinear system defined by two parametric coordinates $\boldsymbol{\xi} = (\xi^1, \xi^2)$ (see Fig. 4.2). Thus, the reference position $(t = 0)$ of any point of the membrane is given by $\mathbf{X}(\boldsymbol{\xi})$. Assuming that the membrane moves, any material point at the current state is represented by $\mathbf{x}(\boldsymbol{\xi}, t)$. The uppercase and lowercase letters correspond to the reference and the current state, respectively.

The local covariant bases are constructed as follows:

$$\mathbf{g}_1 = \mathbf{x}_{,1}, \quad \mathbf{g}_1 = \mathbf{x}_{,2}, \quad \mathbf{g}_3 = \mathbf{n} = \frac{\mathbf{g}_1 \times \mathbf{g}_2}{|\mathbf{g}_1 \times \mathbf{g}_2|} \tag{4.2}$$

where the sub-index $\cdot_{,\alpha} = \frac{\partial \cdot}{\partial \xi^\alpha}$ denotes the partial derivative with respect to the parametric coordinates.

The local contravariant bases $(\mathbf{g}^1, \mathbf{g}^2, \mathbf{g}^3)$ are defined such that $\mathbf{g}^\alpha \cdot \mathbf{g}_\beta = \delta^\alpha_\beta$, where δ^α_β is the mixed Kronecker delta, and $\mathbf{g}^3 = \mathbf{n}$. The metric tensors associated to each basis are $g_{ij} = \mathbf{g}_i \cdot \mathbf{g}_j$ and $g^{ij} = \mathbf{g}^i \cdot \mathbf{g}^j$. Unless otherwise specified, the Greek indices α and β go from 1 to 2, and Latin indices i and j go from 1 to 3. On the other hand, the local covariant, contravariant and metric tensor at the reference state are analogously defined and represented by uppercase letters.

The local equilibrium equation of the membrane at the current state is given by

$$\nabla_s \cdot \boldsymbol{\tau} + \mathbf{t} = 0 \tag{4.3}$$

In Eq. 4.3 we assume that the inertia of the membrane is negligible, which is reasonable in the case of thin membranes. The first term, $\boldsymbol{\tau}$, is the in-plane Cauchy stress tensor that corresponds to the force per unit arc length of the membrane, ∇_s is the surface divergence and the second term ,$\mathbf{t} = \Delta\mathbf{f}$, is the traction on the membrane that is equal to the jump stress.

In this work, we consider that the membrane is a hyper-elastic isotropic material. This material is a subclass of the elastic material in which the constitutive equation can be described in terms of a scalar strain energy function $\Psi(\boldsymbol{F})$:

$$\boldsymbol{\tau} = \frac{\partial \Psi(\boldsymbol{F})}{\partial \boldsymbol{F}} \frac{\boldsymbol{F}^T}{J_s} \tag{4.4}$$

In Eq. 4.4 the tensor $\boldsymbol{F} = d\mathbf{x}/d\mathbf{X} = \mathbf{g}_i \otimes \mathbf{G}^i$ is the deformation gradient and $J_s = |\boldsymbol{F}|$ is the surface dilatation. In the case of isotropic bi-dimensional models the tensor gradient and the energy function only depend on two strain invariants:

$$I_1 = G^{\alpha\beta} g_{\alpha\beta}, \quad I_2 = |G^{\alpha\beta}||g_{\alpha\beta}| - 1 = J_s^2 - 1 \tag{4.5}$$

and the Cauchy tensor in the contravariant form can be written as,

$$\tau^{\alpha\beta} = 2J_s^{-1} \frac{\partial \Psi(I_1, I_2)}{\partial I_1} G^{\alpha\beta} + 2J_s \frac{\partial \Psi(I_1, I_2)}{\partial I_2} g^{\alpha\beta} \tag{4.6}$$

In the literature, several constitutive laws have been proposed to take into account the mechanical properties of biological membranes [169]. In this work, two common models are adopted: the Neo-Hookean model and the model for red blood cells (RBC) proposed by Skalat et al. [145]. The bi-dimensional Neo-Hookean model is usually

used to describe behaviour of proteinreticulated membranes. The energy function is given by:

$$\Psi^{NH} = \frac{G_s^{NH}}{2}\left(I_1 + \frac{1}{I_2+1} - 1\right) \tag{4.7}$$

where G_s^{NH} is the shear modulus. The area dilatation coefficient is defined as $K_s^{NH} = 3G_s^{NH}$.

Although, the model reported by Skalat et al. was originally developed for RBCs, it also is appropriated and extensible for other biological cells. The energy function is defined as:

$$\Psi^{Sk} = \frac{G_s^{Sk}}{4}\left(I_1^2 + 2I_1 - 2I_2 + \mathsf{C}I_2^2\right) \tag{4.8}$$

In Eq. 4.8 G_s^{Sk} is the shear modulus and $\mathsf{C} > -1/2$ is a parameter that indicates the ratio between the area dilatation and the shear modulus such that $K_s^{Sk} = G_s^{Sk}(1+2\mathsf{C})$. In contrast to the softening Neo-Hookean model, the Skalat law shows a strain-hardening behaviour and for $\mathsf{C} >> 1$ the model is almost area-incompressible, as observed in RBCs.

4.3 Formulation of the method

4.3.1 Isogeometric Boundary Element Method

The application of the boundary integral formulation to Stokes flows is mature and well known [170]. In this section we expose this formulation focusing on those aspects related to the isogeometric paradigm and our algorithm. In this context, the field velocity and the fluid stress are discretizated in a finite space $\mathcal{V}^h$ defined by the same set of basis functions as the geometry. Thus, using the global notation, both vectorial field can be expressed as,

$$\begin{aligned}\mathbf{v}(\mathbf{x}) &= \sum_{A=1}^{m_{cp}} R_A(\mathbf{x})\mathbf{v}_A \\ \mathbf{f}(\mathbf{x}) &= \sum_{A=1}^{m_{cp}} R_A(\mathbf{x})\mathbf{f}_A\end{aligned} \tag{4.9}$$

where $\{\mathbf{v}_A\}_{A=1}^{m_{cp}}$ and $\{\mathbf{f}_A\}_{A=1}^{m_{cp}}$ are the velocity and fluid stress control vector corresponding to the global basis $\{R\}_{A=1}^{m_{cp}}$.

Given a continuous surface Γ, the single-layer and double-layer potential operators applied to the collocation point $\mathbf{x}_0$ are defined as,

$$(\boldsymbol{\mathcal{G}}_\Gamma \mathbf{f})(\mathbf{x}_0) = \frac{1}{8\pi\mu}\int_\Gamma \mathfrak{G}_{ij}(\mathbf{x},\mathbf{x}_0) f_j(\mathbf{x}) d\Gamma \quad \text{and} \quad (\boldsymbol{\mathcal{H}}_\Gamma \mathbf{v})(\mathbf{x}_0) = \frac{1}{8\pi}\fint_\Gamma \mathfrak{T}_{ij}(\mathbf{x},\mathbf{x}_0) v_j(\mathbf{x}) d\Gamma \tag{4.10}$$

respectively. In discrete form these operators can be written as,

$$\begin{aligned}(\boldsymbol{\mathcal{G}}_\Gamma \mathbf{f})^h(\mathbf{x}_0) &= \frac{1}{8\pi\mu}\sum_{A=1}^{m_{cp}}\int_\Gamma \mathfrak{G}(\mathbf{x},\mathbf{x}_0) R(\mathbf{x})_A \mathbf{f}_A d\Gamma \\ (\boldsymbol{\mathcal{H}}_\Gamma \mathbf{v})^h(\mathbf{x}_0) &= \frac{1}{8\pi}\sum_{A=1}^{m_{cp}}\fint_\Gamma \mathfrak{T}(\mathbf{x},\mathbf{x}_0) R_A(\mathbf{x}) \mathbf{v}_A d\Gamma\end{aligned} \tag{4.11}$$

Although both integrals are well defined, we indicate with the symbol $\fint$ that the double-layer integral is evaluated in the Cauchy Principal Value sense (CPV) when the collocation point lies on the integration domain Γ. The tensors $\mathfrak{G}(\mathbf{x},\mathbf{x}_0)$ and $\mathfrak{T}(\mathbf{x},\mathbf{x}_0)$ are the free-space Green's functions of the Stokes flow. For a three dimensional space these tensors are given by:

$$\begin{aligned}\mathfrak{G}_{ij}(\mathbf{x},\mathbf{x}_0) &= \frac{r_i r_j}{|\mathbf{r}|^3} + \frac{\delta_{ij}}{|\mathbf{r}|} \\ \mathfrak{T}_{ij}(\mathbf{x},\mathbf{x}_0) &= -6\frac{r_i r_j r_k n_k}{|\mathbf{r}|^5}\end{aligned} \qquad i,j \text{ and } k = 1,2,3 \tag{4.12}$$

where δ_{ij} is the Kronecker's delta and $\mathbf{r} = \mathbf{x} - \mathbf{x}_0$.

As usual, we consider the Stokes problem as a superposition of two flows, this is, the total fluid velocity and fluid traction vectors can be expressed as $\mathbf{v} = \mathbf{v}^\infty + \mathbf{v}^D$ and $\mathbf{f} = \mathbf{f}^\infty + \mathbf{f}^D$, respectively. The unperturbed flow, denoted with the super-index $\cdot^\infty$, corresponds to known pipe flow without the capsule (see Fig. 4.1). Whereas the disturbed flow (super-index $\cdot^D$) is caused only by the presence of the capsule. The boundary integral equation (BIE) applied to the capsule can be expressed as,

$$\begin{aligned}\left[\mathbf{I} - (1-\kappa)\boldsymbol{\mathfrak{C}}(\mathbf{x}_0)\right]\mathbf{v}(\mathbf{x}_0) = (1-\kappa)(\boldsymbol{\mathcal{H}}_{\Gamma_C}\mathbf{v})(\mathbf{x}_0) - (\boldsymbol{\mathcal{G}}_{\Gamma_C}\Delta\mathbf{f})(\mathbf{x}_0) \\ - (\boldsymbol{\mathcal{G}}_{\Gamma_T}\mathbf{f}^D)(\mathbf{x}_0) + \mathbf{v}^\infty(\mathbf{x}_0) \qquad \mathbf{x}_0 \in \Gamma_C\end{aligned} \tag{4.13}$$

and in the tube,

$$\mathbf{0} = (1-\kappa)(\boldsymbol{\mathcal{H}}_{\Gamma_C}\mathbf{v})(\mathbf{x}_0) - (\boldsymbol{\mathcal{G}}_{\Gamma_C}\Delta\mathbf{f})(\mathbf{x}_0) - (\boldsymbol{\mathcal{G}}_{\Gamma_T}\mathbf{f}^D)(\mathbf{x}_0) \quad \mathbf{x}_0 \in \Gamma_T \tag{4.14}$$

where $\mathbf{I} \in \Re^{3\times3}$ is the identity matrix and the term $\mathfrak{C}(\mathbf{x}_0) \in \Re^{3\times3}$ is the solid angle, that can be computed directly using the formulation proposed by Mantic [93] or indirectly appealing to the "rigid body motion" method [94]. We employ this last technique since it provides a regularization of the second-layer integral avoiding the computation of the integral in the CPV sense. Thus, the second-layer potential term on the capsule is modified as,

$$(\widehat{\boldsymbol{\mathcal{H}}}_{\Gamma_C}\mathbf{v})(\mathbf{x}_0) = \mathfrak{C}(\mathbf{x}_0)\mathbf{v}(\mathbf{x}_0) + (\boldsymbol{\mathcal{H}}_{\Gamma_C}\mathbf{v})(\mathbf{x}_0) = \frac{1}{8\pi}\int_{\Gamma_C}\mathfrak{T}(\mathbf{x},\mathbf{x}_0)(\mathbf{v}(\mathbf{x})-\mathbf{v}(\mathbf{x}_0))d\Gamma \tag{4.15}$$

which in discrete form can be written as,

$$(\widehat{\boldsymbol{\mathcal{H}}}_{\Gamma_C}\mathbf{v})^h(\mathbf{x}_0) = \frac{1}{8\pi}\sum_{A=1}^{m_{cp}}\int_{\Gamma}\mathfrak{T}(\mathbf{x},\mathbf{x}_0)\left(R_A(\mathbf{x})-R_A(\mathbf{x}_0)\right)\mathbf{v}_A d\Gamma \quad \mathbf{x}_0 \in \Gamma_C \tag{4.16}$$

In Eqs. (4.13) and (4.14) we assume the inlet Γ_I and outlet Γ_O boundaries (see Fig. 4.1) are sufficiently far from the capsule such that the perturbed velocity flow is practically negligible. The disturbed fluid stress on the inlet and outlet can be retained as unknown variables in the BIE or explicitly computed by an auxiliary equation as proposed by Pozrikidis[164]. This last alternative reduces the number of degrees of freedom (DoF) of the BIE and it is used in this work. Approximating the disturbed fluid stress at the inlet as $\mathbf{f}^D_{\Gamma_I} \simeq -\Delta P^D\mathbf{n}$ and setting $\mathbf{f}^D_{\Gamma_O} = \mathbf{0}$ at the outlet, the disturbed pressure drop ΔP^D can be calculated as:

$$\Delta P^D = \frac{1}{Q^\infty}\int_{\Gamma_C}\Delta\mathbf{f}(\mathbf{x})\cdot\mathbf{v}^\infty(\mathbf{x}) + (1-\kappa)\mathbf{f}^\infty(\mathbf{x})\cdot\mathbf{v}(\mathbf{x})d\Gamma \tag{4.17}$$

in which $Q^\infty \simeq Q$ is the total instantaneous flow rate.

We use generalized Greville abcisae as the collocation points of the BIE [24]. This strategy manages robustly extraordinary points and hanging-nodes and it has been shown that provides suitable results in the context of isogeometric analysis. Thus, the BIE (Eq. 4.13 and Eq. 4.14) must be satisfied in a set of m_{cp} specific points $\{\mathbf{x}_\alpha\}_{\alpha=1}^{m_{cp}}$. The particularization of the discrete BIE to those points generates a system

of equations that can be written in matrix form as,

$$\begin{bmatrix} (1-\kappa)\widehat{\mathbf{H}}_{CC} - \mathbf{R}^T(\mathbf{x}_C) & \mathbf{0} \\ (1-\kappa)\mathbf{H}_{WC} & \mathbf{0} \end{bmatrix} \begin{bmatrix} \mathbf{v}_C \\ \mathbf{0} \end{bmatrix} = \begin{bmatrix} \mathbf{G}_{CC} & \mathbf{G}_{CW} \\ \mathbf{G}_{WC} & \mathbf{G}_{WW} \end{bmatrix} \begin{bmatrix} \overline{\Delta \mathbf{f}} \\ \mathbf{f}_W^D \end{bmatrix} - \Delta p^D \begin{bmatrix} \mathbf{G}\mathbf{n}_C \\ \mathbf{G}\mathbf{n}_W \end{bmatrix} - \begin{bmatrix} \mathbf{v}^\infty(\mathbf{x}_C) \\ \mathbf{v}^\infty(\mathbf{x}_W) \end{bmatrix} \tag{4.18}$$

In Eq. 4.18 $\mathbf{H}$ and $\mathbf{G}$ denote the single-layer and double-layer global matrices where the first sub-index makes reference to the localization of the collocation points (on the capsule or on the tube wall) and the second one is referred to the integration domain. $\mathbf{Gn}$ is a global vector that corresponds to the single-layer operator applied on the inlet cap assuming the approximation of constant fluid stress vector in the normal direction. $\mathbf{R}$ is the global rational basis functions in matrix form evaluated at the collocation points $\mathbf{x}_C$. $\mathbf{v}^\infty$ is the unperturbed velocity vector evaluated at the collocation points. Note that the jump stress vector on the capsule $\Delta\mathbf{f}$ is known at any time by applying the membrane equilibrium equation (Eq. 4.3). The computation of the membrane stress will be explained in more detail in the next section. Whereas, the velocity vector of the capsule $\mathbf{v}_C$, the disturbed fluid stress vector of the tube wall $\mathbf{f}_W^D$ and disturbed pressure drop Δp^D are unknown variables. The problem is completely defined adding the pressure drop equation (Eq. 4.17).

Following the standard FE formulation, the global matrix and vectors can be constructed by parts performing an integration over each Bézier element and then assembling in the global system [57]. The single-layer and regularized double-layer potential operator are weakly singular. As proposed by Lachat and Watson [95], this singularity is addressed by making a local change of variable in the element that contains the collocation point. The numerical evaluation of the integrals is performed by a Gauss-Legendre quadrature with eight quadrature-points on each element in the parent domain.

4.3.2 Isogeometric Finite Element Method

Known the unstressed state of the membrane and for a given current configuration at any time, the internal stress and tractions on the membrane can be computed making use of the local equilibrium equation (Eq. 4.3) in the strong form. Regarding the BIE, the stress jump on the membrane can be directly introduced evaluating the tractions at

a series of specific points as the quadrature-points are. This method requires to rely on the differentiability of the stress in the membrane as well as on the differentiability of the geometry since it is necessary to compute the divergence of the stress tensor and the curvilinear system is used. Even using cubic T-splines that offer a high order of approximation and smoothness, there are local regions of the membrane (as those around poles or extraordinary points) where the continuity is reduced. In the proximity of such regions, the evaluation of high order derivatives can introduce errors leading to numerical problems. In the literature, numerical instabilities associated to that issue have been reported when B-spline discretizations have been employed [4], that establishes the need to develop some additional techniques to alleviate such problems. As proposed by Walter et al. [5], in this work we use a weak formulation of the membrane mechanics. This technique relaxes the continuity requirement of the basis functions allowing the first derivatives to be discontinuous between elements C^0. It gives accurate and stable results without the need to implement smoothing techniques. Following we expose this formulation in the context of isoperimetrical analysis.

In virtue of the principle of virtual works (PVW) in the spatial description, the balance equation on the membrane can expressed in a variational form as,

$$\underbrace{\int_{\Gamma_C} \delta\mathbf{u}(\mathbf{x}) \cdot \mathbf{t}(\mathbf{x}) d\Gamma}_{\delta W^{ext}} = \underbrace{\int_{\Gamma_C} \delta\boldsymbol{e}(\mathbf{x}) : \boldsymbol{\tau}(\mathbf{x}) d\Gamma}_{\delta W^{int}} \tag{4.19}$$

The left and right side terms of Eq. 4.19 represent the work by the external force and internal stress, respectively. $\delta\mathbf{u}(\mathbf{x})$ is the virtual displacement vector and $\delta\mathbf{e}(\mathbf{x})$ is the virtual Euler-Almansi strain tensor. The displacement vector is defined as the difference between the current and reference state $\mathbf{u}(\mathbf{x}) = \mathbf{x}(t) - \mathbf{X}$ and the virtual displacement is assumed to be an arbitrary and infinitesimal variation of the displacements. The virtual Euler-Almansi strain tensor compatible with the virtual displacements is given by,

$$\delta\boldsymbol{e}(\mathbf{x}) = \frac{1}{2}\left(\nabla_s \delta\mathbf{u}(\mathbf{x}) + \nabla_s^T \delta\mathbf{u}(\mathbf{x})\right) \tag{4.20}$$

Using a curvilinear coordinate system it can be rewritten in covariant form as,

$$\delta e_{\alpha\beta}(\mathbf{x}) = \frac{1}{2}\left(\delta u_{\alpha,\beta}(\mathbf{x}) + \delta u_{\beta,\alpha}(\mathbf{x}) - 2\Gamma^i_{\alpha\beta}(\mathbf{x})\delta u_i(\mathbf{x})\right) \tag{4.21}$$

where $\Gamma^i_{\alpha\beta} = \mathbf{g}^i \cdot \mathbf{g}_{\alpha,\beta}$ is the Cristoffel symbol and $b_{\alpha\beta} = \Gamma^3_{\alpha\beta}$ is known as the curvature

tensor.

Under the isoparametric concept, the virtual displacement and traction on the membrane are discretized in a finite space defined by the T-spline basis functions $\mathcal{V}^h$. These are written as,

$$\begin{aligned} \delta\mathbf{u}(\mathbf{x}) &= \sum_{A=1}^{m_C} R(\mathbf{x})_A \delta\mathbf{u}_A \\ \mathbf{t}(\mathbf{x}) &= \sum_{A=1}^{m_C} R(\mathbf{x})_A \mathbf{t}_A \end{aligned} \tag{4.22}$$

where m_C is the number of global basis function in the capsule and $\{\delta\mathbf{u}_A\}_{A=1}^{m_C}$ and $\{\mathbf{t}_A\}_{A=1}^{m_C}$ are the virtual displacement and traction control vector corresponding to the global basis $\{R\}_{A=1}^{m_C}$.

Introducing Eq. 4.22 in the PVW (Eq. 4.19), we obtain the equation in the discrete form. After some operations the left and right hand side terms of Eq. 4.19 can be expressed as,

$$\delta W^{ext} = \sum_{A=1}^{m_C}\sum_{B=1}^{m_C} \left[\delta\mathbf{u}_A^T \mathbf{t}_B \int_\Gamma R_A(\mathbf{x}) R_B(\mathbf{x})\right] d\Gamma \tag{4.23}$$

$$\begin{aligned} \delta W^{int} = \sum_{A=1}^{m_C} \Bigg[\delta\mathbf{u}_A^T \int_\Gamma \tau^{\alpha\beta}(\mathbf{x}) \Bigg(&\frac{1}{2} R_{A,\beta}(\mathbf{x})\mathbf{g}_\alpha + \frac{1}{2} R_{A,\alpha}(\mathbf{x})\mathbf{g}_\beta \\ &+ R_A(\mathbf{x})\mathbf{g}_{\alpha,\beta} - \Gamma^i_{\alpha\beta} R_A(\mathbf{x})\Bigg) d\Gamma\Bigg] \end{aligned} \tag{4.24}$$

Note that for a given current state the Cauchy tensor $\boldsymbol{\tau}(\mathbf{x})$ can be evaluated directly using the constitutive equation (Eq. 4.6). In matrix form the PVW can be written as,

$$\mathbf{M}\mathbf{t} = \mathbf{d} \tag{4.25}$$

where $\mathbf{M} \in \Re^{3m_C \times 3m_C}$ is the global matrix of the system, $\mathbf{t} \in \Re^{3m_C}$ is the global traction vector on the membrane and $\mathbf{d} \in \Re^{3m_C}$ is the known right hand side term of Eq. 4.24. As in the preceding boundary integral formulation, the global system can be constructed by parts using an integration over each Bézier element. The numerical evaluation of the integrals are computed by a Gauss-Legendre quadrature with eight quadrature points.

4.3.3 Dynamic refinement

In dynamic problems with large deformation, the accuracy of results is very sensitive to numerical errors in each time step, thus the discretization plays a very important role. As the capsule is moved and deformed as the time evolves, the geometry and the other physical variables change. In some cases the discretization can not be appropriated in regions with relatively high gradients of the variables at a certain time. To address this issue, we exploit the T-spline properties and apply a dynamic analysis-suitable local h-refinement (element-subdivision) to the capsule. It should be note that, alike the traditional FE Analysis, the T-spline refinement process does not necessarily change the physical space, this is, the original physical space is nested in the new physical space. This feature is very atractive and it represents an accurate tool. The details of the Tspline h-refinement can be found in [21, 56].

The aim of the dynamic refinement is to construct a reasonable discretization of the capsule during the all simulation. For this, the quality of the T-spline mesh is evaluated as a function of the discretized variables and it is modified if required. Thus, a set of parameters is defined to measure the suitability of the T-spline mesh. In this work, we select the size and the variation of the tractions, the velocity and the mean curvature ($\chi = 1/2\nabla \cdot \mathbf{n}$) along the two centred parametric directions of the T-spline element. These are given by,

$$\begin{cases} L_\alpha = \displaystyle\int_{l_\alpha} dl \\ \widehat{T}_\alpha = \dfrac{1}{L_\alpha}\left|\displaystyle\int_{l_\alpha} d\mathbf{t}\right| = \dfrac{|\Delta \mathbf{t}|_{l_\alpha}|}{L_\alpha} \\ \widehat{V}_\alpha = \dfrac{1}{L_\alpha}\left|\displaystyle\int_{l_\alpha} d\mathbf{v}\right| = \dfrac{|\Delta \mathbf{v}|_{l_\alpha}|}{L_\alpha} \\ \widehat{\chi}_\alpha = \dfrac{1}{L_\alpha}\left|\displaystyle\int_{l_\alpha} d\chi\right| = \dfrac{|\Delta \chi|_{l_\alpha}|}{L_\alpha} \end{cases} \tag{4.26}$$

respectively, where l_α is the centred arclength of the element. Then, the elements are susceptible to be divided if the parameters exceed the following set of limits:

$$\begin{cases} L_\alpha > min\left\{ L_{ref}, L_{ref}\left(\dfrac{\widehat{T}_{ref}}{\widehat{T}_\alpha}\right)^{p_{ref}}, L_{ref}\left(\dfrac{\widehat{V}_{ref}}{\widehat{V}_\alpha}\right)^{p_{ref}}, L_{ref}\left(\dfrac{\widehat{\chi}_{ref}}{\widehat{\chi}_\alpha}\right)^{p_{ref}} \right\} \\ \text{or} \\ D_{ref} > \dfrac{L_\alpha}{L_\beta} \end{cases} \tag{4.27}$$

in which the sub-index $\cdot_{ref}$ denotes the reference limits, D_{ref} is the aspect ratio and p_{ref} is the reference order.

As it can be observed, the algorithm is based on the management of the aspect ratio and the two central arclengths of the element. The discrepancy between the variation of the physical variables with respect to the reference values acts as a penalty factor reducing the maximum size of the element in areas with high gradients. Moreover, the element can be divided independently in each direction producing two or four subelements. To avoid an excessive refinement, a minimal length (L_{min}) is set additionally. Once the elements are selected, they are divided by edge insertion under the analysis-suitable T-spline context and the nestedness requirements [56].

For deformable capsules, two geometrical maps need to be constructed: one corresponds to the reference configuration (or unstressed state), and other to the current configuration. The evaluation of the mesh quality is developed in the current configuration and the refinement process is carried out identically on both T-spline maps. In this way, both meshes preserve the same topology and parametrization that is convenient for the evaluation of the membrane stress. This strategy is general, and not all quality parameters have to be used. The selection of the appropriated parameter depends on the needs of the specific problem considered. A illustrative example of a local refinement process applied to a static mesh is shown in Fig 4.3. In Section 4.4 we will show the ability of this strategy for complex models with dynamic meshes.

4.3.4 Numerical procedure

To update the position of the capsule alongthe time and the value of the rest of physical variables (as the stress and strain of the membrane, velocity, pressure drop, etc.) a time integration scheme is needed. In the literature various schemes have been proposed to simulate deformable capsules in Stokes flows, and most of them are explicit methods [4, 5, 141, 167, 171–173]. These algorithms are conditionally stable. Note that the problem considered is strongly non-linear because the membrane can have large displacements and deformations and the constitutive law is non-linear. This fact linked to the high distortions that the mesh usually experience, can induce the instability of the explicit methods for a fixed time step. Our experience is that this instability is especially important when degenerated elements are present in the mesh as well as when the capsule is very stiff or the membrane undergoes a buckling process. In these

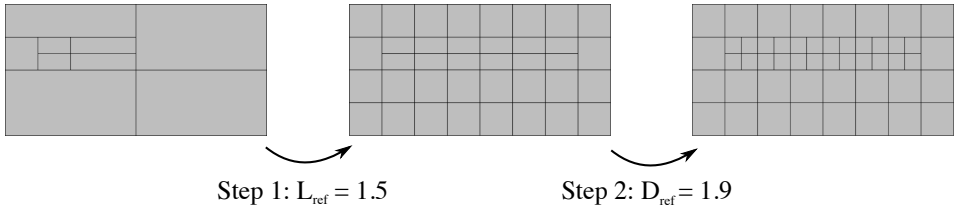

(a) The initial mesh has 9 physical elements with different sizes. A maximum size is set in the first step, resulting a finer mesh but with a variable aspect ratio of the elements. A maximum aspect ratio is fixed in the second step providing a more regular element size (50 physical elements at the end of the refinement process).

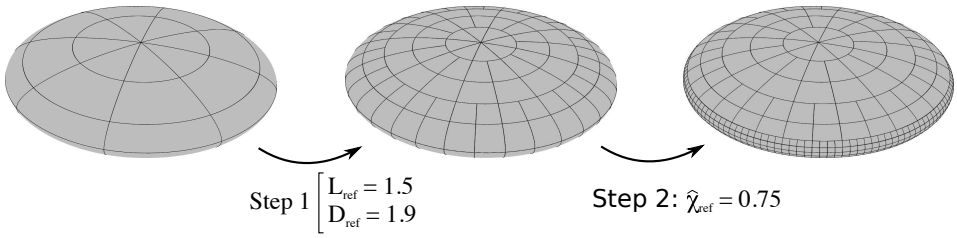

(b) The initial mesh contains 48 physical elements. In the first step a maximum size and maximum aspect ratio are selected, which lead to a finer mesh of regular elements. Then, a reference value of variation of mean curvature is set. This criterion produces a local refinement on the central region (720 physical elements at the end of the refinement process).

Figure 4.3: Local refinement applied on a static mesh for the case of (a) a ractangular plane with dimension 10×5 and (b) for the case of a spheroid with major and minor semi-axes 4 and 1, respectively. The refinement process is divided in two subsequently steps and only geometric aspects are considered.

situations a very small time step has to be set. This issue has motived us to use an implicit second-order scheme with a adaptive time step.

The Crack-Nicolson scheme is:

$$\mathbf{x}^{k+1}(t_{n+1}) = \mathbf{x}(t_n) + \frac{\Delta t_n}{2}\left(\mathbf{v}(t_n) + \mathbf{v}^k(t_{n+1})\right) \qquad k = 1, 2, ... \tag{4.28}$$

in which the t_n denotes the actual time and k is the sub-iteration number. To update the position of the membrane to the next time step t_{n+1} an iterative process is carried out until the normalized L^2-error of the control points satisfies a tolerance error $\|\mathbf{x}^{k+1}(t_{n+1}) - \mathbf{x}^k(t_{n+1})\|_{L_2}/(R_C\sqrt{m_C}) \leq \epsilon$, with R_C being the characteristic radius of the capsule (i.e the radius of the equivalent sphere with the same volume). The time step is modified in each iteration Δt_n , if it is necessary, until the integration scheme suitably converges to the imposed tolerance. This is, if the number of sub-iterations

k exceeds a maximum number (I_{max}) without reaching the tolerance, the time step is reduced by a factor. Whereas if the number sub-iterations needed is smaller than a defined number (I_{min}), the time step is increased by the same proportion. This strategy allows us to keep a suitable equilibrium between accuracy and computational cost as well as it improves the stability of the method. In fact, the time step is naturally adapted to the requirements of a dynamic adaptive mesh.

For second-order integration schemes, the convergence is expected when [5],

$$\frac{Q\Delta t_n}{\pi R_T^3} < O(\frac{hCa}{R_T}) \tag{4.29}$$

where R_T is the radius of the tube, h is the representative minimum element size of the capsule (defined as the square root of the element surface) and Ca is the capillarity number. Eq. 4.29 gives the order of magnitude of the time step needed and it can be used to select the value of the initial time step. In our simulations we set the tolerance error to $\epsilon = 10^{-7}$ and the maximum and minimum numbers of sub-iterations to $I_{max} = 8$ and $I_{min} = 4$, respectively, otherwise the time step is modified by a 25%. This election is made in base of experimental criteria and provides accuracy and suitable results as it will show in the numerical examples (Section 4.4).

The capillarity number and the ratio between radius of the capsule and the radius of the tube ($\delta = R_C/R_T$) are important parameters because they determine the motion and deformation of the capsule. The capillarity number relates the fluid stress on the membrane with the elastic stress. In the case of a capsule in a pulsatile flow it is defined as:

$$Ca = \frac{\mu\overline{Q}}{\pi R_T^2 G_s} \tag{4.30}$$

with $\overline{Q}$ being the temporal average ratio flow in a pulse.

It is convenient to remember that the T-spline basis functions are not interpolatory and the control values have not a physical meaning. In fact, the control points do not lie on the surface. Consequently, not any transformation of the surface can be directly applied to the control points (only linear transformations and translations: $\mathbf{x} \rightarrow \mathbf{Ax} + \mathbf{b}$). However, when an isogeometrical analysis is used, the basis functions are common for all physical variables and the updated process (Eq. 4.28) can be applied directly to the control points.

Although the BIE satisfies implicitly the null divergence of the velocity field through the fundamental solution, the volume of the capsule can experiece slightly changes. Three factors are mainly responsible for this: one comes from the discretization of the surface and velocity field; the second is related to the numerical integration of the kernels which introduces errors; and the time integration scheme is not conservative. These errors are usually relatively small but they are stored along the whole simulation. As proposed by [173] and to reduce this volumetric change, we slightly transform the fluid system to a minimization problem and constrain it to satisfy the net normal flux across the membrane to be null in each iteration. The constrained equation is written as,

$$\int_{\Gamma_C} \mathbf{v}(\mathbf{x}) \cdot \mathbf{n}(\mathbf{x}) d\Gamma = 0 \tag{4.31}$$

Assuming negligible inertial effects, we can observe that the fluid solver and the mechanical solver are uncoupled. In our numerical procedure we know the unstressed state and the shape of the membrane, and the current configuration at any time step. Thus, by applying the PVW equation (Eq. 4.19) we can compute the traction on the capsule. Then, introducing the jump stress into the fluid solver system (Eqs. 4.18, 4.17 and 4.31) we can obtain the velocity of the capsule. As pointed out by Pozrikidis [164], the fluid solver is considerably simplified when the internal and external fluids are isoviscous, such that the BIE on the capsule and on the tube are uncoupled and only it is necessary to compute the single layer operator. Once the velocity in the interface is computed, the shape is updated using the integration scheme (Eq. 4.28). To avoid constructing an unnecessarily large tube, we relocate the capsule in the middle of the tube at each iteration. After updating the capsule, we compute the variation of centroid of the capsule along the longitudinal direction $\Delta x_1^{vc} = x_1^{vc}(t_{n+1}) - x_1^{vc}(t_n)$ and subtract this value from the actual position (here we have supposed the tube is extended in the x_1-direction). This procedure is repeated until the final time is reached (see Fig. 4.4).

For completeness, the position of the centroid of the capsule at any time in boundary integral form is computed as,

$$\mathbf{x}^{vc} = \frac{1}{2\mathbb{v}} \int_{\Gamma_C} x_i^2 n_i(\mathbf{x}) \boldsymbol{\lambda}_i d\Gamma \tag{4.32}$$

where $\boldsymbol{\lambda}_i$ is the unit Cartesian vector in the i-direction and $\mathbb{v}$ is the actual volume of the capsule (note that we will use the upper-case to refer to the volume in the reference or unstressed configuration).

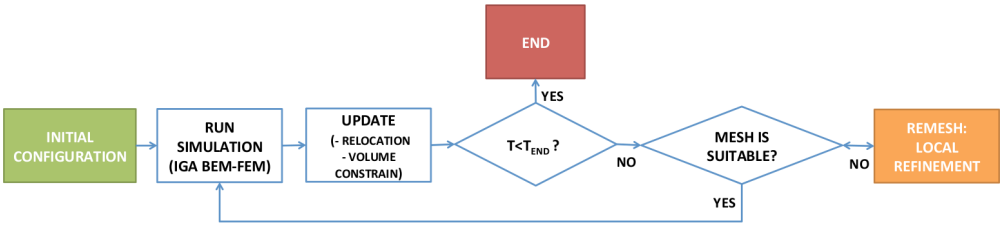

Figure 4.4: Schematic illustration of the numerical procedure

Additionally we also compute the average volumetric velocity ($\mathbf{v}^{vc}$) to follow the motion of whole capsule. This parameter can be expressed as,

$$\mathbf{v}^{vc} = \frac{1}{\mathbb{V}} \int_{\Gamma_C} \mathbf{v}(\mathbf{x}) x_3 n_3(\mathbf{x}) d\Gamma \tag{4.33}$$

It is defined the pressure drop coefficient in the tube as the ratio between the perturbed pressure drop due to the presence of the capsule and the unperturbed pressure drop in the tube,

$$\mathcal{P} = \Delta p^d / \Delta p^\infty \tag{4.34}$$

This coefficient is related with the theoretical apparent viscosity by the expression,

$$\mu_{app} = \mu(1 + \mathcal{P}) \tag{4.35}$$

and with apparent intrinsic viscosity by the equation,

$$k_T = \mathcal{P}/H_T \tag{4.36}$$

where H_T is the volume fraction tube hematocrit defined as the ratio of capsule volume to tube volume.

4.4 Numerical Examples

4.4.1 Uniform flow past a spheroid

In this section we validate the formulation of the IGA-BEM presented in the thesis and we check the spatial convergence of the method. The first example consists on a constant flow passing a fixed spheroid. We chose this problem because it has known

analytical solution (see [174]), the geometry is similar to a deformed capsule and it allows us to reveal some geometrical aspects that can impact in the accuracy of the method. Moreover, in contrast with the sphere, it represents a more general case since the curvature is variable. The particular BIE for the present problem is reduced to,

$$\mathbf{v}(\mathbf{x}_0) = (\widehat{\boldsymbol{\mathcal{H}}}_\Gamma \mathbf{v})(\mathbf{x}_0) - (\boldsymbol{\mathcal{G}}_\Gamma \Delta\mathbf{f})(\mathbf{x}_0) + \mathbf{v}^\infty(\mathbf{x}_0) \tag{4.37}$$

Although, physically it can be indistinctly considered that either the fluid is moved respect to the fixed spheroid ($\mathbf{v} = \mathbf{0}, \mathbf{v}^\infty \neq \mathbf{0}$) or the sphere is moved respect to the fluid ($\mathbf{v} \neq \mathbf{0}, \mathbf{v}^\infty = \mathbf{0}$), the change of the observer leads to a numerically different formulation. In order to check the suitable formulation of single and double layer kernels we assume the last option.

In this example, we define the spheroid through its volume $V = 4/3\pi a^2 b = 1$ and the relation between the semi-major axes and the semi-minor axes $b/a = 1.5$ (see Fig. 4.5), such that the semi-mayor axes is oriented vertically (x_3-direction). The incidental angle of the flow is set to $\theta = \pi/4$ with respect to the horizontal plane (x_1x_2-plane), thus the velocity of the body is given by $\mathbf{v} = -(cos\theta\boldsymbol{\lambda}_1 + sin\theta\boldsymbol{\lambda}_3)$.

We study two different topological representations of the spheroid (Fig. 4.5). One type corresponds to a structured mesh (Fig. 4.5a). The geometry is made from a regular sphere with unity radius that is appropriately transformed by two scale operations and where the poles are placed on the semi-major axis. The second representation (Fig. 4.5b) uses an unstructured mesh. The model is constructed by the projection from a regular cube to a spheroid. In both cases we set the weight to be unity and we chose continuous and smooth basis functions (expect in the poles that are C^0), because in dynamic problems the smoothness plays an important role in the stability of the results. Note that these models do not represent a geometrically perfect spheroid. A perfect spheroid could be constructed selecting the appropriate basis functions, but these would be piece-wise smooth. Moreover, in order to check the numerical convergence of the method, four different discretizatons of each model are selected. Particularly, for the structured mesh we set a number of $42, 146, 546$ and 2114 control points and $56, 218, 866$ and 3458 control points for the unstructured mesh. The coarsest mesh is shown in Fig. 4.5. For each level of refinement each Bézier element is divided into four elements.

An important aspect to take into account in the accuracy and convergence of the method comes from the accurate discretizacion of the normal field. The traction field

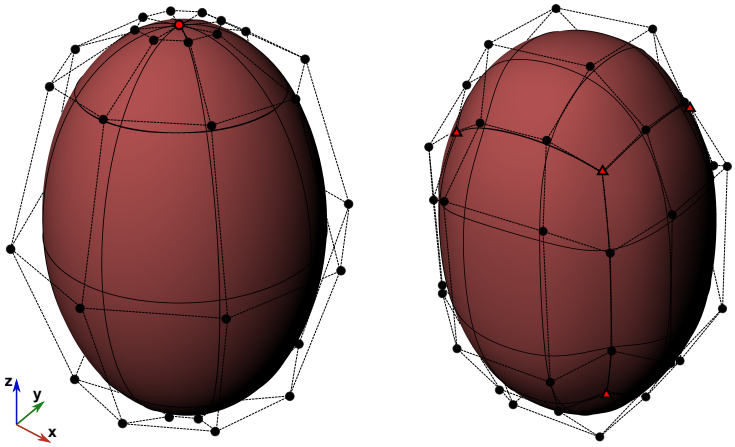

(a) (b)

Figure 4.5: a) Structured mesh and b) unstructured mesh of a spheroid. In (a) the red spherical control points denote the poles and in (b) the red triangular points are extraordinary points.

depends on the normal field as it is defined as $\mathbf{f} = \boldsymbol{\tau}\mathbf{n}$. In the context of isogeometric analysis, the analytical normal field can not be included into the finite space defined by the T-spline basis functions, and a geometric error is introduced in the numerical method. Consequently, the error of the discretized traction vector in this finite space, without considering other numerical aspects, is expected to be governed by the error of the discretized normal vector. Regarding this, in Fig. 4.6 we show the L^2-error between the analytical normal field and the discretized normal field for the structured and unstructured mesh as a function of the number of control points. The errors converge almost linearly when a logarithm scale is used. The average convergence ratio, defined as the logarithm slope, is 2.03 for the structured mesh and 1.62 for the unstructured mesh.

Note that the structured mesh implies the presence of degenerated elements. This fact can bring also negative consequences in the accuracy of the results, as it will be shown, if the singular elements are not suitablement addressed. Taus et al. [58] proposed to carry out a reparametrization of such elements based on the singular-value descomposition theorem accompanied of a global increasing of the number of quadrature points to improve the numerical integration of the kernels. On the other hand, Heltai et al. [19] implemented a non-singular BIE providing optimum results. The approach is based on the desingularization of the single and double layer operator forming a system of equation well conditioned. This technique requires to

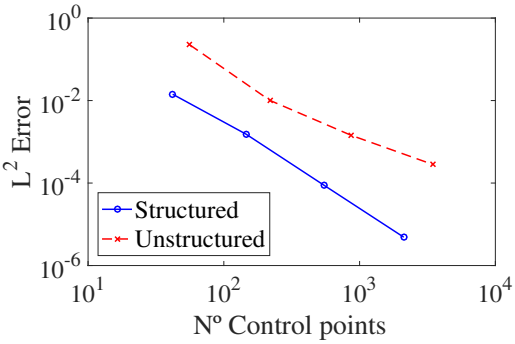

Figure 4.6: L^2-Error of the discretized normal field for the structured mesh (continuous line) and the unstructured mesh (dashed line).

rely on the differentiability of the geometry and it assumes that the normal is unique at the collocation points. This can not be guaranteed for all cases because when the Greville abcisae is used, the collocation points are placed at the poles where the continuity of the surface is locally C^0. A priori, for a fixed spheroid the normal is unique at these points though it can not be directly computed. However, in deformable capsules the normal can become not unique and the method is not applicable.

Fig.4.7 shows the results obtained with the standard BIE for the structured and the unstructured mesh, and those obtained by the desingularization of the kernels and by the Bézier transformation to non degenerated elements (explained in the Section 2.3) for the structured mesh. Regarding this last technique, the original degenerated elements have been subdivided in eight Bézier elements in the azimuthal direction to provide an accurate approximation of the original Bézier elements (in Table 4.1 we summarise the results for various subdivision levels). Fig. 4.7(a) depicts the L^2-error of the normal pressure on the spheroid. The error obtained with the standard formulation for the structured mesh practically is kept constant for all discretizations. This is attributed to the L^2-error is dominated by the error produced in the singular elements. However, for the rest of cases the error rapidly converges with a similar way, being the results obtained with the desingularizated technique and with Bézier transformation technique very similar. The average convergence ratios are 1.61 for the structured mesh (applying the Bézier trasnsformation technique) and 1.64 for the unstructured mesh.

Additionally, the total drag error on the spheroid with respect to the analytical solution is shown in Fig. 4.7(b). It is detected a erratic behaviour of the results

Subdivision	level 0	Level 1	Level 2	Level 3
Normal vector (L^2-error)	$1.332 \cdot 10^{-3}$	$3.494 \cdot 10^{-4}$	$8.947 \cdot 10^{-5}$	$8.947 \cdot 10^{-5}$
Pressure (L^2-error)	$6.499 \cdot 10^{-4}$	$2.362 \cdot 10^{-4}$	$1.825 \cdot 10^{-4}$	$1.781 \cdot 10^{-4}$
Drag (%Error)	$1.735 \cdot 10^{-6}$	$1.682 \cdot 10^{-6}$	$1.679 \cdot 10^{-6}$	$1.679 \cdot 10^{-6}$

Table 4.1: Errors of the normal vector, pressure and drag force on the spheroid for the structured mesh discreitized with 546 control points using the Bézier transformation technique. For each subdivision level the original degenerated Bézier element is subdivided in 2^{level} Bézier elements along the azimuthal direction.

computed with the standard formulation for the structured mesh, whereas for the others cases the error converge almost linearly (in a logarithm scale). The convergence ratio are 2.21 for the structured mesh and 2.28 for the unstructured mesh. These errors reveal that, in general, the structured mesh exhibit smaller errors than the unstructured mesh when the singular elements are suitable treated, but the converge ratios are similar and they are the same order than the converge ratios of the normal vectors.

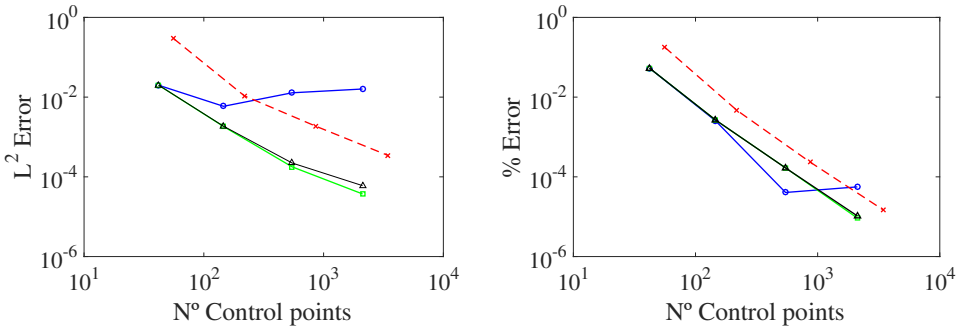

Figure 4.7: (a) L^2-error between the analytical and numerical normal force on the spheroid and b) percentage error of the drag force on the spheroid. Standard BIE for structured mesh: continuous line with circles; standard BIE for unstructured mesh: dashed line with crosses; desingularized BIE for structured mesh: continuous line with triangles and BIE with Bézier transformation technique for structured mesh: continuous line with squares.

Fig. 4.8 shows the point-wise error of the normal pressure on the spheroid surface with respect to the analytical solution. It is observed that the error is concentrated around the poles when not specific treatment is applied on singular elements. The error is reduced and more uniformly distributed after applying a Bézier transformation technique to the degenerated elements. For the unstructured mesh, although the error

is also distributed along all the surface of the spheroid, is found to be higher around the extraordinary points.

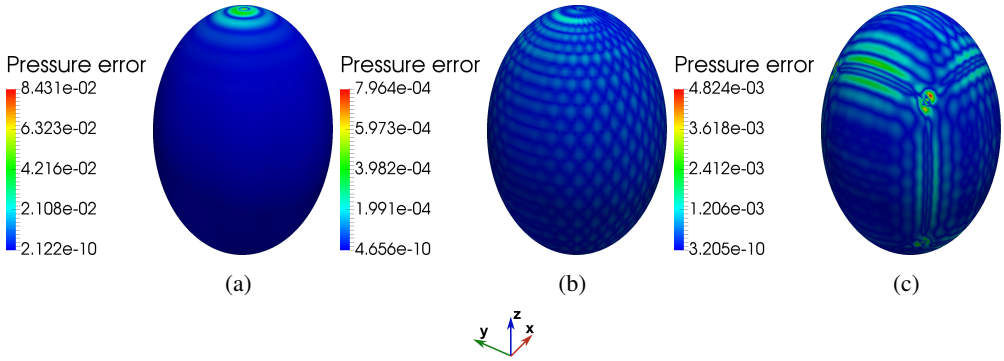

Figure 4.8: Point-wise error of the normal pressure on the spheroid for the structured mesh discretized by 546 control points (a) without using any treatment on degenerated elements and (b) using the Bézier transformation technique, and (c) for the unstructured mesh discretized by 866 control points.

4.4.2 Capsule in shear flow

The objective of this section is to analyse the temporal stability and accuracy of the coupled IGA BEM-FEM formulation. To check this feature, we simulate the deformation of a capsule immersed in a shear flow. Although this problem has not known analytical solution, several authors have extensively studied it, reporting numerical results for a wide range of different problem parameters [4, 5]. We focus on the case of an initial spherical isoviscous ($\kappa = 1$) capsule with a Neo-Hookean law for the membrane. The BIE for this problem is reduced to,

$$\mathbf{v}(\mathbf{x}_0) = -(\boldsymbol{\mathcal{G}}_\Gamma \Delta\mathbf{f})(\mathbf{x}_0) + \mathbf{v}^\infty(\mathbf{x}_0) \tag{4.38}$$

where the unperturbed flow is given by $\mathbf{v}^\infty = \dot{\gamma} x_3 \boldsymbol{\lambda}_1$ and $\dot{\gamma}$ is the shear rate.

By the action of this flow, the capsule is deformed until reaching a steady shape. Even in this steadiness of the shape, the membrane moves and rotates with respect to the internal fluid. This phenomenon is known as tank-treading. In this state the capsule acquires a shape similar to an ellipsoid with the major-axis contained in the shear plane. Consequently, it is usual to quantify the deformation of the capsule through the

Taylor parameter:

$$D_{12} = \frac{L_1 - L_2}{L_1 + L_2} \tag{4.39}$$

where L_1 and L_2 are the largest and shortest semi-axes measured from the centroid to the surface, respectively. This parameter provides a measure of the change of shape.

The motion and deformation of the capsule is characterized by the capillarity number, that for this particular case is defined as $Ca = \mu\dot{\gamma}R_C/G_s$. In fact, there are a low and a high critical capillarity number from which the capsule does not reach a stable equilibrium. In what follows we compare the temporal deformation of the capsule obtained by the present formulation with those presented by Lac et al. [4] for various stables values of capillarity $Ca = 0.3, 0.45$ and 0.6 and different meshes.

Without loss of generality, we consider an initial sphere with radius unity. As in the previous example, we consider two topological representations of the capsule. One made by a regular structured mesh and the other with an unstructured mesh. The structured mesh has 842 control points, whereas the unstructured mesh is constructed by a cube projection with 866 control points. The Bézier transformation technique is used to avoid the presence of degenerated elements. The initial dimensionless time step is set to $\dot{\gamma}\Delta t_0 = 0.01Ca$. The simulation is stopped at the dimensionless time $\dot{\gamma}t_{end} = 25Ca$ to guarantee that the steady state is reached.

In Fig. 4.9a we show the time evolution of the Taylor parameter for the unstructured mesh and three different capillarity numbers. It is observed that the present results are very close to those reported in the literature [4] for all capillarity numbers considered. The angles of the principal direction of capsule with respect to the flow at the steady state (Fig. 4.9b) were also measured and are in agreement with those obtained by [4]. We also studied the influence of the time step. We ran simulations with a fixed time step and with an adaptive scheme for the case of the unstructured mesh and $Ca = 0.45$. The relative difference of the deformation parameter in the steady state for both simulations is practically negligible ($5.7 \cdot 10^{-5}\%$). However, using the adaptive model the time step increases during the simulation reaching a maximum value $\Delta t = 5.619\Delta t_0$ and the average value is $\Delta t = 4.327\Delta t_0$. Another illustrative indicator to verify the accuracy of the method is the time evolution of the volumetric change of the capsule ($E_{\mathbb{v}}(t) = \Delta\mathbb{v}/\mathbb{V}$). We analysed the effect of the volumetric constrain Eq.4.31. The results are summarized in Table 4.2 for the unstructured mesh. It is observed that the volumetric error remains low for all cases ($E_{\mathbb{v}} \leq O(10^{-3})\%$) and it increases with the capillarity, as it is expected because the capsule suffers

larger deformations. Moreover, the volumetric error significantly decreases when the volumetric constrain equation is used.

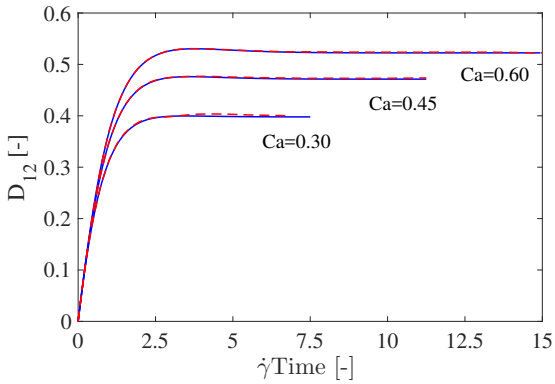

(a)

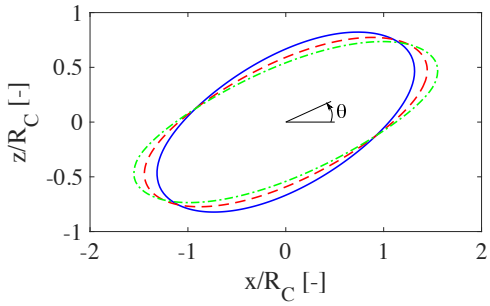

	θ [rad]		
	Ca=0.30	Ca=0.45	Ca=0.60
Present	0.443	0.387	0.349
Lac et al	0.44	0.38	0.35

(b)

Figure 4.9: (a) Evolution of the Taylor deformation parameter of the capsule (Neo-Hookean membrane) in a shear flow for the unstructured mesh and three capillarity numbers ($Ca = 0.3, 0.45$ and 0.6). Continuous line: present results and dashed line: results obtained by Lac et al. [4]. (b) Steady shape of the capsule in the shear plane for the unstructured mesh for $Ca = 0.30$ (solid line), $Ca = 0.45$ (dashed line) and $Ca = 0.60$ (dot and dash line). The inserted table contains the angles between the principal axis of the deformed capsule and the flow direction computed by the present method and reported by [4].

A special attention should be paid in the case of the structured mesh. The mesh is heterogeneous and the aspect ratio of the elements (ratio between length and width) is very variable. In fact, the elements around the poles show an aspect ratio far from

	$E_v(t) = \frac{\Delta v}{V}\%$					
	$Ca = 0.3$		$Ca = 0.45$		$Ca = 0.6$	
	$Avg(E_V)$	$max(E_V)$	$Avg(E_V)$	$Max(E_V)$	$Avg(E_V)$	$Max(E_V)$
Volume constrain	$3.378 \cdot 10^{-5}$	$4.511 \cdot 10^{-5}$	$6.159 \cdot 10^{-5}$	$9.325 \cdot 10^{-5}$	$2.065 \cdot 10^{-4}$	$1.173 \cdot 10^{-3}$
Non volume constrain	$4.449 \cdot 10^{-4}$	$9.892 \cdot 10^{-4}$	$1.434 \cdot 10^{-3}$	$3.322 \cdot 10^{-3}$	$2.957 \cdot 10^{-3}$	$5.841 \cdot 10^{-3}$

Table 4.2: Average and maximum volumetric error of the capsule in shear flow for the structured mesh and various capillarity numbers ($Ca = 0.3, 0.45$ and 0.6).

the ideal unit value. That linked with the loss of continuity and the sigularity of the degenerated elements, produces an important source of numerical problems. Joneidi et al. [173] found numerical instabilities around the poles for a deformable capsule discretized with a NURBS. Similar finding were reported by Lac et al. [4] using bi-cubic B-spline functions. In this last work the authors analysed the influence of the initial position of the poles and found that the simulations were unstable when they were placed in axes out of the shear plane ($x_1x_3 - plane$) where the membrane is compressed. In the present work, we find that these instabilities can be avoided making a suitable numerical integration of the degenerated elements, this is, by applying the Bézier transformation technique or the technique proposed by Taus et al.[58], and using an adaptive implicit temporal integration scheme. We carried out some simulations with the poles contained in the x_2-axis and for $Ca = 0.45$. Using a fixed time step ($\Delta t_n = \Delta t_0 = 0.01Ca$), the temporal integration scheme does not converge at the early stages and it must be reduced at least a 25% to provide stable results. This can be naturally overcome using a adaptive scheme. Another important aspect regarding the stability is the method chosen for the computation of the load on the membrane. Our simulations reveal that the instabilities appear when the equilibrium equation in strong form is used instead of the variational principle, even with the utilization of an adaptive integration scheme. Nevertheless, the variational principle provides stable results independently of the position of the poles. Fig. 4.10 shows the typical instability produced around the poles and the steady stated when a suitable method is applied. The relative discrepancy of the deformation parameter between the unstructured and the structured mesh in the steady state is $4.4 \cdot 10^{-5}\%$ for $Ca = 0.30$, $3.4 \cdot 10^{-3}\%$ for $Ca = 0.45$ and $1.2 \cdot 10^{-3}\%$ for $Ca = 0.6$.

4.4.3 Dynamic mesh

In this section we show the ability of the present approach to adapt dynamically the mesh to the needs of the problem. Two examples are shown. The first example consists

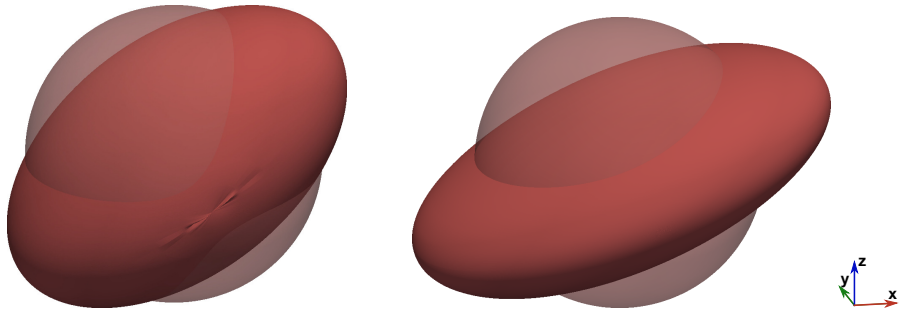

(a) (b)

Figure 4.10: (a) Instability of the capsule around the poles when these are located in the x_2-axis and the equilibrium equation in strong form on the membrane is used (at $\dot{\gamma}t = 0.664$) and (b) steady state of the capsule using the variational principle for the Capilarity number $Ca = 0.45$. The transparent sphere corresponds to the initial state and the solid surface to the deformed state.

on the movement of a micro-drop immersed in a four-roll flow. Although is not a capsule, this example is significant becasue the error is very sensitive to the quality of the mesh. For comparability purposes, we analised a particular case for which results have be previosly reported numerically and experimentally in the literature [37, 175]. Taking the notation from [37] the unperturbed flow can be expressed as:

$$\begin{cases} v_1 = \dfrac{\dot{\gamma}}{2}\left((1+a_f)x_1 + (1-a_f)x_3\right) \\ v_2 = 0 \\ v_3 = \dfrac{\dot{\gamma}}{2}\left((-1+a_f)x_1 - (1+a_f)x_3\right) \end{cases} \tag{4.40}$$

where a_f is set to 0.6. The viscosity ratio is $\kappa = 0.118$ and the capillarity number is given by $Ca = \frac{\dot{\gamma}\mu R_C}{\sigma} = 0.196$ being σ the superficial tension and R_C the radius of the drop (see Fig 4.11).

The computation of the jump stress on the drop surface depends purely on geometric aspects ($\Delta\mathbf{f} = (\nabla \cdot \mathbf{n})\mathbf{n}$). Consequently, the motion of the interface is described solely by the BIE:

$$\mathbf{v}(\mathbf{x}_0) = (1-\kappa)(\widehat{\boldsymbol{\mathcal{H}}}_\Gamma \mathbf{v})(\mathbf{x}_0) - (\boldsymbol{\mathcal{G}}_\Gamma \Delta\mathbf{f})(\mathbf{x}_0) + \mathbf{v}^\infty(\mathbf{x}_0) \tag{4.41}$$

By the action of flow, the drop is deformed and it adopts a shape similar to an ellipsoid in the steady regime. Note that the fluid particles on the interface are not

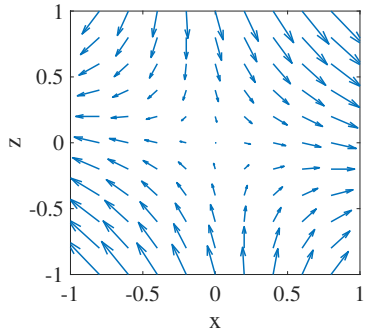

Figure 4.11: Umperturbed velocity field for a four-roll flow with $a_f = 0.6$

bounded. This is, the particles can move freely over the interface due to the net fluid stress on both sides. Usually, this produces a migration of the particles to preferential zones of the interface, leaving other areas with low concentrations. This linked to the large deformation of the drop can lead to unsuitable large distortion of the mesh. In such a case it is especially important the use of a dynamic local refinement to provide accurate results. Additionally, since the tangential motion of the interface does not affect to the dynamic of the drop [37, 173], it can be omitted in the update process of the interface which helps to manage the distortion of the mesh.

As in the previous example, the simulation starts from a sphere with unit radius. A regular structured mesh with 222 control point is used. This discretization is not fine enough to capture accurately the large deformation of the drop, as it will be shown in what follows. Given the characteristics of this problem, the suitability of the mesh is evaluated as a function of the variation of the curvature and the aspect ratio of the elements. It should be noted that the tractions are proportional to the mean curvature, thus this parameter is representative of the geometry discretization, as well as, the discretization of the physical variables (traction and velocity). In this case, the reference parameters are set to: $L_{ref} = 0.32R_C$, $\widehat{\chi}_{ref} = 2/R_C^2$, $D_{ref} = 2$, $p_{ref} = 2$ and $L_{min} = 0.05R_C$. In the degenerated elements, the aspect ratio criteria unnecessarily generates a dense refinement due to its inherent distortion, thus the refinement is not applied. The initial time step is $\dot{\gamma}\Delta t = 0.005$. The simulation finalize once the steady shape is reached at $\dot{\gamma}t_{end} = 10$.

Fig. 4.12 shows the time evolution of the Taylor parameter. It can be observed that the present results are very close to the numerical results reported by Wang and Dimitrakopoulos [172]. Moreover, the deformation of the drop in the steady state

($D_{12}^{\infty} = 0.381$) is in good agreement with the experimental findings of Bentley and Leal [175] ($D_{12}^{\infty} = 0.381$). However, if a scheme without refinement is applied, the accuracy of the results is considerably reduced (relative discrepancy 8.312%). This reveals the importance of a suitable discretization of the drop. Various refinements are carried out during the simulation. In Fig 4.13 the discretization of the drop is represented at three different stages, this is, at the beginning, at an intermediate state and at the steady state. As the drop is deformed, the variation of the curvature increases rapidly around the two endpoints corresponding to the principal inertia axis of the drop and various local refinements are performed. At the end of the simulation the drop contains a total of 844 control points.

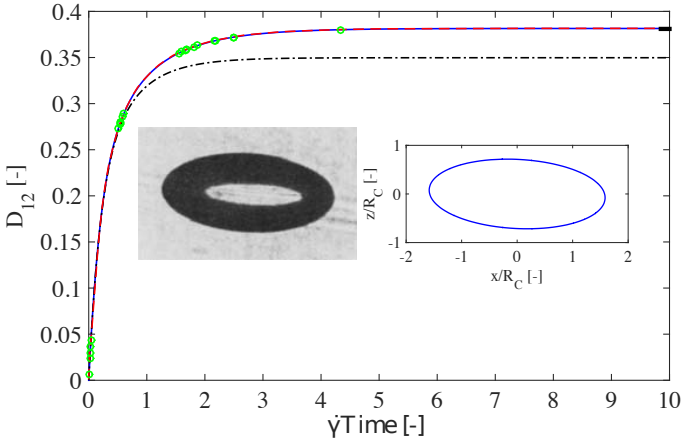

Figure 4.12: Time evolution of the Taylor parameter of a drop in a four-roll flow for the capillarity number $Ca = 0.196$ and viscosity ratio $\kappa = 0.118$. Continuous line: present results appliying a dynamic refinement; dot dash line: present results without refinement; and dashed line: numerical result reported by Wang and Dimitrakopoulos [172]. The circles reveal the times at which a refinement is applied to the drop. The dash marker '-' on the left corresponds to the Taylor deformation experimentally found by Bentley and Leal [175] at the steady state. The inset (a) is the experimental shape reported in [175] [1]and (b) shows the shape of the drop obtained by the present approach in the steady state.

Secondly, we studied the movement of an isoviscous capsule in a hyperbolic flow following a Sakalt law with $\mathsf{C} = 1$. The unperturbed flow can be expressed as Eq. 4.40 with $a_f = 1$. As in the previous case, the capsule evolves into a shape similar to an ellipsoid. This problem has been analysed by several authors using a BEM approach [4, 5, 141]. Lac et al. [4] found numerical instabilities when the capillarity number

[1]Used with permission

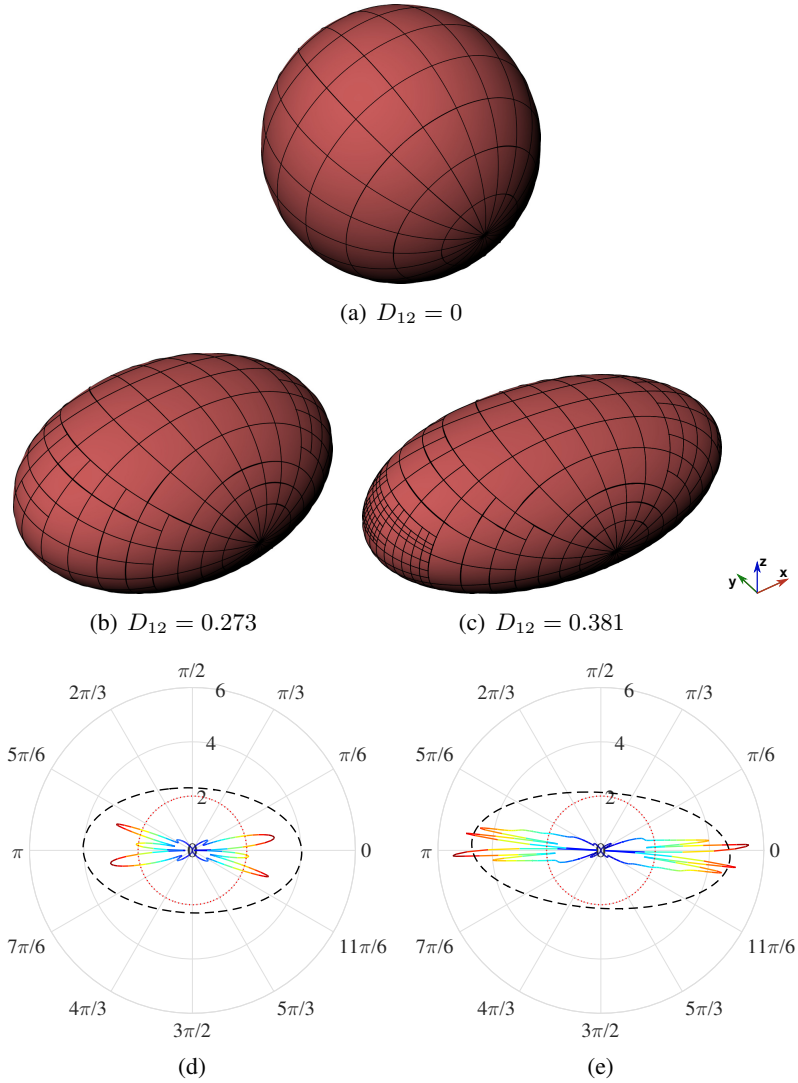

(a) $D_{12} = 0$

(b) $D_{12} = 0.273$ (c) $D_{12} = 0.381$

(d) (e)

Figure 4.13: Discretization of the drop in a four-roller flow applying a dynamic refinement (a) at the beginning $\dot{\gamma}t = 0$, (b) in an intermediate state $\dot{\gamma}t = 0.509$ and (c) in the steady state $\dot{\gamma}t = 10$. (d) and (f) variation of the mean curvature of the vertical section of the drop ($x_1x_3-plane$) represented in a polar coordinate system at $\dot{\gamma}t = 0.509$ and $\dot{\gamma}t = 10$, respectively. Dashed line: scale representation of the section of the drop ($E = 3:1$); solid line: variation of the curvature ($\frac{d\chi}{dl}$); and dotted line: limit value of the variation of the curvature ($\widehat{\chi}$).

is larger than the value 0.7. Dodson and Dimitrakopoulus [141] found stable results for higher values of capillarity number ($Ca > 0.7$) as well as Walter et al. [5]. They observed that the capsule acquires very high values of the mean curvature during the

transitory phase and that can lead to numerical problems. Given these findings, we check the ability of the present approach to simulate such a problem for capillarity numbers $Ca = 0.45, 0.60$ and 0.8. The use of a dynamic local refinement scheme is needed, otherwise an excessive fine discretization should be carried out during the whole simulation.

The simulation is initialized using an unit radius sphere. In this case, the sphere is discretized with an unstructured mesh with 218 control points and constructed using a regular cubic projection (Fig. 4.15a). The suitability of the mesh is managed through the variation of the traction on the membrane. Thus, the reference values are set to: $L_{ref} = 0.35R_C$, $\widehat{T}_{ref} = 8G_s/R_C$ $D_{ref} = 2.5$, $p_{ref} = 1$ and $L_{min} = 0.035R_C$. These rules were established experimentally and based on the deformation of the capsule at the steady state.

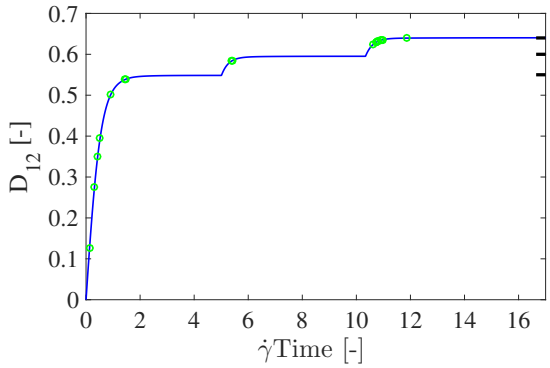

Figure 4.14: Time evolution of the Taylor parameter of a capsule in a four-roll flow for the capillarity $Ca = 0.45, 0.60$ and 0.80. The circles reveal the times at which a refinement is applied. The dash marker '-' on the right corresponds to the Taylor parameter found by Walter et al. [5] at the steady state.

The simulations for the different capillarity numbers were carried out subsequently from the deformation of the capsule of the previous capillarity numbers. In all case stable results were found after a transient. The obtained Taylor parameters at the steady state are $D_{12}^{\infty} = 0.548, 0.595$ and 0.640 for $Ca = 0.45, 0.06$ and 0.80, respectively, which are in good agreement with those reported by Dodson and Dimitrakopoulos [141] ($D_{12} = 0.548$ and 0.595 for $Ca = 0.45$ and 0.6) and Walter et al. [5] ($D_{12} = 0.55, 0.60$ and 0.64 for $Ca = 0.45, 0.6$ and 0.8) (see Fig. 4.14). The discretization of the capsule in the steady state as well as the variation of the tractions are illustrated in Fig. 4.15. The capsule suffers very large deformations (larger for higher values of Ca)

and the variation of tractions are very high around the tips of the capsule that requires a fine mesh in theses areas. The total number of control points at the steady state is 706 for $Ca = 0.45$, 906 for $Ca = 0.6$ and 1478 for $Ca = 0.8$. The volumetric error remains in the order of $O(10^{-3}\%)$ for all simulations.

In Fig. 4.16 is shown a comparative of the capsule shape for the capillarity $Ca = 0.80$ at the steady state between a fixed mesh and a dynamic mesh. Despite that the fixed mesh has a low number of elements, the capsule shapes for both discretization are surprising close. It is around the tips where the maximum discrepancy appears due to the high variation of the curvature and tractions which can not be accurately captured with the coarse mesh. In fact, the traction discrepancy is considerable high (17.32%) as it can be seen in Fig. 4.17.

4.4.4 Capsule in a pulsatile tube flow

In this section we analyse the motion of a deformable capsule in a micro-channel with a pulsating flow. According to our knowledge, this problem has not been reported in the literature and it has important implications in biological flows. Nevertheless, far to elaborate a parametric studio, we focus the discussion in the ability of the present approach to simulate the behaviour of deformable capsules in a confined channel with pulsatile flow.

We consider an initial spherical isoviscous capsule following a Skalat law with $\mathsf{C} = 1$. The channel is a long cylindrical tube of constant section. The ratio between the capsule radius and tube radius is set to $\delta = R_C/R_T = 0.5$. The tube has a length of $L_T = 2\pi R_T$ which is enough to assume the contribution of the disturbed flow at the inlet and at the outlet as it was assumed in Section 4.3.1 [164]. Initially the centre of capsule is placed in middle of the tube and at a radial distance $r_C = 0.25R_T$ under the centreline (See Fig. 4.18). This configuration makes the problem non axisymmetric. The capsule is discretized using an unstructured mesh with 602 control points and it is constructed with a regular cube projection. The tube is modelled with a structured mesh with 19×24 control points. The tube is construct by applying a revolution operation around the central axis providing a perfect geometrical representation. Three levels of refinement are imposed along the tube, concentrating the mesh around the capsule (Fig. 4.18).

The unperturbed flow inside the tube is governed by the Womersley solution for a pulsatile flow [176]. In the Stokes regime the inertia effects are negligible and the

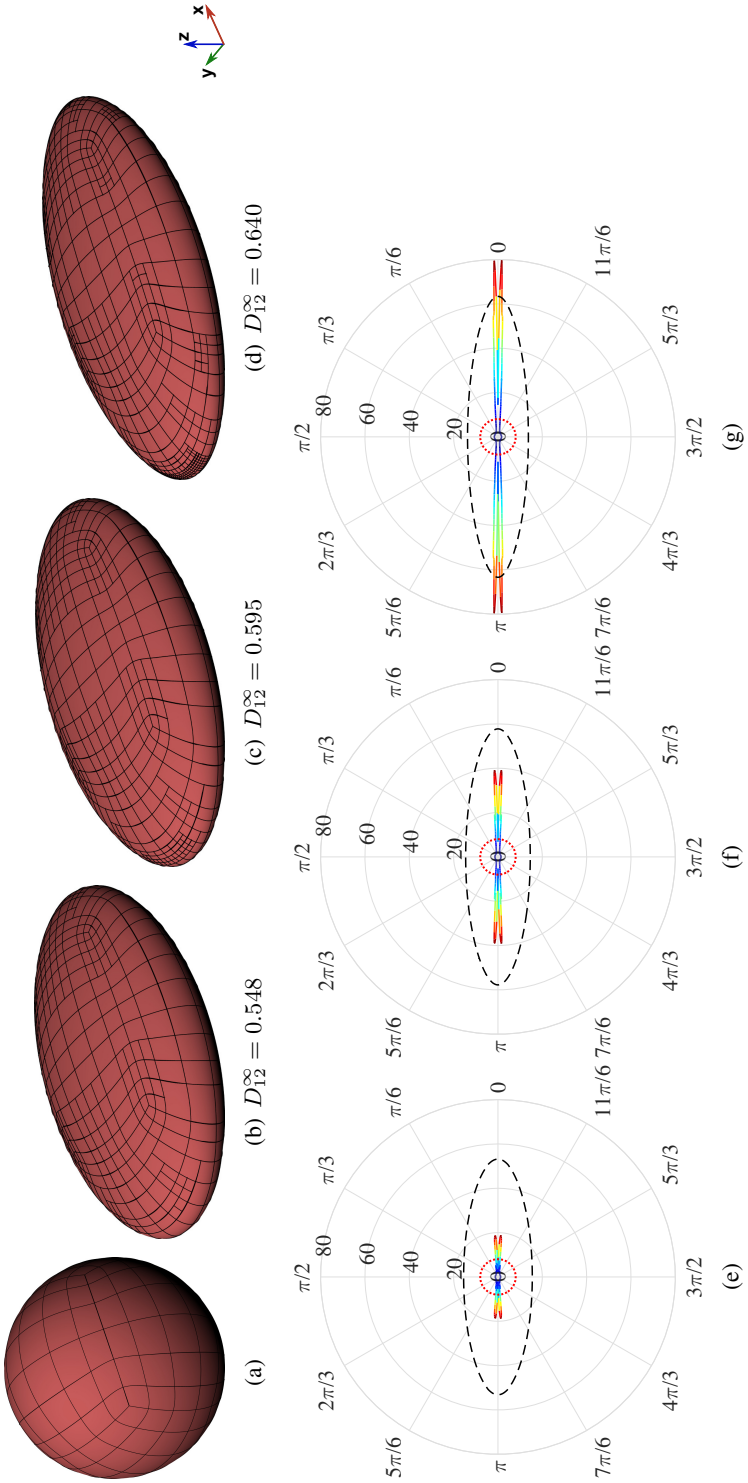

Figure 4.15: Discretization of the capsule in a hyperbolic flow (a) at the initial time and at the steady state for (b) $Ca = 0.45$, (c) $Ca = 0.60$ and (d) $Ca = 0.8$ after applying a dynamic refinement. (e),(f) and (g) Variation of tractions in the meridional plane of the capsule ($x_1x_3 - plane$) represented in a polar coordinate system at the three respective capillarity numbers. Dashed line: scale representation of the section of the drop ($E = 30 : 1$); solid line: variation of the tranctions ($\frac{dt}{dl}$); and dotted line: limit value of the variation of the traction ($\widehat{T}$).

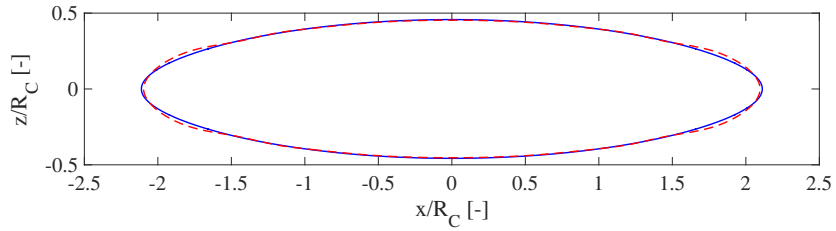

Figure 4.16: Capsule shape in a four-roll flow with $Ca = 0.8$ at the steady state. Solid line: after applying a dynamic refinement; dashed line: without remeshing.

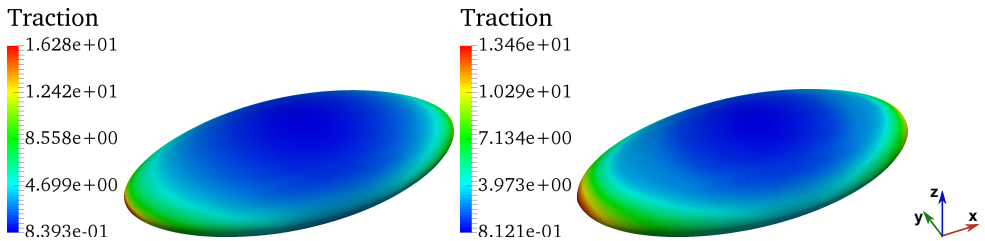

(a) (b)

Figure 4.17: Tractions on the membrane for a capsule in a four-roll flow with $Ca = 0.8$ at the steady state (a) after applying a dynamic refinement and (b) without remeshing.

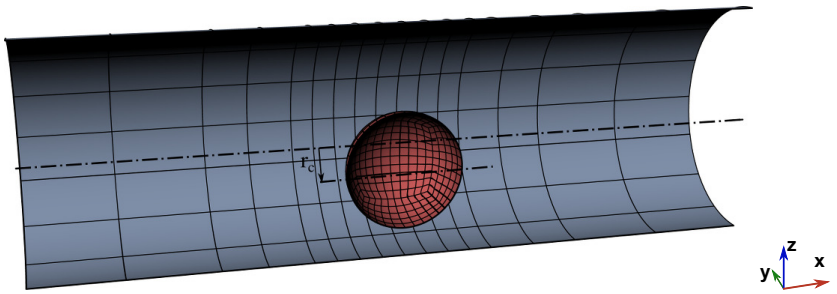

Figure 4.18: T-spline model for the non-axisymmetric problem of a capsule flowing in a cylindrical tube. For clarity, only the half of the model is represented.

solution can be simplified to a periodic Poiseuille flow. Consequently the unperturbed flow can be expressed as:

$$\mathbf{v}^{\infty}(r,t) = [\Delta v(r) cos(\omega t) + v_0(r)]\, \boldsymbol{\lambda}_1 \tag{4.42}$$

where r is the radial distance from the axis of the tube, ω is the frequency of the pulse, $\Delta v(r)$ is the temporal amplitude of the pulse and $v_0(r)$ is a constant velocity.

These last two terms obey to the parabolic profile of Poiseuille flow, this is, $f(r) = 2f_m(1-(r/R_T)^2)$ with f_m being the mean velocity in the section. Thus, the flow rate is give by:

$$Q^{\infty}(t) = \frac{\Delta P^{\infty}(t)\pi R_T^4}{8\mu L} = \left[\Delta v_m^{\infty} cos(\omega t) + v_{0m}^{\infty}\right]\pi R_T^2 \tag{4.43}$$

in which $\Delta P^{\infty}(t)$ is the unsteady pressure drop along the tube length.

Additionally we assume a positive difference of pressure (p_{os}) between the interior and exterior of the capsule. This situation appears naturally in capsules with semi-permeable membrane because of different concentration of any substance between both side of the membrane (i.e. osmotic pressure). For a spherical isotropic capsule, this pressure jump can be taken into account by a pre-inflation of the capsule from a radius $R_{C.pi}$ to a radius of $R_C = (1+\alpha)R_{C.pi}$, causing an isotropic internal stress $\tau_{iso} = 1/2 p_{os} R_C$. Among other effects, the pre-inflation of the capsule helps to prevent the buckling of the membrane. This phenomenon can not be managed by the present approach due to the lack of bending stiffness in the membrane, and it can lead to the instability of the model. Some authors studied with more details the effect of pre-stressed capsules for different flows [4, 6, 139]. In this case we assume a low expansion coefficient $\alpha = 0.025$.

We considered a representative value of the shear modulus of a biological capsule $G_s = 6 \cdot 10^{-6} N/m$, the fluid viscosity $\mu = 1.2 \cdot 10^{-3} Ns/m^2$ and the average flow velocity within the range $v_{0m}^{\infty} = [0.375 - 1.500] mm/s$. Continuing with a non-dimensionless analysis, we carried out some simulations for the capillarity mumbers $Ca = [0.075, 0.15, 0.30]$ (Eq. 4.30), amplitude of the pulse $\Delta v_m^{\infty}/v_{0m}^{\infty} = [0, 1/3, 2/3]$ and angular velocity $\omega' = \omega R_T / v_{0m}^{\infty} = [2/3\pi, 2\pi, 6\pi]$.

First, we checked the validity of the present model simulating a non-pulsating flow ($\Delta v_m^{\infty} = 0$) with the capsule placed in the axis of the tube ($r_C = 0$) and we compared our results with that reported by Lefebvre and Barthès-Biesel [6] for an axisymmetric model with capillarity number $Ca = 0.06$, $\delta = 0.8, 0.9$ and $\alpha = 0.025$. I can be seen in Fig. 4.19 that the agreement between both predictions of the shape of the capsules at the steady state is very good.

Fig. 4.20a and 4.20b represent the time evolution of the capsule shape initially placed at $r_C = 0.25 R_C$ for a steady ($Ca = 0.15$) and pulsatile ($Ca = 0.15$, $\Delta v_m^{\infty}/v_{0m}^{\infty} = 2/3$ and $\omega' = 2\pi$) flow, respectively. The frame of reference is jointly

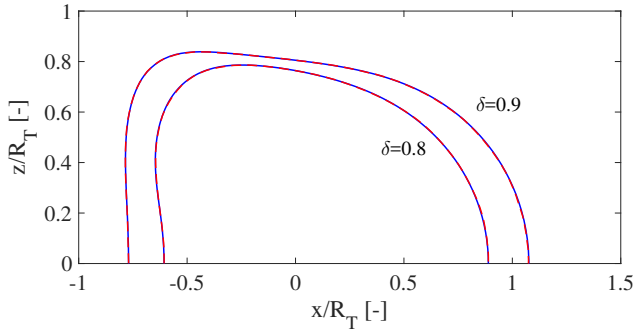

Figure 4.19: Profile of a Skalat deformable Capsule ($\mathsf{C} = 1$) flowing in a cylindrical tube by the action of constant flow for $Ca = 0.06$, $\delta = 0.8$ and 0.9, $r_C = 0$ and $\alpha = 0.025$. Only a half of the profile is represented given the axisymmetry of the problem. Pressent result for a three dimensional model: continuous line; relults reported by Lefebvre and Barthès-Biesel [6] for a axisymmetric model: dashed line; and original pre-inflated capsule: dotted line.

moved with the centroid of the capsule along the axial direction. It can be seen in Fig. 4.20a that during a first transient period, the capsule is rapidly deformed adopting a non-symmetric shape. The front increases the concavity whereas the rear becomes nearly flat. Then, the capsule is slowly deformed as it asymptotically migrates to the centreline of the tube. In this way, the rear acquires a convex shape and tends to have a symmetric parachute shape. This shape is the typical deformation for initial spherical capsules in axisymmetric problems [6, 177]. Similarly, for a pulsatile flow (4.20b) we find a transient period of fast deformation followed by the slow migration to the centreline. The characteristic shape of the capsule is similar to the previous case, however the capsule evolves in a quasi-periodic way due to the pulsating character of the flow. Fig 4.20b shows the typical oscillations of the capsule corresponding to the maximum, medium and minimum surface deformation in a cycle. A 3D view of the capsule at different times is represented in Fig. 4.20c.

We select the surface area variation of the capsule as a representative parameter of the surface deformation. This quantity measures the change of the surface area from the initial (after the pre-inflation) to the actual configuration ($\Delta s/s_0 = (s(t) - s_0(t = 0))/s_0(t = 0)$ with s being the total surface area) and it is related to the strain on the membrane. Fig. 4.21a shows the time evolution of $\Delta s/s_0$ for a pulsatile flow with $Ca = 0.15$, $\omega' = 2/3\pi$ and three different amplitudes. The zero amplitude corresponds to a non-pulsatile flow. In this case it is observed clearly the initial transient period until reaching a maximum area change and then the slow evolution

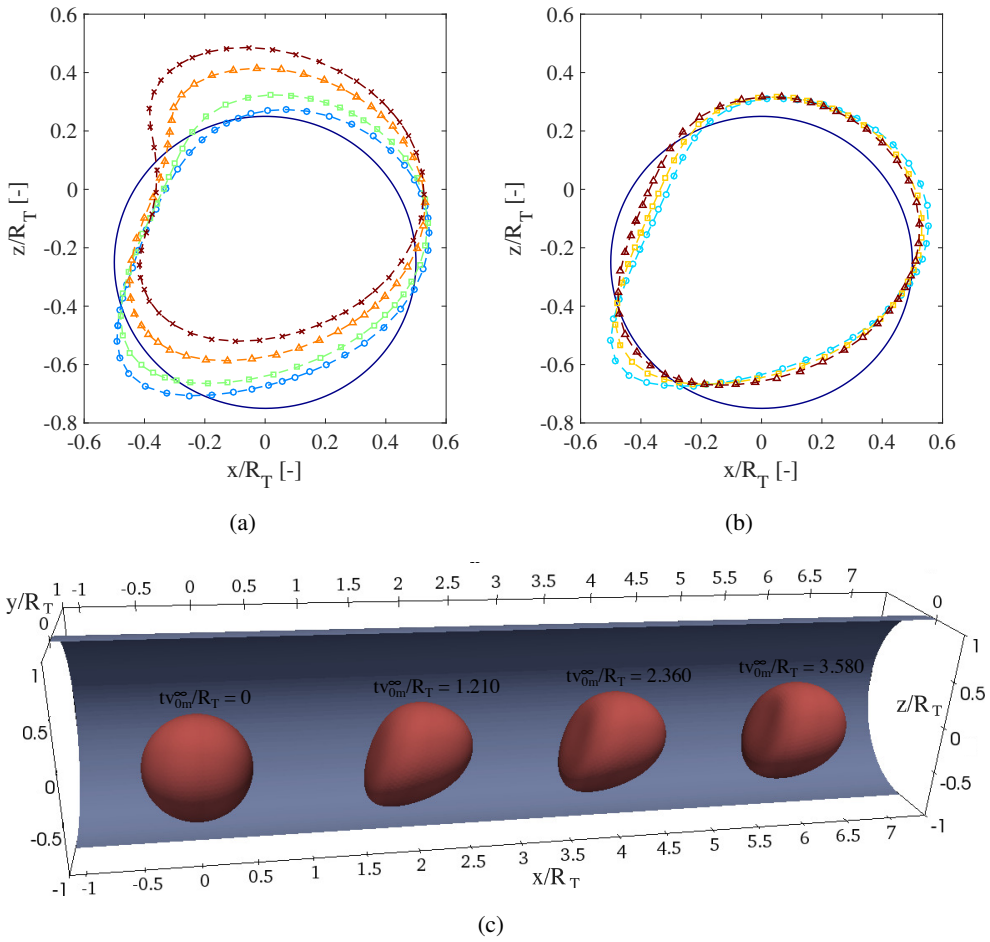

Figure 4.20: (a) Time evolution of the capsule shape in a constant flow with $Ca = 0.15$ and $r_C = 0.25R_T$ at the times $tv_{0m}^{\infty}/R_T = 0.000$ (solid line) 1.185 (circles), 3.754 (squares), 11.249 (triangles) and 37.500 (crosses). (b) Evolving shape for a pulsatile flow with $Ca = 0.15$, $r_C = 0.25R_T$, $\Delta v_m^{\infty}/v_{0m}^{\infty} = 2/3$ and $\omega' = 2\pi$ at the times $tv_{0m}^{\infty}/R_T = 0.000$ (solid line), 2.414 (circles), 2.666 (squares), and 2.928 (triangles) corresponding to the maximum, medium and minimum surface deformation in a cycle. The meridian plane is represented and the frame follows the volume centre of the capsule in the x_1-direction. (c) Three-dimensional representation of the capsule for the pulsatile flow (b) at different times.

of the capsule while moving way to the centreline of the tube. For amplitudes of the pulsatile flow larger than zero, the surface deformation acquires a quasi-periodic behaviour that oscillates about the response to the constant flow and with the same frequency as the imposed pulsatile flow. The area variation of the capsule in a pulsatile flow with the same capillarity number ($Ca = 0.15$), amplitude $\Delta v_m^\infty / v_{0m}^\infty = 1/3$ and various frequencies is shown in Fig. 4.21b. We observe the amplitude of the oscillations decay with the frequency because the capsule has less time to deform in each cycle. The surface deformation also depends on the relative stiffness of the capsule. That is illustrated in Fig. 4.21c where the surface deformations for three different capillarity number are depicted. The amplitude of the oscillation as well as the average value of $\Delta s/s_0$ increases with the capillarity. The capsule becomes relatively softer, it suffers a large elongation in the flow direction and a slightly reduction in the width direction (Fig 4.22). Moreover, a time delay between the surface deformation and the pulsatile flow is detected. This delay slightly increases for higher values capillarity number and the frequency. Hereinafter, we refer to the average value as the temporal moving average with a span of a cycle and it is useful to analyse the trend of the capsule.

Following, we analyse the motion of the capsule along the tube. The time evotuion of the radial trajectory of the centroid of the capsule is depicted in Fig. 4.23a. It is observed that the capsule asymptotically migrates to the centreline with oscillatory movement. It should be noted that this phenomenon does not happen in the case of a neutral buoyant solid sphere where the particle moves parallel to the tube-axis. The migration towards the centreline of the tube is due to the deformability of the capsule. This phenomenon has been numerically and experimentally reported by some authors [142, 164, 178–183]. Fig 4.23b shows the time evolution of the migration velocity of the capsule (defined as $v_{CR} = v_3^{vc} = -\frac{dr_C}{dt}$) in a pulsatile flow for three different amplitudes. After a short transient period, the migration velocity harmonically oscillates reducing monotonically the amplitude and the average value as the time evolves. Doddi and Bagchi [181] reported a quilitative similar behaviour for capsule in a constant Poiseuille flow. Zhu et al. [142] studied the motion of a deformable capsule in a sinusoidal shear flow near a wall. They found a quasi-periodic behaviour, but with a constant migration velocity in average term from the wall. The influence of the frequency of the pulse and the capillarity is illustrated in Figs. 4.23c and 4.23d, respectively. It can see that the softer the membrane is, the more the capsule is deformed and it rapidly migrates to the centreline. Furthermore, the amplitude of

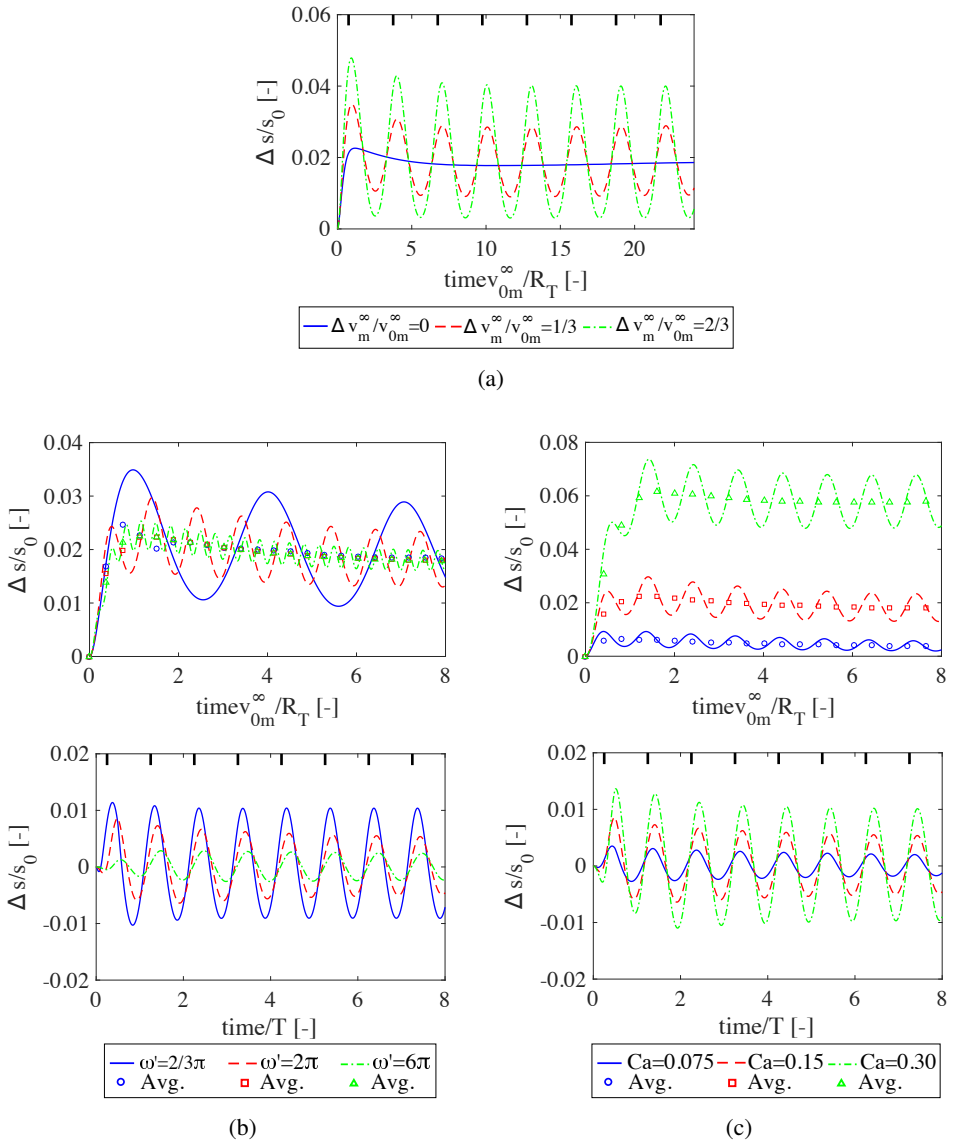

Figure 4.21: (a) Time evolution of the area variation of the capsule in pulsatile flow with $Ca = 0.15$, $\omega' = 2/3\pi$ and three different amplitudes; (b) in a pulsatile flow with amplitude $\Delta v_m^\infty / v_{0m}^\infty = 1/3$, $Ca = 0.15$, and various frequecies (top: as a function of the dimensionless time tv_{0m}^∞ / R_T; and bottom: as function of the dimensionless time t/T and substracting the average term); and (c) in a pulsatile flow with amplitude $\Delta v_m^\infty / v_{0m}^\infty = 1/3$, $\omega' = 2\pi$ and different capillarities (top: as a function of the dimensionless time tv_{0m}^∞ / R_T; and bottom: as a function of the dimensionless time t/T and substracting the average term). The vertical marks along the x-axis denote the maximum peaks of the pulsatile flow. The averaged is computed as a moving average with a span of a cycle.

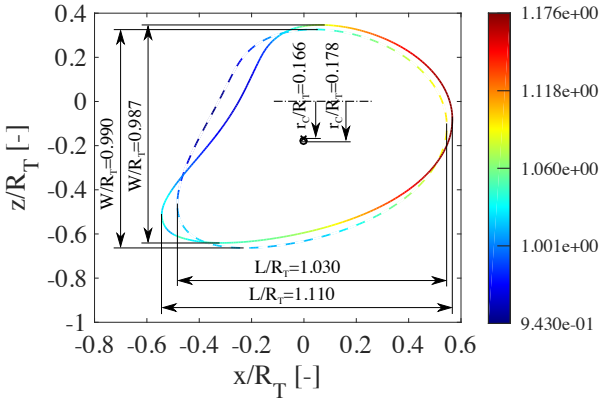

Figure 4.22: Surface dilation ($J_{s0} = \frac{ds}{ds_0}$) of a capsule in a pulsatile flow with amplitude $\Delta v_m^\infty / v_{0m}^\infty = 1/3$, frequency $\omega' = 2\pi$ and capilarity $Ca = 0.15$ (solid line) and $Ca = 0.30$ (dashed line) at the time $tv_{0m}^\infty / R_T = 3.750$. The circle and cross markers denote the centroid for $Ca = 0.15$ and $Ca = 0.30$,respectively.

the oscillations is slightly reduced with the frequency. The decay of the amplitude per cycle is more pronounced for lower frequencies because the migration velocity depends on the proximity to the centreline.

Fig. 4.24a shows the time evolution of the translational velocity ($v_{CH} = v_1^{vc}$) of the whole capsule in a pulsatile flow for various values of frequency and capillarity. On the right of the plot we have marked the theoretical value of the translational velocity for a neutral buoyant solid sphere in a Poiseuille flow placed at the centreline of the tube by the method of asymptotic expansion [184, 185]. The translation velocity starts from a non null velocity and its trend slowly increases in average term getting closer to the theoretical value as the capsule approximates to the centreline. We observe that the translational velocity is lower sensitive to the variation of the frequency and capillarity than the migration velocity. The influence of these parameter can be appreciated more clearly by the slip velocity defined as the difference of the horizontal velocity of the umperturbed flow at the position of the centroid of the capsule and the horizontal velocity of the capsule ($v_{CS} = (v_1^\infty(r = x_3^{vc}) - v_1^{vc})/v_{0m}^\infty$) (Fig. 4.24b). The slip velocity is always positive, that indicates the capsule moves behind the flow, and it trends to slowly decrease as the capsule approximates to the centreline. Moreover we observe a slight reduction of the slip velocity for higher values of the capillarity as it was also found by Doddi and Bagchi [181].

We observe that the membrane suffers a tank-treading effect due to the torque exercised by the flow on capsule. Fig. 4.25a depicts the distribution of the tangential

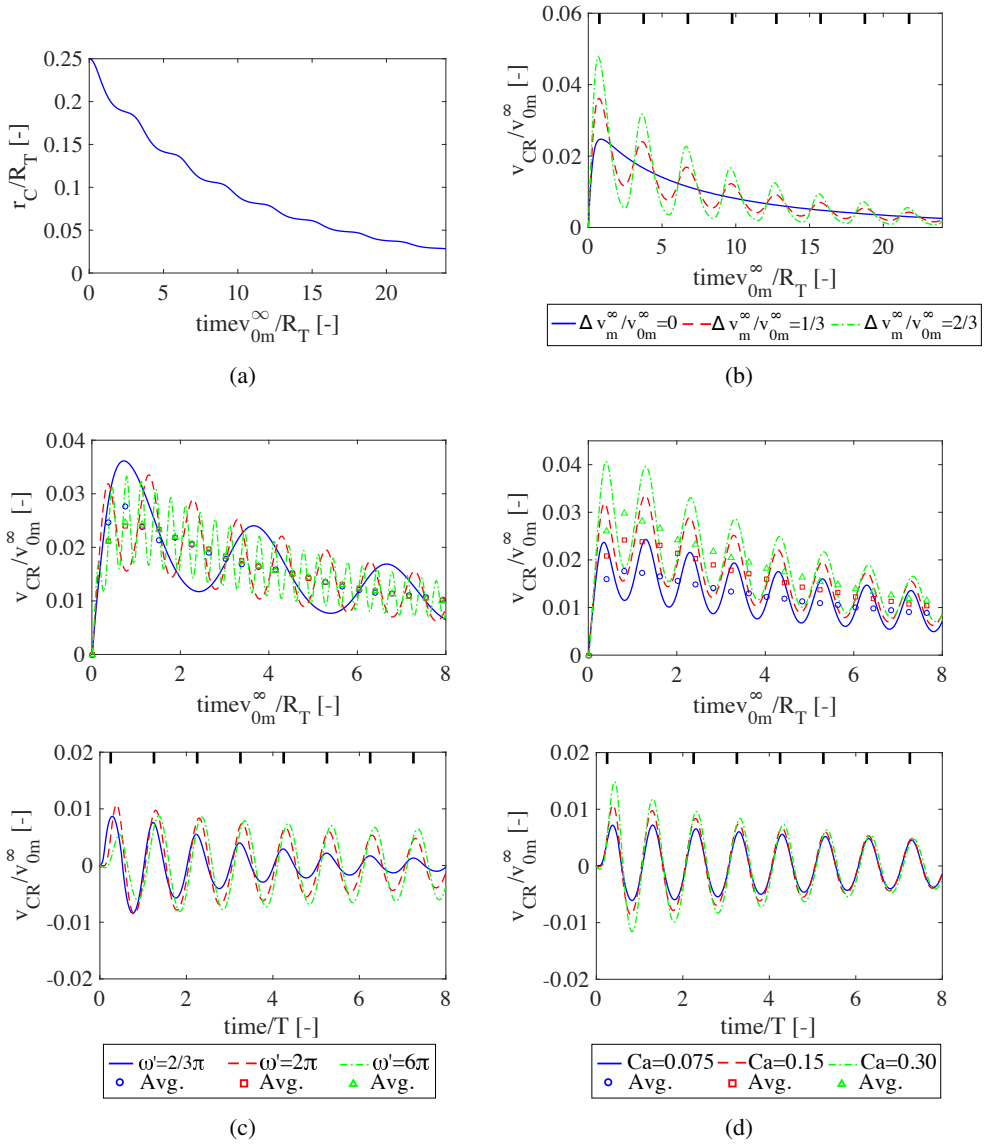

Figure 4.23: (a) Time evolution of the radial distance from the centreline of the tube to the centroid of the capsule (r_C/R_T) for a pulsatile flow with $Ca = 0.15$, $\omega' = 2/3\pi$ and $\Delta v_m^\infty/v_{0m}^\infty = 2/3$. (b) time evolution of the migration velocity of a capsule (defined as $v_{CR} = -\frac{dr_C}{dt}$) in pulsatile flow with $Ca = 0.15$, $\omega' = 2/3\pi$ and three different amplitudes; (c) in a pulsatile flow with amplitude $\Delta v_m^\infty/v_{0m}^\infty = 1/3$, capillarity $Ca = 0.15$ and three values of the frequency (top: as a function of the dimensionless time tv_{0m}^∞/R_T; and bottom: as a function of the dimensionless time t/T and substracting the average term); and (c) in a pulsatile flow with amplitude $\Delta v_m^\infty/v_{0m}^\infty = 1/3$, frequency $\omega' = 2\pi$ and different capillarities (top: as a function of the dimensionless time tv_{0m}^∞/R_T; and bottom: as a function of the dimensionless time t/T and substracting the average term). The vertical marks in the x-axis denote the maximum peaks of the pulsatile flow.

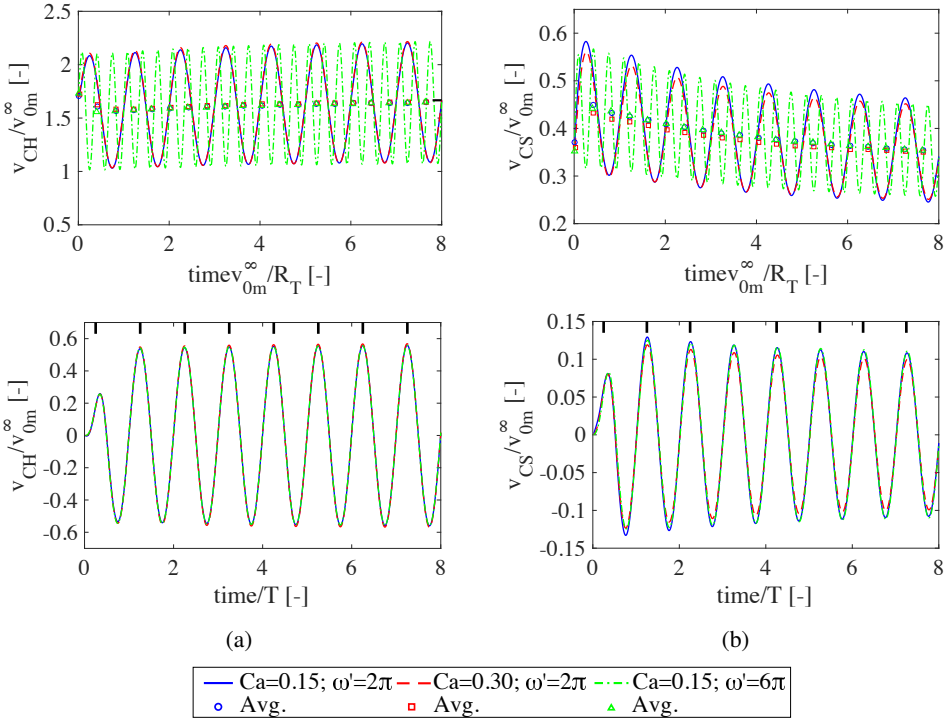

Figure 4.24: Time evolution of (a) the horizontal velocity and (b) the slip velocity of a capsule in a pulsating flow with a amplitude $\Delta v_m^\infty / v_{0m}^\infty = 1/3$, different frecuencies and capillarity numbers (top: as function of the dimensionless time tv_{0m}^∞ / R_T; and bottom: as fuction of the dimensionless time t/T and substracting the average term). The right mark on the y-axis denotes the theoretical translation of a neutral buoyant sphere placed in the centreline of a tube computed with a constant flow.

velocity (v_t) in the meridian plane of the membrane after subtracting the radial a horizontal velocity of the whole capsule. The membrane has a net tangential velocity in the clockwise direction that makes it rotate, although the direction is determined by the position of the capsule in the tube, this is, under the centreline or over it. Given the pulsatile character of the flow, the rotation exhibits also an oscillatory behaviour. This is illustrated in Fig. 4.25b where the mean tangential velocity on the membrane (v_{CT}) is shown. Initially, the mean tangential velocity is close to the theoretical value computed for a neutral buoyant solid sphere placed to a distance $r_C = 0.25 R_T$ from the centreline. The temporal average term asymptotically tends to decay with time as well as the oscillations. This is attributed to the migration of the capsule to the centreline. In fact, for softer capsules we find a larger reduction of the tank-treading

effect due to the faster migration process. In the limit case when the capsule reaches the centreline of the tube, the capsule will becomes axisymmetric and the tank-treading phenomenon will disappear.

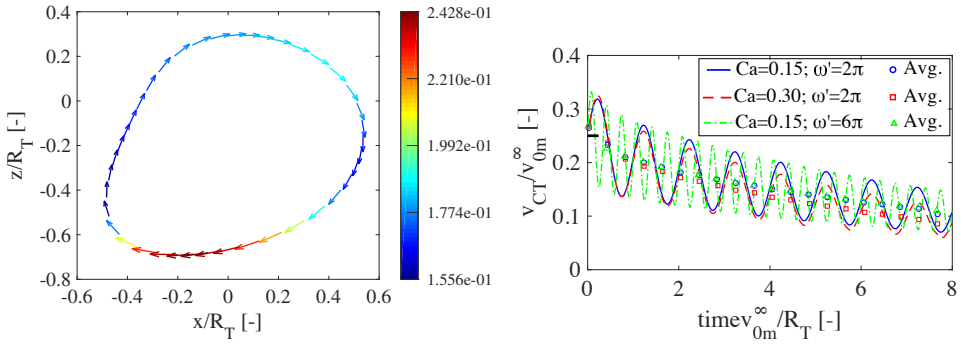

(a) (b)

Figure 4.25: (a) Tangential velocity distribution on the meridian plane of a capsule (v_t) in a pulsatile flow with $Ca = 0.15$, $\Delta v_m^\infty / v_{0m}^\infty = 1/3$ and $\omega' = 2\pi$ at time $tv_{0m}^\infty / R_T = 2.002$. (b) Time evolution of the mean tangential velocity on the meridian plane of a capsule (v_{CT}) in a pulsating flow for different frecuencies and capillarities. The left mark on the y-axis denotes the theoretical tangential velocity of a neutral buoyant sphere placed to a distance $r_C = 0.25 R_T$ from the centreline of a tube.

As it is known, the presence of the capsule in the tube causes an increase of the flow resistance that results in an additional pressure drop give by Δp^D. Note that this pressure drop is intimately related to the apparent viscosity through the Eq. 4.35. Lefebre and Barthès-Biesel [6] found that for an axisymmetric configuration with a constant flow, the additional pressure drop is influenced by the relative size and deformability of the capsule. They explained that the capsule is mainly elongated in the flow direction, which increases the surrounding viscosity film and consequently the additional pressure drop. In Fig. 4.26a we show the time evolution of the pressure drop for a pulsatile flow with different amplitudes. Similarly to the surface deformation, we observe an initial transient period with a fast increase of the additional pressure drop followed by quasi-periodic behaviour whose average term asymptotically evolves to a constant value as the capsule approaches the centreline. The time evolution of the additional pressure drop in a pulsating flow for different frequencies and capillarity is illustrated in Fig. 4.26b . The amplitude of the oscillations decreases with the frequency because the membrane has less time to deform in each cycle. Whereas for softer membranes a lower level of the additional pressure drop is observed. In this

case, the migration process is dominant. The capsule suffers a larger deformation and consequently migrates more rapidly to the centreline reducing the additional pressure drop as it is predicted by the theory of solid spheres in a tube. This effect is in consonance with the findings reported by Doddi and Bagchi [181] for deformable capsule in a Poiseuille flow.

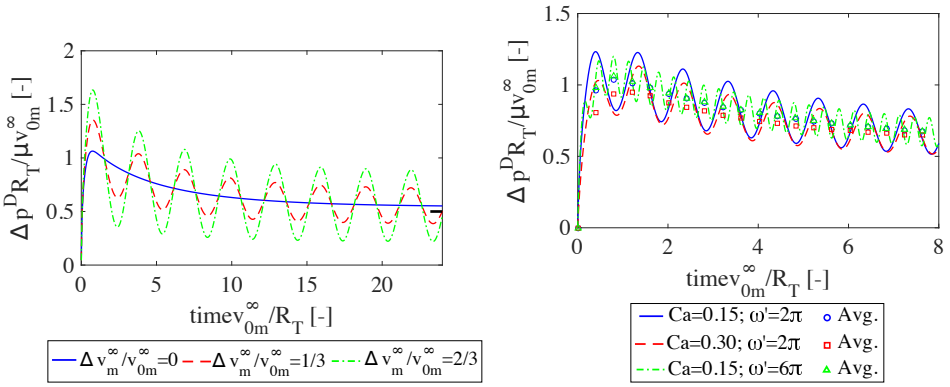

(a) (b)

Figure 4.26: (a) Time evolution of the disturbed pressure drop due to the presence of a capsule in a pulsatile flow with $Ca = 0.15$, $\omega' = 2/3\pi$ and three different amplitudes and (b) in a pulsatile flow with amplitude $\Delta v^\infty_m/v^\infty_{0m} = 1/3$, differente frequencies and capillarities. The right mark on the y-axis corresponds to the theoretical pressure drop for a neutral buoyant solid sphere placed in the centreline of the tube.

4.5 Conclusions

In this work we have presented a three dimensional isogeometric coupled BEM-FEM analysis in the time domain for the study of deformable capsules. The approach has been developed using the analysis suitable T-spline basis function. The T-spline bases provide a high order of approximation and continuity for both the geometry and physical variables. This continuity and smoothness of the bases are an important property since it confers stability and robustness to the method. Moreover, the high order of the bases provide a high differentiability needed for the accurate compute of the jump stress.

In the numerical examples we checked the spatial accuracy of the present approach analysing a constant flow passing a spheroid. We studied two different topological

discretizations: a structured mesh and an unstructured mesh. The structured mesh contains degenerated elements that are a source of numerical problems. We showed that applying a suitable treatment of degenerated elements both meshes properly converge with nearly the same order of accuracy. We also evaluated the temporal stability and accuracy of the method by simulating a deformable capsule in a shear flow. It was shown that numerical instabilities can appear in the capsule when degenerated elements are present and the membrane equilibrium is applied in strong form. The use of the variational principle helps to stabilize the method as well as reduces the continuity requirement of the basis functions. This linked with the application of an adaptive implicit temporal integration algorithm conforms a more robust approach. We compared our results with the literature and we found a good agreement for both the structured and unstructured mesh. However, this last mesh is advantageous since it does not contain degenerated elements and the aspect ratio of the elements is more homogeneous. In addition, exploiting the local h-refinement property of the T-spline, we showed the ability of the method to adapt dynamically the mesh of the capsule to the need of the specific problem. This technique is especially important for cases in which the membrane suffers large deformations along the time.

Finally we applied the method to the simulation of a deformable capsule in a tube with a pulsatile flow to show its potential use in complex biological flows. We showed the influence of the frequency of the pulse and the capillarity number in the evolution of the capsule and in consequence in the whole behaviour of the flow. We detect a tank treading effect of the membrane that decreases with the capillarity. Moreover, a migration of the capsule to the centreline of the tube is observed. This migration depends on the deformation of the capsule, so that the migration velocity increases with the capillarity whereas it is reduced slightly with the frequency. As the capsule tends to the centreline the additional flow resistance caused by the capsule decreases. This decrement in average term is more accused for higher values of the capillarity and amplitude of oscillations is slightly reduced with frequency.

UNIVERSITAT ROVIRA I VIRGILI
TOWARDS THE APPLICATION OF THE ISOGEOMETRIC BOUNDARY ELEMENT ANALYSIS TO FLUID MECHANICS:
NON-LINEAR GRAVITY WAVES AND DYNAMICS OF DEFORMABLE CAPSULES IN SHEAR FLOWS
Jorge Maestre Heredia

Chapter 5

Conclusions and future work

5.1 Conclusions

In this thesis an IGA-BEM analysis based on the NURBS and T-spline framework in the context of the Bézier extraction operation has been developed and implemented. Firstly, this approach was applied to the study of the propagation of non-linear gravity waves and the wave-structure interaction in the time domain. Then, the approach was extended for the analysis of deformable micro-capsules in shear flows considering the elastic properties of the membrane. The main conclusions can be summarized as follows:

- The T-spline and the NURBS technologies offer high level capabilities for complex geometric models that can be easily constructed with the aid of CAD systems. Invoking the IGA concept, these models can be imported directly into the engineering analysis softwares avoiding intermediate steps and preserving the exact geometry.
- The Bézier extraction operation provides a unified framework to incorporate the NURBS and T-spline discretization in the IGA, in a way similar to the standard finite element via modifying the basis functions.
- A spatial spectral convergence of the method has been demonstrated. Nevertheless, the presence of degenerated elements can affect to the convergence and a suitable treatment should be applied, as the Bézier transformation technique from degenerated to non-degenerated elements.

- The hight continuity of the basis functions gives stable and accurate results for large simulation times and under large movements and severe distortions of the mesh without the need of applying artificial smooth techniques, which typically are used in the standard formulation based on the Lagrange elements.
- The ability of the T-spline framework to manage unstructured meshes makes the approach robust because an homogeneous distribution of elements can be generated and the presence of degenerated elements can be avoided.
- Exploiting the local h-refinement of the T-spline framework, the quality of the mesh can be dynamically managed adapting efficiently to the requirements of the problem and keeping the accuracy during the simulation.
- The potential of the IGA has been revealed through the application of the present approach to solve problems of engineering interest as the generation of waves by a submerged moving foil and the dynamic movement of a deformable capsule in a pipe under a pulsating flow.

5.2 Future work

In this thesis we have shown the potential of the IGA-BEM based on the T-spline and NURBS for the study of two fluid dynamics problems, in which the boundary integral formulation can be applied. Since the introduction of the IGA, a great effort of the research community to develop more sophisticated geometric design techniques integrated with the engineering analysis tools has been carried out. In this direction, a recent line of investigation has appeared related with the formulation of the hierarchical spline family, this is, hierarchical B-splines, NURBS and T-splines [186–188]. This technology is based on a multilevel discretization of the physical space. Each level supposes an additional enrichment of the basis functions increasing the level of detail of the numerical analysis on the foundation of a fixed control mesh. This hierarchical technique allows the applications of high local refinements keeping the exact geometry and the smoothness. In addition, local coarsing processes can be applied by removing the levels of refinements and without the need of costly mesh operations. Therefore, the implementation of this technology can be seen as the next step to make a more advanced approach.

In the field of the wave-structure interaction, the formulation has been focused on the generation gravity waves by moving solid bodies and the propagation phenomenon.

However, some engineering applications are more aware on the structural design and integrity under hydrodynamic forces produced by the waves on the body. In this line, the present approach can be extended to take into account the deformability of the structure using a IGA-FEM model and coupling it with the IGA-BEM in a similar way as for the case of deformable capsules. Respect to this last application for deformable capsules, the membrane was considered to be a hyperelastic thin shell with negligible bending resistance. Although this model is in good agreement with the experiments, some processes as the buckling of the membrane cannot be properly reproduced. An example of the buckling is shown in the Fig. 5.1. The central region of the capsule is in compression and it generates the formation of folds. In this case, the length of folds depends on the mesh discretization and it does not inform about the bending rigidity of the membrane. Despite this unstable phenomenon, it is interesting note that the approach remains stable thanks to the smoothness of the basis functions and the inherent numerical bending resistance introduced by the FEM. A natural and straightforward extension of the present model can incorporate the effect of the small bending resistance of the membrane.

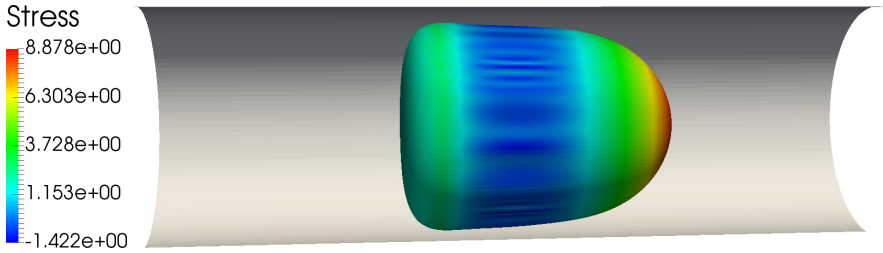

Figure 5.1: Steady shape of an initially spherical capsule of equivalent radius $R_C = 1R_T$ flowing in a cylindrical tube under a Poiseuille flow.

UNIVERSITAT ROVIRA I VIRGILI
TOWARDS THE APPLICATION OF THE ISOGEOMETRIC BOUNDARY ELEMENT ANALYSIS TO FLUID MECHANICS:
NON-LINEAR GRAVITY WAVES AND DYNAMICS OF DEFORMABLE CAPSULES IN SHEAR FLOWS
Jorge Maestre Heredia

Appendix A

Bézier surface

In this Appendix we introduce briefly the concepts of the Bézier surfaces since they are used in the formulation of the FE view of the T-spline and NURBS surfaces. For more details the reader is referred to [53].

A Bézier surface is a special case of a B-spline surface in which there is only one non-null knot span in each parametric directions, $\tilde{\boldsymbol{\xi}} = (\tilde{\xi}^1, \tilde{\xi}^2)$. The Bézier surface is defined by a set of control points, $\mathbf{Q}_{ij}$, with the corresponding weights, w^b_{ij}, and the bivariate Bernstein polynomials (or functions) $B_{ij,\mathbf{p}}(\tilde{\boldsymbol{\xi}})$ of degree $\mathbf{p} = (p_1, p_2)$, with $i = 1, 2, ...m^b_1 = p_1 + 1$ and $j = 1, 2, ...m^b_2 = p_2 + 1$. Then, the Bézier quadrilateral patch is represented as,

$$\mathbf{x}(\tilde{\boldsymbol{\xi}}) = \sum_{i=1}^{m_1}\sum_{j=1}^{m_2} \frac{w^b_{ij}\mathbf{Q}_{ij}B_{ij,\mathbf{p}}(\tilde{\boldsymbol{\xi}})}{\sum_{i=1}^{m_1}\sum_{j=1}^{m_2} w^b_{ij}B_{ij,\mathbf{p}}(\tilde{\boldsymbol{\xi}})} \qquad \tilde{\xi}^i \in [-1, 1] \tag{A.1}$$

The Bivariate Bernstein function are formed by a tensor product of univariate Bernstein functions, $B^i_{k,p_i}(\tilde{\xi}^i)$, as,

$$B_{ij,\mathbf{p}}(\tilde{\boldsymbol{\xi}}) = B^1_{i,p_1}(\tilde{\xi}^1)B^2_{j,p_2}(\tilde{\xi}^2) \tag{A.2}$$

in which the univariate Bernstein functions are defined as follows:

$$B^i_{k,p_i}(\tilde{\xi}^i) = \frac{1}{2^{p_i}}\binom{p_i}{k-1}(1+\tilde{\xi}^i)^{k-1}(1-\tilde{\xi}^i)^{p+1-k} \tag{A.3}$$

The univariate Bernstein functions, and by extension the bivariate basis, have several mathematical properties, the more important are:

- Partition unity: $\sum_{k=1}^{m_i} B^i_{k,p_i}(\tilde{\xi}^i) = 1$ for $\xi^i \in [-1, 1]$.
- Linear independence: $\sum_{k=1}^{m_i} c_k B^i_{k,p_i}(\tilde{\xi}^i) = 0$ if $c_k = 0$ for $\xi^i \in [-1, 1]$.
- Point-wise non-negativity: $B^i_{k,p_i}(\tilde{\xi}^i) \geq 0$ for $\xi^i \in [-1, 1]$.
- Symmetry: $B^i_{k,p_i}(\tilde{\xi}^i) = B^i_{k,p_i}(-\tilde{\xi}^i)$ for $\xi^i \in [-1, 1]$.
- Endpoint interpolation: $B^i_{k,p_i}(-1) = 1$

Fig A.1 shows an example of a cubic Bézier patch. Note that we have used a local index notation for each parametric direction, (i, j), however the above formulation can be expressed in global index by the mapping $A(i, j) = m_1(j - 1) + i$.

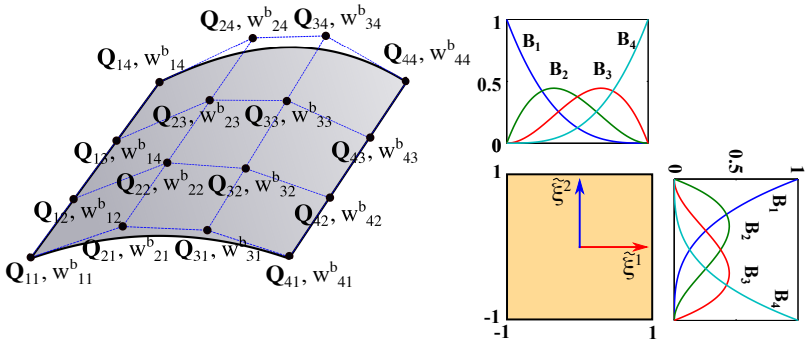

Figure A.1: Schematic illustration of a reactangular cubic Bézier patch.

An alternative way to express the Bézier patch is using the homogeneous coordinates. The advantage of this formulation is that allows applying the geometrical operations for non-rational bases to rational bases ($w^b \neq 1$). The idea consists in extend the Euclidean space, $\mathbf{Q}(x, y, x)$, to four dimensional space, $\mathbf{Q}^w = (w^b\mathbf{Q}, w^b)$. Then, the non-rational surface in four dimension is given by,

$$\mathbf{x}^w = (\mathbb{x}, \mathbb{y}, \mathbb{z}, \mathbb{w}) = \sum_{i,j=1}^{m_1,m_2} \mathbf{Q}^w_{ij,\mathbf{p}} B_{ij,\mathbf{p}}(\tilde{\boldsymbol{\xi}}) \tag{A.4}$$

While, the mapping to the Euclidean space is reverted as follows,

$$\mathbf{x} = (x, y, z) = \left(\frac{\mathbb{x}}{\mathbb{w}}, \frac{\mathbb{y}}{\mathbb{w}}, \frac{\mathbb{z}}{\mathbb{w}}\right) \tag{A.5}$$

Although the triangular Bézier patch is not very common, it is also used in this thesis. The formulation is similar to the standard quadrilateral patch and it can be expressed as,

$$\mathbf{x}(\tilde{\xi}^1, \tilde{\xi}^2, \tilde{\xi}^3) = \sum_{i+j+k=p+3} \mathbf{T}_{ijk} B_{ijk,p}(\tilde{\boldsymbol{\xi}}) \tag{A.6}$$

In Eq. A.6 the sub-indexes are defined by $\{i, j, k = 1, 2, ..., p+1 \mid i+j+k = p+3\}$, the parametric domain by $\{(\xi^1, \tilde{\xi}^2, \tilde{\xi}^3) \in [0, 1] \mid \tilde{\xi}^1 + \tilde{\xi}^2 + \tilde{\xi}^3 = 1\}$ and the triangular Bernstein functions are given by,

$$B_{ijk,p}(\tilde{\boldsymbol{\xi}}) = \binom{p}{i, j, k} (\tilde{\xi}^1)^{i-1} (\tilde{\xi}^2)^{j-1} (\tilde{\xi}^3)^{k-1} \tag{A.7}$$

UNIVERSITAT ROVIRA I VIRGILI
TOWARDS THE APPLICATION OF THE ISOGEOMETRIC BOUNDARY ELEMENT ANALYSIS TO FLUID MECHANICS:
NON-LINEAR GRAVITY WAVES AND DYNAMICS OF DEFORMABLE CAPSULES IN SHEAR FLOWS
Jorge Maestre Heredia

Appendix B

Transformation from degenerated Bézier element to non-degenerated elements

In Fig. B.1 a schematic illustration of the transformation process from the degenerated cubic quadrilateral Bézier patch to three non-degenerated cubic Bézier patches is shown.

Using the homogeneous coordinates representation, the transformation from the original degenerated quadrilateral Bézier patch to the triangular Bézier patch is given by,

$$
\begin{bmatrix} \mathbf{T}^w_{114} \\ \mathbf{T}^w_{213} \\ \mathbf{T}^w_{312} \\ \mathbf{T}^w_{411} \\ \mathbf{T}^w_{123} \\ \mathbf{T}^w_{222} \\ \mathbf{T}^w_{321} \\ \mathbf{T}^w_{132} \\ \mathbf{T}^w_{231} \\ \mathbf{T}^w_{141} \end{bmatrix} =
\begin{bmatrix} 1 & 0 & 0 & 0 & 0 & 0 & 0 & 0 \\ 0 & 1 & 0 & 0 & 0 & 0 & 0 & 0 \\ 0 & 0 & 1 & 0 & 0 & 0 & 0 & 0 \\ 0 & 0 & 0 & 1/4 & 0 & 0 & 0 & 1/4 \\ 0 & 0 & 0 & 0 & 1 & 0 & 0 & 0 \\ 0 & -1/4 & 0 & 0 & 0 & 3/4 & 0 & 0 \\ 0 & 0 & 0 & 0 & 0 & 0 & 0 & 0 \\ 0 & 0 & 0 & 0 & 0 & 0 & 0 & 0 \\ 0 & 0 & 0 & 0 & 0 & 0 & 0 & 0 \\ 0 & 0 & 0 & 0 & 0 & 0 & 0 & 0 \end{bmatrix}
\begin{bmatrix} 0 & 0 & 0 & 0 & 0 & 0 & 0 & 0 \\ 0 & 0 & 0 & 0 & 0 & 0 & 0 & 0 \\ 0 & 0 & 0 & 0 & 0 & 0 & 0 & 0 \\ 0 & 0 & 0 & 1/4 & 0 & 0 & 0 & 1/4 \\ 0 & 0 & 0 & 0 & 0 & 0 & 0 & 0 \\ 0 & 3/4 & 0 & 0 & 0 & -1/4 & 0 & 0 \\ 0 & 0 & 0 & 0 & 0 & 0 & 1 & 0 \\ 1 & 0 & 0 & 0 & 0 & 0 & 0 & 0 \\ 0 & 0 & 0 & 0 & 0 & 1 & 0 & 0 \\ 0 & 0 & 0 & 0 & 1 & 0 & 0 & 0 \end{bmatrix}
\begin{bmatrix} \mathbf{Q}^w_{11} \\ \mathbf{Q}^w_{21} \\ \mathbf{Q}^w_{31} \\ \mathbf{Q}^w_{41} \\ \mathbf{Q}^w_{12} \\ \mathbf{Q}^w_{22} \\ \mathbf{Q}^w_{32} \\ \mathbf{Q}^w_{42} \\ \mathbf{Q}^w_{13} \\ \mathbf{Q}^w_{23} \\ \mathbf{Q}^w_{33} \\ \mathbf{Q}^w_{43} \\ \mathbf{Q}^w_{14} \\ \mathbf{Q}^w_{24} \\ \mathbf{Q}^w_{34} \\ \mathbf{Q}^w_{44} \end{bmatrix}
\tag{B.1}
$$

In Eq. B.1 we have been assumed the degeneration is located in the right side of the quadrilateral Bézier patch. The transformation for other localization of the degenerated side is straightforward by applying a rotation to the conversion matrix.

The subdivision of the triangular Bézier patch in three quadrilateral patches depends on the choice of the points $\{\mathbf{D}_0, \mathbf{D}_1, \mathbf{D}_2, \mathbf{D}_3\}$ that define the domain of each quadrilateral patch (see Fig. B.1). In this work we locate the points $\{\mathbf{D}_1, \mathbf{D}_2, \mathbf{D}_3\}$ in the centre of each side of the triangular Bézier domain, and the internal point $\mathbf{D}_0$ in the barycentre. This usual configuration provides a well-balanced partition of the triangular Bézier patch. The computation of each quadrilateral partition is as follows [189]:

$$
\begin{bmatrix}
\widehat{\mathbf{Q}}^{w}_{1,11} \\ \widehat{\mathbf{Q}}^{w}_{1,21} \\ \widehat{\mathbf{Q}}^{w}_{1,31} \\ \widehat{\mathbf{Q}}^{w}_{1,41} \\ \widehat{\mathbf{Q}}^{w}_{1,12} \\ \widehat{\mathbf{Q}}^{w}_{1,22} \\ \widehat{\mathbf{Q}}^{w}_{1,32} \\ \widehat{\mathbf{Q}}^{w}_{1,42} \\ \widehat{\mathbf{Q}}^{w}_{1,13} \\ \widehat{\mathbf{Q}}^{w}_{1,23} \\ \widehat{\mathbf{Q}}^{w}_{1,33} \\ \widehat{\mathbf{Q}}^{w}_{1,43} \\ \widehat{\mathbf{Q}}^{w}_{1,14} \\ \widehat{\mathbf{Q}}^{w}_{1,24} \\ \widehat{\mathbf{Q}}^{w}_{1,34} \\ \widehat{\mathbf{Q}}^{w}_{1,44}
\end{bmatrix}
=
\begin{bmatrix}
1 & 0 & 0 & 0 & 0 & 0 \\
1/2 & 1/2 & 0 & 0 & 0 & 0 \\
1/4 & 1/2 & 1/4 & 0 & 0 & 0 \\
1/8 & 3/8 & 3/8 & 1/8 & 0 & 0 \\
1/2 & 0 & 0 & 0 & 1/2 & 0 \\
5/18 & 5/18 & 0 & 0 & 5/18 & 3/18 \\
11/72 & 22/72 & 11/72 & 0 & 11/72 & 14/72 \\
1/12 & 3/12 & 3/12 & 1/12 & 1/12 & 2/12 \\
1/4 & 0 & 0 & 0 & 2/4 & 0 \\
11/72 & 11/72 & 0 & 0 & 22/72 & 14/72 \\
5/54 & 10/54 & 5/54 & 0 & 10/54 & 13/54 \\
1/18 & 3/18 & 3/18 & 1/18 & 2/18 & 4/18 \\
1/8 & 0 & 0 & 0 & 3/8 & 0 \\
1/12 & 1/12 & 0 & 0 & 3/12 & 2/12 \\
1/18 & 2/18 & 1/18 & 0 & 3/18 & 4/18 \\
1/27 & 3/27 & 3/27 & 1/27 & 3/27 & 6/27
\end{bmatrix}
\begin{bmatrix}
0 & 0 & 0 & 0 \\
0 & 0 & 0 & 0 \\
0 & 0 & 0 & 0 \\
0 & 0 & 0 & 0 \\
0 & 0 & 0 & 0 \\
0 & 0 & 0 & 0 \\
3/72 & 0 & 0 & 0 \\
1/12 & 0 & 0 & 0 \\
0 & 1/4 & 0 & 0 \\
0 & 11/72 & 3/72 & 0 \\
3/54 & 5/54 & 3/54 & 0 \\
2/18 & 1/18 & 1/18 & 0 \\
0 & 3/8 & 0 & 1/8 \\
0 & 3/12 & 1/12 & 1/12 \\
1/18 & 3/18 & 2/18 & 1/18 \\
3/27 & 3/27 & 3/27 & 1/27
\end{bmatrix}
\begin{bmatrix}
\mathbf{T}^{w}_{114} \\ \mathbf{T}^{w}_{213} \\ \mathbf{T}^{w}_{312} \\ \mathbf{T}^{w}_{411} \\ \mathbf{T}^{w}_{123} \\ \mathbf{T}^{w}_{222} \\ \mathbf{T}^{w}_{321} \\ \mathbf{T}^{w}_{132} \\ \mathbf{T}^{w}_{231} \\ \mathbf{T}^{w}_{141}
\end{bmatrix}
\tag{B.2}
$$

and by permuting the indices $\mathbf{T}^{w}_{ijk}$ to $\mathbf{T}^{w}_{kij}$ and $\mathbf{T}^{w}_{jki}$, the homogeneous coordinates for the two other Bézier patches $\widehat{\mathbf{Q}}^{w}_{2}$ and $\widehat{\mathbf{Q}}^{w}_{3}$ can be obtained, respectively.

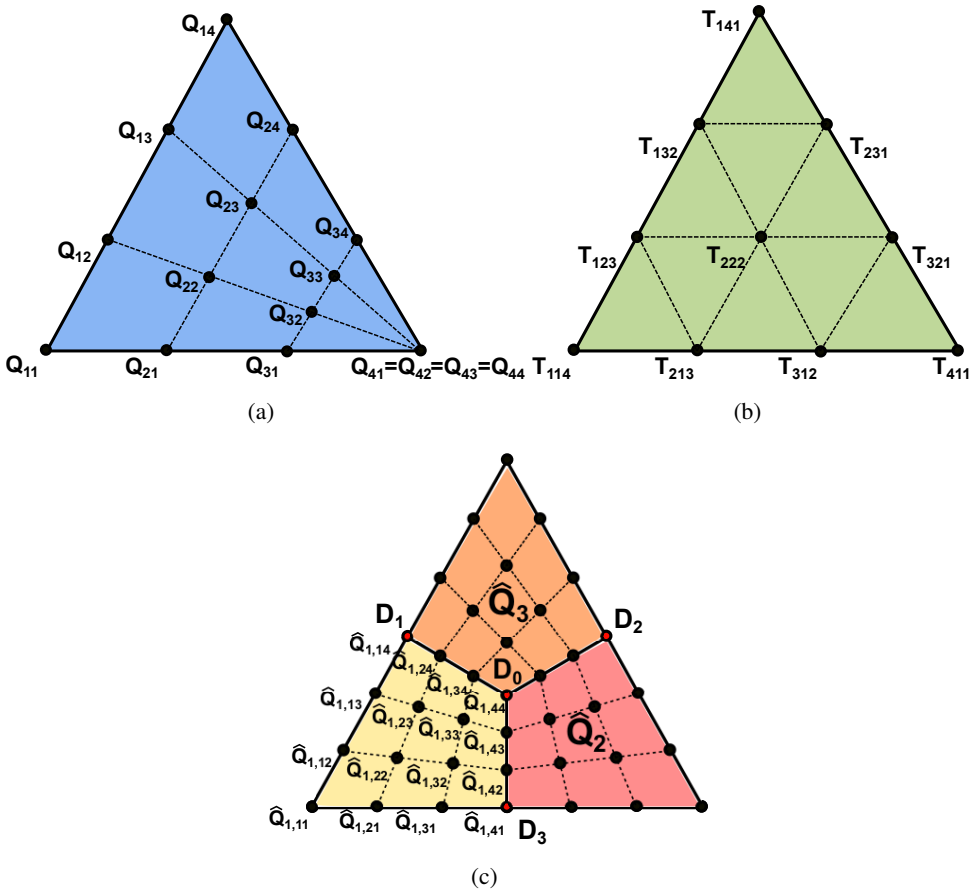

Figure B.1: (a) Degenerated cubic quadrilateral Bézier patch, (b) cubic triangular Bézier patch and (c) set of non-degenerated cubic quadrilateral Bézier patches.

Appendix C

Degenerated Bézier element transformation example data

Bézier control points

Table C.1 lists the Bézier control points of the example 2.6.

	Control points			
	x	y	z	w
1	0	0	0	1
2	$1/3$	0	0	1
3	$2/3$	0	0	1
4	1	0	0	1
5	$1/6$	$\sqrt{3}/6$	0	1
6	$7/18$	$\sqrt{3}/6$	0	1
7	$11/18$	$\sqrt{3}/6$	0	1
8	$5/6$	$\sqrt{3}/6$	0	1
9	$2/6$	$\sqrt{3}/3$	0	1
10	$8/18$	$\sqrt{3}/3$	0	1
11	$10/18$	$\sqrt{3}/3$	0	1
12	$4/6$	$\sqrt{3}/3$	0	1
13	$1/2$	$\sqrt{3}/2$	0	1
14	$1/2$	$\sqrt{3}/2$	0	1
15	$1/2$	$\sqrt{3}/2$	0	1
16	$1/2$	$\sqrt{3}/2$	0	1

Table C.1: Bézier control points relative to example 2.6

Subdivision operator

The subdivision matrices from the original Bézier element to three sub-elements, relative to the example 2.6, are as follows:

$$C_1^D = \left[\begin{matrix}
1.0000 & 0.0000 & 0.0000 & 0.0000 & 0.0000 & 0.0000 & 0.0000 & 0.0000 \\
0.5000 & 0.5000 & 0.0000 & 0.0000 & 0.0000 & 0.0000 & 0.0000 & 0.0000 \\
0.2500 & 0.5000 & 0.2500 & 0.0000 & 0.0000 & 0.0000 & 0.0000 & 0.0000 \\
0.1250 & 0.3750 & 0.3750 & 0.1250 & 0.0000 & 0.0000 & 0.0000 & 0.0000 \\
0.5000 & 0.0000 & 0.0000 & 0.0000 & 0.5000 & 0.0000 & 0.0000 & 0.0000 \\
0.2500 & 0.2500 & 0.0000 & 0.0000 & 0.2500 & 0.2500 & 0.0000 & 0.0000 \\
0.1250 & 0.2500 & 0.1250 & 0.0000 & 0.1250 & 0.2500 & 0.1250 & 0.0000 \\
0.0625 & 0.1875 & 0.1875 & 0.0625 & 0.0625 & 0.1875 & 0.1875 & 0.0625 \\
0.2500 & 0.0000 & 0.0000 & 0.0000 & 0.5000 & 0.0000 & 0.0000 & 0.0000 \\
0.1250 & 0.1250 & 0.0000 & 0.0000 & 0.2500 & 0.2500 & 0.0000 & 0.0000 \\
0.0625 & 0.1250 & 0.0625 & 0.0000 & 0.1250 & 0.2500 & 0.1250 & 0.0000 \\
0.0312 & 0.0938 & 0.0938 & 0.0312 & 0.0625 & 0.1875 & 0.1875 & 0.0625 \\
0.1250 & 0.0000 & 0.0000 & 0.0000 & 0.3750 & 0.0000 & 0.0000 & 0.0000 \\
0.0625 & 0.0625 & 0.0000 & 0.0000 & 0.1875 & 0.1875 & 0.0000 & 0.0000 \\
0.0312 & 0.0625 & 0.0312 & 0.0000 & 0.0938 & 0.1875 & 0.0938 & 0.0000 \\
0.0156 & 0.0469 & 0.0469 & 0.0156 & 0.0469 & 0.1406 & 0.1406 & 0.0469
\end{matrix}\right.$$

$$\left.\begin{matrix}
0.0000 & 0.0000 & 0.0000 & 0.0000 & 0.0000 & 0.0000 & 0.0000 & 0.0000 \\
0.0000 & 0.0000 & 0.0000 & 0.0000 & 0.0000 & 0.0000 & 0.0000 & 0.0000 \\
0.0000 & 0.0000 & 0.0000 & 0.0000 & 0.0000 & 0.0000 & 0.0000 & 0.0000 \\
0.0000 & 0.0000 & 0.0000 & 0.0000 & 0.0000 & 0.0000 & 0.0000 & 0.0000 \\
0.0000 & 0.0000 & 0.0000 & 0.0000 & 0.0000 & 0.0000 & 0.0000 & 0.0000 \\
0.0000 & 0.0000 & 0.0000 & 0.0000 & 0.0000 & 0.0000 & 0.0000 & 0.0000 \\
0.0000 & 0.0000 & 0.0000 & 0.0000 & 0.0000 & 0.0000 & 0.0000 & 0.0000 \\
0.0000 & 0.0000 & 0.0000 & 0.0000 & 0.0000 & 0.0000 & 0.0000 & 0.0000 \\
0.2500 & 0.0000 & 0.0000 & 0.0000 & 0.0000 & 0.0000 & 0.0000 & 0.0000 \\
0.1250 & 0.1250 & 0.0000 & 0.0000 & 0.0000 & 0.0000 & 0.0000 & 0.0000 \\
0.0625 & 0.1250 & 0.0625 & 0.0000 & 0.0000 & 0.0000 & 0.0000 & 0.0000 \\
0.0312 & 0.0938 & 0.0938 & 0.0312 & 0.0000 & 0.0000 & 0.0000 & 0.0000 \\
0.3750 & 0.0000 & 0.0000 & 0.0000 & 0.1250 & 0.0000 & 0.0000 & 0.0000 \\
0.1875 & 0.1875 & 0.0000 & 0.0000 & 0.0625 & 0.0625 & 0.0000 & 0.0000 \\
0.0938 & 0.1875 & 0.0938 & 0.0000 & 0.0312 & 0.0625 & 0.0312 & 0.0000 \\
0.0469 & 0.1406 & 0.1406 & 0.0469 & 0.0156 & 0.0469 & 0.0469 & 0.0156
\end{matrix}\right] \tag{C.1}$$

$$
C_2^D = \left[\begin{matrix}
0.1250 & 0.3750 & 0.3750 & 0.1250 & 0.0000 & 0.0000 & 0.0000 & 0.0000 \\
0.0000 & 0.2500 & 0.5000 & 0.2500 & 0.0000 & 0.0000 & 0.0000 & 0.0000 \\
0.0000 & 0.0000 & 0.5000 & 0.5000 & 0.0000 & 0.0000 & 0.0000 & 0.0000 \\
0.0000 & 0.0000 & 0.0000 & 1.0000 & 0.0000 & 0.0000 & 0.0000 & 0.0000 \\
0.0625 & 0.1875 & 0.1875 & 0.0625 & 0.0625 & 0.1875 & 0.1875 & 0.0625 \\
0.0000 & 0.1250 & 0.2500 & 0.1250 & 0.0000 & 0.1250 & 0.2500 & 0.1250 \\
0.0000 & 0.0000 & 0.2500 & 0.2500 & 0.0000 & 0.0000 & 0.2500 & 0.2500 \\
0.0000 & 0.0000 & 0.0000 & 0.5000 & 0.0000 & 0.0000 & 0.0000 & 0.5000 \\
0.0312 & 0.0938 & 0.0938 & 0.0312 & 0.0625 & 0.1875 & 0.1875 & 0.0625 \\
0.0000 & 0.0625 & 0.1250 & 0.0625 & 0.0000 & 0.1250 & 0.2500 & 0.1250 \\
0.0000 & 0.0000 & 0.1250 & 0.1250 & 0.0000 & 0.0000 & 0.2500 & 0.2500 \\
0.0000 & 0.0000 & 0.0000 & 0.2500 & 0.0000 & 0.0000 & 0.0000 & 0.5000 \\
0.0156 & 0.0469 & 0.0469 & 0.0156 & 0.0469 & 0.1406 & 0.1406 & 0.0469 \\
0.0000 & 0.0312 & 0.0625 & 0.0312 & 0.0000 & 0.0938 & 0.1875 & 0.0938 \\
0.0000 & 0.0000 & 0.0625 & 0.0625 & 0.0000 & 0.0000 & 0.1875 & 0.1875 \\
0.0000 & 0.0000 & 0.0000 & 0.1250 & 0.0000 & 0.0000 & 0.0000 & 0.3750
\end{matrix}\right.
$$

$$
\left.\begin{matrix}
0.0000 & 0.0000 & 0.0000 & 0.0000 & 0.0000 & 0.0000 & 0.0000 & 0.0000 \\
0.0000 & 0.0000 & 0.0000 & 0.0000 & 0.0000 & 0.0000 & 0.0000 & 0.0000 \\
0.0000 & 0.0000 & 0.0000 & 0.0000 & 0.0000 & 0.0000 & 0.0000 & 0.0000 \\
0.0000 & 0.0000 & 0.0000 & 0.0000 & 0.0000 & 0.0000 & 0.0000 & 0.0000 \\
0.0000 & 0.0000 & 0.0000 & 0.0000 & 0.0000 & 0.0000 & 0.0000 & 0.0000 \\
0.0000 & 0.0000 & 0.0000 & 0.0000 & 0.0000 & 0.0000 & 0.0000 & 0.0000 \\
0.0000 & 0.0000 & 0.0000 & 0.0000 & 0.0000 & 0.0000 & 0.0000 & 0.0000 \\
0.0000 & 0.0000 & 0.0000 & 0.0000 & 0.0000 & 0.0000 & 0.0000 & 0.0000 \\
0.0312 & 0.0938 & 0.0938 & 0.0312 & 0.0000 & 0.0000 & 0.0000 & 0.0000 \\
0.0000 & 0.0625 & 0.1250 & 0.0625 & 0.0000 & 0.0000 & 0.0000 & 0.0000 \\
0.0000 & 0.0000 & 0.1250 & 0.1250 & 0.0000 & 0.0000 & 0.0000 & 0.0000 \\
0.0000 & 0.0000 & 0.0000 & 0.2500 & 0.0000 & 0.0000 & 0.0000 & 0.0000 \\
0.0469 & 0.1406 & 0.1406 & 0.0469 & 0.0156 & 0.0469 & 0.0469 & 0.0156 \\
0.0000 & 0.0938 & 0.1875 & 0.0938 & 0.0000 & 0.0312 & 0.0625 & 0.0312 \\
0.0000 & 0.0000 & 0.1875 & 0.1875 & 0.0000 & 0.0000 & 0.0625 & 0.0625 \\
0.0000 & 0.0000 & 0.0000 & 0.3750 & 0.0000 & 0.0000 & 0.0000 & 0.1250
\end{matrix}\right] \tag{C.2}
$$

$$C_3^D = \left[\begin{matrix}
0.1250 & 0.0000 & 0.0000 & 0.0000 & 0.3750 & 0.0000 & 0.0000 & 0.0000 \\
0.0000 & 0.1250 & 0.0000 & 0.0000 & 0.0000 & 0.3750 & 0.0000 & 0.0000 \\
0.0000 & 0.0000 & 0.1250 & 0.0000 & 0.0000 & 0.0000 & 0.3750 & 0.0000 \\
0.0000 & 0.0000 & 0.0000 & 0.1250 & 0.0000 & 0.0000 & 0.0000 & 0.3750 \\
0.0000 & 0.0000 & 0.0000 & 0.0000 & 0.2500 & 0.0000 & 0.0000 & 0.0000 \\
0.0000 & 0.0000 & 0.0000 & 0.0000 & 0.0000 & 0.2500 & 0.0000 & 0.0000 \\
0.0000 & 0.0000 & 0.0000 & 0.0000 & 0.0000 & 0.0000 & 0.2500 & 0.0000 \\
0.0000 & 0.0000 & 0.0000 & 0.0000 & 0.0000 & 0.0000 & 0.0000 & 0.2500 \\
0.0000 & 0.0000 & 0.0000 & 0.0000 & 0.0000 & 0.0000 & 0.0000 & 0.0000 \\
0.0000 & 0.0000 & 0.0000 & 0.0000 & 0.0000 & 0.0000 & 0.0000 & 0.0000 \\
0.0000 & 0.0000 & 0.0000 & 0.0000 & 0.0000 & 0.0000 & 0.0000 & 0.0000 \\
0.0000 & 0.0000 & 0.0000 & 0.0000 & 0.0000 & 0.0000 & 0.0000 & 0.0000 \\
0.0000 & 0.0000 & 0.0000 & 0.0000 & 0.0000 & 0.0000 & 0.0000 & 0.0000 \\
0.0000 & 0.0000 & 0.0000 & 0.0000 & 0.0000 & 0.0000 & 0.0000 & 0.0000 \\
0.0000 & 0.0000 & 0.0000 & 0.0000 & 0.0000 & 0.0000 & 0.0000 & 0.0000 \\
0.0000 & 0.0000 & 0.0000 & 0.0000 & 0.0000 & 0.0000 & 0.0000 & 0.0000
\end{matrix}\right.$$

$$\left.\begin{matrix}
0.3750 & 0.0000 & 0.0000 & 0.0000 & 0.1250 & 0.0000 & 0.0000 & 0.0000 \\
0.0000 & 0.3750 & 0.0000 & 0.0000 & 0.0000 & 0.1250 & 0.0000 & 0.0000 \\
0.0000 & 0.0000 & 0.3750 & 0.0000 & 0.0000 & 0.0000 & 0.1250 & 0.0000 \\
0.0000 & 0.0000 & 0.0000 & 0.3750 & 0.0000 & 0.0000 & 0.0000 & 0.1250 \\
0.5000 & 0.0000 & 0.0000 & 0.0000 & 0.2500 & 0.0000 & 0.0000 & 0.0000 \\
0.0000 & 0.5000 & 0.0000 & 0.0000 & 0.0000 & 0.2500 & 0.0000 & 0.0000 \\
0.0000 & 0.0000 & 0.5000 & 0.0000 & 0.0000 & 0.0000 & 0.2500 & 0.0000 \\
0.0000 & 0.0000 & 0.0000 & 0.5000 & 0.0000 & 0.0000 & 0.0000 & 0.2500 \\
0.5000 & 0.0000 & 0.0000 & 0.0000 & 0.5000 & 0.0000 & 0.0000 & 0.0000 \\
0.0000 & 0.5000 & 0.0000 & 0.0000 & 0.0000 & 0.5000 & 0.0000 & 0.0000 \\
0.0000 & 0.0000 & 0.5000 & 0.0000 & 0.0000 & 0.0000 & 0.5000 & 0.0000 \\
0.0000 & 0.0000 & 0.0000 & 0.5000 & 0.0000 & 0.0000 & 0.0000 & 0.5000 \\
0.0000 & 0.0000 & 0.0000 & 0.0000 & 1.0000 & 0.0000 & 0.0000 & 0.0000 \\
0.0000 & 0.0000 & 0.0000 & 0.0000 & 0.0000 & 1.0000 & 0.0000 & 0.0000 \\
0.0000 & 0.0000 & 0.0000 & 0.0000 & 0.0000 & 0.0000 & 1.0000 & 0.0000 \\
0.0000 & 0.0000 & 0.0000 & 0.0000 & 0.0000 & 0.0000 & 0.0000 & 1.0000
\end{matrix}\right] \tag{C.3}$$

Transformation operator to non-degenerated elements

The transformation matrices from the degenerated Bézier element to three non-degenerated elements, relative to the example 2.6, are as follows:

$$C_1^{QQ} = \begin{bmatrix}
0.0000 & 0.0000 & 0.0000 & 1.0000 & 0.0000 & 0.0000 & 0.0000 & 0.0000 \\
0.0000 & 0.0000 & 0.0000 & 0.5000 & 0.0000 & 0.0000 & 0.0000 & 0.5000 \\
0.0000 & 0.0000 & 0.0000 & 0.2500 & 0.0000 & 0.0000 & 0.0000 & 0.5000 \\
0.0000 & 0.0000 & 0.0000 & 0.1250 & 0.0000 & 0.0000 & 0.0000 & 0.3750 \\
0.0000 & 0.0000 & 0.5000 & 0.5000 & 0.0000 & 0.0000 & 0.0000 & 0.0000 \\
0.0000 & 0.0000 & 0.2778 & 0.2778 & -0.0417 & 0.1250 & 0.1250 & 0.2361 \\
0.0000 & 0.0000 & 0.1528 & 0.1528 & -0.0486 & 0.1458 & 0.1458 & 0.2569 \\
0.0000 & 0.0000 & 0.0833 & 0.0833 & -0.0417 & 0.1250 & 0.1250 & 0.2083 \\
0.0000 & 0.2500 & 0.5000 & 0.2500 & 0.0000 & 0.0000 & 0.0000 & 0.0000 \\
0.0000 & 0.1528 & 0.3056 & 0.1528 & -0.0069 & 0.1458 & 0.1458 & 0.1042 \\
0.0000 & 0.0926 & 0.1852 & 0.0926 & -0.0046 & 0.1806 & 0.1806 & 0.1250 \\
0.0000 & 0.0556 & 0.1111 & 0.0556 & 0.0000 & 0.1667 & 0.1667 & 0.1111 \\
0.1250 & 0.3750 & 0.3750 & 0.1250 & 0.0000 & 0.0000 & 0.0000 & 0.0000 \\
0.0833 & 0.2500 & 0.2500 & 0.0833 & 0.0417 & 0.1250 & 0.1250 & 0.0417 \\
0.0556 & 0.1667 & 0.1667 & 0.0556 & 0.0556 & 0.1667 & 0.1667 & 0.0556 \\
0.0370 & 0.1111 & 0.1111 & 0.0370 & 0.0556 & 0.1667 & 0.1667 & 0.0556
\end{bmatrix}$$

$$\begin{bmatrix}
0.0000 & 0.0000 & 0.0000 & 0.0000 & 0.0000 & 0.0000 & 0.0000 & 0.0000 \\
0.0000 & 0.0000 & 0.0000 & 0.0000 & 0.0000 & 0.0000 & 0.0000 & 0.0000 \\
0.0000 & 0.0000 & 0.0000 & 0.2500 & 0.0000 & 0.0000 & 0.0000 & 0.0000 \\
0.0000 & 0.0000 & 0.0000 & 0.3750 & 0.0000 & 0.0000 & 0.0000 & 0.1250 \\
0.0000 & 0.0000 & 0.0000 & 0.0000 & 0.0000 & 0.0000 & 0.0000 & 0.0000 \\
0.0000 & 0.0000 & 0.0000 & 0.0000 & 0.0000 & 0.0000 & 0.0000 & 0.0000 \\
0.0417 & 0.0000 & 0.0000 & 0.1528 & 0.0000 & 0.0000 & 0.0000 & 0.0000 \\
0.0833 & 0.0000 & 0.0000 & 0.2500 & 0.0000 & 0.0000 & 0.0000 & 0.0833 \\
0.0000 & 0.0000 & 0.0000 & 0.0000 & 0.0000 & 0.0000 & 0.0000 & 0.0000 \\
0.0000 & 0.0000 & 0.0000 & 0.0000 & 0.0000 & 0.0000 & 0.0000 & 0.0000 \\
0.0556 & 0.0000 & 0.0000 & 0.0926 & 0.0000 & 0.0000 & 0.0000 & 0.0000 \\
0.1111 & 0.0000 & 0.0000 & 0.1667 & 0.0000 & 0.0000 & 0.0000 & 0.0556 \\
0.0000 & 0.0000 & 0.0000 & 0.0000 & 0.0000 & 0.0000 & 0.0000 & 0.0000 \\
0.0000 & 0.0000 & 0.0000 & 0.0000 & 0.0000 & 0.0000 & 0.0000 & 0.0000 \\
0.0556 & 0.0000 & 0.0000 & 0.0556 & 0.0000 & 0.0000 & 0.0000 & 0.0000 \\
0.1111 & 0.0000 & 0.0000 & 0.1111 & 0.0000 & 0.0000 & 0.0000 & 0.0370
\end{bmatrix} \tag{C.4}$$

$$C_2^{QQ} = \begin{bmatrix}
0.0000 & 0.0000 & 0.0000 & 0.0000 & 0.0000 & 0.0000 & 0.0000 & 0.0000 \\
0.0000 & 0.0000 & 0.0000 & 0.0000 & 0.0000 & 0.0000 & 0.0000 & 0.0000 \\
0.0000 & 0.0000 & 0.0000 & 0.0000 & 0.2500 & 0.0000 & 0.0000 & 0.0000 \\
0.1250 & 0.0000 & 0.0000 & 0.0000 & 0.3750 & 0.0000 & 0.0000 & 0.0000 \\
0.0000 & 0.0000 & 0.0000 & 0.0000 & 0.0000 & 0.0000 & 0.0000 & 0.0000 \\
0.0000 & 0.0000 & 0.0000 & 0.0000 & -0.0417 & 0.1250 & 0.1250 & -0.0417 \\
0.0000 & 0.0417 & 0.0000 & 0.0000 & 0.1042 & 0.1458 & 0.1458 & -0.0486 \\
0.0833 & 0.0833 & 0.0000 & 0.0000 & 0.2083 & 0.1250 & 0.1250 & -0.0417 \\
0.0000 & 0.0000 & 0.0000 & 0.0000 & 0.0000 & 0.0000 & 0.0000 & 0.2500 \\
0.0000 & 0.0000 & 0.0417 & 0.0000 & -0.0486 & 0.1458 & 0.1458 & 0.1042 \\
0.0000 & 0.0556 & 0.0556 & 0.0000 & 0.0324 & 0.1806 & 0.1806 & 0.0324 \\
0.0556 & 0.1111 & 0.0556 & 0.0000 & 0.1111 & 0.1667 & 0.1667 & 0.0000 \\
0.0000 & 0.0000 & 0.0000 & 0.1250 & 0.0000 & 0.0000 & 0.0000 & 0.3750 \\
0.0000 & 0.0000 & 0.0833 & 0.0833 & -0.0417 & 0.1250 & 0.1250 & 0.2083 \\
0.0000 & 0.0556 & 0.1111 & 0.0556 & 0.0000 & 0.1667 & 0.1667 & 0.1111 \\
0.0370 & 0.1111 & 0.1111 & 0.0370 & 0.0556 & 0.1667 & 0.1667 & 0.0556
\end{bmatrix}$$

$$\begin{bmatrix}
0.0000 & 0.0000 & 0.0000 & 0.0000 & 0.0000 & 0.0000 & 0.0000 & 1.0000 \\
0.5000 & 0.0000 & 0.0000 & 0.0000 & 0.0000 & 0.0000 & 0.0000 & 0.5000 \\
0.5000 & 0.0000 & 0.0000 & 0.0000 & 0.0000 & 0.0000 & 0.0000 & 0.2500 \\
0.3750 & 0.0000 & 0.0000 & 0.0000 & 0.0000 & 0.0000 & 0.0000 & 0.1250 \\
0.0000 & 0.0000 & 0.0000 & 0.5000 & 0.0000 & 0.0000 & 0.0000 & 0.5000 \\
0.2778 & 0.0000 & 0.0000 & 0.2778 & 0.0000 & 0.0000 & 0.0000 & 0.2778 \\
0.3056 & 0.0000 & 0.0000 & 0.1528 & 0.0000 & 0.0000 & 0.0000 & 0.1528 \\
0.2500 & 0.0000 & 0.0000 & 0.0833 & 0.0000 & 0.0000 & 0.0000 & 0.0833 \\
0.0000 & 0.0000 & 0.0000 & 0.5000 & 0.0000 & 0.0000 & 0.0000 & 0.2500 \\
0.1528 & 0.0000 & 0.0000 & 0.3056 & 0.0000 & 0.0000 & 0.0000 & 0.1528 \\
0.1852 & 0.0000 & 0.0000 & 0.1852 & 0.0000 & 0.0000 & 0.0000 & 0.0926 \\
0.1667 & 0.0000 & 0.0000 & 0.1111 & 0.0000 & 0.0000 & 0.0000 & 0.0556 \\
0.0000 & 0.0000 & 0.0000 & 0.3750 & 0.0000 & 0.0000 & 0.0000 & 0.1250 \\
0.0833 & 0.0000 & 0.0000 & 0.2500 & 0.0000 & 0.0000 & 0.0000 & 0.0833 \\
0.1111 & 0.0000 & 0.0000 & 0.1667 & 0.0000 & 0.0000 & 0.0000 & 0.0556 \\
0.1111 & 0.0000 & 0.0000 & 0.1111 & 0.0000 & 0.0000 & 0.0000 & 0.0370
\end{bmatrix} \tag{C.5}$$

$$
C_3^{QQ} = \left[\begin{matrix}
1.0000 & 0.0000 & 0.0000 & 0.0000 & 0.0000 & 0.0000 & 0.0000 & 0.0000 \\
0.5000 & 0.5000 & 0.0000 & 0.0000 & 0.0000 & 0.0000 & 0.0000 & 0.0000 \\
0.2500 & 0.5000 & 0.2500 & 0.0000 & 0.0000 & 0.0000 & 0.0000 & 0.0000 \\
0.1250 & 0.3750 & 0.3750 & 0.1250 & 0.0000 & 0.0000 & 0.0000 & 0.0000 \\
0.5000 & 0.0000 & 0.0000 & 0.0000 & 0.5000 & 0.0000 & 0.0000 & 0.0000 \\
0.2778 & 0.2778 & 0.0000 & 0.0000 & 0.2361 & 0.1250 & 0.1250 & -0.0417 \\
0.1528 & 0.3056 & 0.1528 & 0.0000 & 0.1042 & 0.1458 & 0.1458 & -0.0069 \\
0.0833 & 0.2500 & 0.2500 & 0.0833 & 0.0417 & 0.1250 & 0.1250 & 0.0417 \\
0.2500 & 0.0000 & 0.0000 & 0.0000 & 0.5000 & 0.0000 & 0.0000 & 0.0000 \\
0.1528 & 0.1528 & 0.0000 & 0.0000 & 0.2569 & 0.1458 & 0.1458 & -0.0486 \\
0.0926 & 0.1852 & 0.0926 & 0.0000 & 0.1250 & 0.1806 & 0.1806 & -0.0046 \\
0.0556 & 0.1667 & 0.1667 & 0.0556 & 0.0556 & 0.1667 & 0.1667 & 0.0556 \\
0.1250 & 0.0000 & 0.0000 & 0.0000 & 0.3750 & 0.0000 & 0.0000 & 0.0000 \\
0.0833 & 0.0833 & 0.0000 & 0.0000 & 0.2083 & 0.1250 & 0.1250 & -0.0417 \\
0.0556 & 0.1111 & 0.0556 & 0.0000 & 0.1111 & 0.1667 & 0.1667 & 0.0000 \\
0.0370 & 0.1111 & 0.1111 & 0.0370 & 0.0556 & 0.1667 & 0.1667 & 0.0556
\end{matrix}\right.
$$

$$
\left.\begin{matrix}
0.0000 & 0.0000 & 0.0000 & 0.0000 & 0.0000 & 0.0000 & 0.0000 & 0.0000 \\
0.0000 & 0.0000 & 0.0000 & 0.0000 & 0.0000 & 0.0000 & 0.0000 & 0.0000 \\
0.0000 & 0.0000 & 0.0000 & 0.0000 & 0.0000 & 0.0000 & 0.0000 & 0.0000 \\
0.0000 & 0.0000 & 0.0000 & 0.0000 & 0.0000 & 0.0000 & 0.0000 & 0.0000 \\
0.0000 & 0.0000 & 0.0000 & 0.0000 & 0.0000 & 0.0000 & 0.0000 & 0.0000 \\
0.0000 & 0.0000 & 0.0000 & 0.0000 & 0.0000 & 0.0000 & 0.0000 & 0.0000 \\
0.0000 & 0.0000 & 0.0000 & 0.0000 & 0.0000 & 0.0000 & 0.0000 & 0.0000 \\
0.0000 & 0.0000 & 0.0000 & 0.0000 & 0.0000 & 0.0000 & 0.0000 & 0.0000 \\
0.2500 & 0.0000 & 0.0000 & 0.0000 & 0.0000 & 0.0000 & 0.0000 & 0.0000 \\
0.1528 & 0.0000 & 0.0000 & 0.0417 & 0.0000 & 0.0000 & 0.0000 & 0.0000 \\
0.0926 & 0.0000 & 0.0000 & 0.0556 & 0.0000 & 0.0000 & 0.0000 & 0.0000 \\
0.0556 & 0.0000 & 0.0000 & 0.0556 & 0.0000 & 0.0000 & 0.0000 & 0.0000 \\
0.3750 & 0.0000 & 0.0000 & 0.0000 & 0.0000 & 0.0000 & 0.0000 & 0.1250 \\
0.2500 & 0.0000 & 0.0000 & 0.0833 & 0.0000 & 0.0000 & 0.0000 & 0.0833 \\
0.1667 & 0.0000 & 0.0000 & 0.1111 & 0.0000 & 0.0000 & 0.0000 & 0.0556 \\
0.1111 & 0.0000 & 0.0000 & 0.1111 & 0.0000 & 0.0000 & 0.0000 & 0.0370
\end{matrix}\right] \tag{C.6}
$$

UNIVERSITAT ROVIRA I VIRGILI
TOWARDS THE APPLICATION OF THE ISOGEOMETRIC BOUNDARY ELEMENT ANALYSIS TO FLUID MECHANICS:
NON-LINEAR GRAVITY WAVES AND DYNAMICS OF DEFORMABLE CAPSULES IN SHEAR FLOWS
Jorge Maestre Heredia

Bibliography

[1] S. T. Grilli, I. A. Svendsen, R. Subramanya, Breaking criterion and characteristics for solitary waves on slopes, Journal of Waterway, Port, Coastal and Ocean Engineering 123 (3) (1997) 102–112.

[2] M. Chern, A. Borthwick, R. Taylor, Simulation of non-linear free surface motions in a cylindrical domain using a Chebyshev-Fourier spectral collocation method, International Journal for Numerical Methods in Fluids 36 (4) (2001) 465–496.

[3] P. Ferrant, A coupled time and frequency approach for nonlinear wave radiation, In Eighteenth Symposium on Naval Hydrodynamics (1991) 67–83.

[4] E. Lac, D. Barthès-Biesel, N. Pelekasis, J. Tsamopoulos, Spherical capsules in three-dimensional unbounded Stokes flows: effect of the membrane constitutive law and onset of buckling, Journal of Fluid Mechanics 516 (2004) 303–334.

[5] J. Walter, A.-V. Salsac, D. Barthès-Biesel, P. Le Tallec, Coupling of finite element and boundary integral methods for a capsule in a Stokes flow, International journal for numerical methods in engineering 83 (7) (2010) 829–850.

[6] Y. Lefebvre, D. Barthès-Biesel, Motion of a capsule in a cylindrical tube: effect of membrane pre-stress, Journal of Fluid Mechanics 589 (2007) 157–181.

[7] T. Hughes, J. Cottrell, Y. Bazilevs, Isogeometric analysis: CAD, finite elements, NURBS, exact geometry and mesh refinement, Computer Methods in Applied Mechanics and Engineering 194 (39–41) (2005) 4135–4195.

[8] T. Hughes, Isogeometric analysis: Progress and Challenges, in: Conference on Mathematical Methods for Curves & Surfaces (MMCS'08), Conference on Mathematical Methods for Curves & Surfaces (MMCS'08), 2008, p. .

[9] J. Cottrell, T. Hughes, A. Reali, Studies of refinement and continuity in isogeometric structural analysis, Computer Methods in Applied Mechanics and Engineering 196 (41-44) (2007) 4160–4183.

[10] J. Cottrell, T. Hughes, Y. Bazilevs, Isogeometric Analysis: Toward Integration of CAD and FEA, John Wiley & Sons, 2009.

[11] C. Politis, A. Ginnis, P. Kaklis, K. Belibassakis, C. Feurer, An isogeometric BEM for exterior potential-flow problems in the plane, Joint Conference on Geometric and Physical Modeling (2009) 349–354.

[12] R. Simpson, S. Bordas, J. Trevelyan, T. Rabczuk, A two-dimensional Isogeometric Boundary Element Method for elastostatic analysis, Computer Methods in Applied Mechanics and Engineering 209-212 (2012) 87–100.

[13] M. Peake, J. Trevelyan, G. Coates, Extended isogeometric boundary element method (XIBEM) for two-dimensional Helmholtz problems, Computer Methods in Applied Mechanics and Engineering 259 (2013) 93–102.

[14] M. Peake, J. Trevelyan, G. Coates, Extended isogeometric boundary element method (XIBEM) for three-dimensional medium-wave acoustic scattering problems, Computer Methods in Applied Mechanics and Engineering 284 (2015) 762–780.

[15] C. Politis, A. Papagiannopoulos, K. Belibassakis, P. Kaklis, K. Kostas, A. Ginnis, T. Gerostathis, An isogeometric BEM for exterior potential-flow problems around lifting bodies, in: 11th World Congress on Computational Mechanics (WCCM XI), 2014, pp. 2433–2444.

[16] A. Aimi, M. Diligenti, M. Sampoli, A. Sestini, Isogemetric analysis and symmetric Galerkin BEM: A 2D numerical study, Applied Mathematics and Computation 272 (2016) 173–186.

[17] A. Ginnis, K. Kostas, C. Feurer, K. Belibassakis, P. Gerostathis, C. Politis, P. Kaklis, A CATIA® ship-parametric model for isogeometric hull optimization with respect to wave resistance, Proc. 15th International Conference on Computer Applications on Shipbuilding, ICCAS 2011.

[18] K. Belibassakis, T. Gerostathis, K. Kostas, C. Politis, P. Kaklis, A. Ginnis, C. Feurer, A BEM-isogeometric method for the ship wave-resistance problem, Ocean Engineering 60 (2013) 53–67.

[19] L. Heltai, M. Arroyo, A. DeSimone, Nonsingular isogeometric boundary element method for Stokes flows in 3D, Computer Methods in Applied Mechanics and Engineering 268 (2014) 514–539.

[20] T. Sederberg, J. Zheng, A. Bakenov, A. Nasri, T-splines and T-NURCCs, ACM Transactions on Graphics 22 (3) (2003) 477–484.

[21] M. Scott, X. Li, T. Sederberg, T. Hughes, Local refinement of analysis-suitable T-splines, Computer Methods in Applied Mechanics and Engineering 213 (2012) 206–222.

[22] X. Li, J. Zheng, T. W. Sederberg, T. J. Hughes, M. A. Scott, On linear independence of T-spline blending functions, Computer Aided Geometric Design 29 (1) (2012) 63–76.

[23] M. Borden, M. Scott, J. Evans, T. Hughes, Isogeometric finite element data structures based on Bézier extraction of NURBS, International Journal for Numerical Methods in Engineering 87 (1-5) (2011) 15–47.

[24] M. Scott, R. Simpson, J. Evans, S. Lipton, S. Bordas, T. Hughes, T. Sederberg, Isogeometric boundary element analysis using unstructured T-splines, Computer Methods in Applied Mechanics and Engineering 254rr (0) (2013) 197–221.

[25] D. Thomas, M. Scott, J. Evans, K. Tew, E. Evans, Bézier projection: A unified approach for local projection and quadrature-free refinement and coarsening of NURBS and T-splines with particular application to isogeometric design and analysis, Computer Methods in Applied Mechanics and Engineering 284 (2015) 55–105.

[26] D. Benson, Y. Bazilevs, M.-C. Hsu, T. Hughes, A large deformation, rotation-free, isogeometric shell, Computer Methods in Applied Mechanics and Engineering 200 (13-16) (2011) 1367–1378.

[27] C. Verhoosel, M. Scott, T. Hughes, R. de Borst, An isogeometric analysis approach to gradient damage models, International Journal for Numerical Methods in Engineering 86 (1) (2011) 115–134.

[28] C. Verhoosel, M. Scott, R. De Borst, T. Hughes, An isogeometric approach to cohesive zone modeling, International Journal for Numerical Methods in Engineering 87 (1-5) (2011) 336–360.

[29] D. Schillinger, L. Dedè, M. Scott, J. Evans, M. Borden, E. Rank, T. Hughes, An isogeometric design-through-analysis methodology based on adaptive hierarchical refinement of NURBS, immersed boundary methods, and T-spline CAD surfaces, Computer Methods in Applied Mechanics and Engineering 249-252 (2012) 116–150.

[30] Z. Kacprzyk, K. Ostapska-Luczkowska, Isogeometric analysis as a new FEM formulation-simple problems of steady state thermal analysis, Procedia Engineering 91 (2014) 87–92.

[31] R. Simpson, M. Scott, M. Taus, D. Thomas, H. Lian, Acoustic isogeometric boundary element analysis, Computer Methods in Applied Mechanics and Engineering 269 (2014) 265–290.

[32] A. Ginnis, K. Kostas, C. Politis, P. Kaklis, K. Belibassakis, T. Gerostathis, M. Scott, T. Hughes, Isogeometric boundary-element analysis for the wave-resistance problem using T-splines, Computer Methods in Applied Mechanics and Engineering 279 (0) (2014) 425–439.

[33] K. Kostas, A. Ginnis, C. Politis, P. Kaklis, Ship-hull shape optimization with a T-spline based BEM-isogeometric solver, Computer Methods in Applied Mechanics and Engineering 284 (2015) 611–622.

[34] V. Nguyen, C. Anitescu, S. Bordas, T. Rabczuk, Isogeometric analysis: An overview and computer implementation aspects, Mathematics and Computers in Simulation 117 (2015) 89–116.

[35] C. Pozrikidis, Finite deformation of liquid capsules enclosed by elastic membranes in simple shear flow, Journal of Fluid Mechanics 297 (1995) 123–152.

[36] S. Ramanujan, C. Pozrikidis, Deformation of liquid capsules enclosed by elastic membranes in simple shear flow: large deformations and the effect of fluid viscosities, Journal of Fluid Mechanics 361 (1998) 117–143.

[37] Y. Wang, P. Dimitrakopoulos, A three-dimensional spectral boundary element algorithm for interfacial dynamics in Stokes flow, Physics of Fluids (1994-present) 18 (8) (2006) 082106.

[38] A. Mola, L. Heltai, A. DeSimone, A stable and adaptive semi-Lagrangian potential model for unsteady and nonlinear ship-wave interactions, Engineering Analysis with Boundary Elements 37 (1) (2013) 128–143.

[39] S. Lipton, J. Evans, Y. Bazilevs, T. Elguedj, T. Hughes, Robustness of isogeometric structural discretizations under severe mesh distortion, Computer Methods in Applied Mechanics and Engineering 199 (5–8) (2010) 357–373.

[40] A. Abbasnia, M. Ghiasi, A fully nonlinear wave interaction with an array of submerged cylinders by nurbs numerical wave tank and acceleration potential, Ships and Offshore Structures 9 (4) (2014) 404–417.

[41] C. C. Lee, Y. H. Liu, C. H. Kim, Simulation of Nonlinear Waves And Forces Due to Transient And Steady Motion of Submerged Sphere, International Journal of Offshore and Polar Engineering 416 (1994) 174–182.

[42] S. T. Grilli, P. Guyenne, F. Dias, A fully non-linear model for three-dimensional overturning waves over an arbitrary bottom, International Journal for Numerical Methods in Fluids 35 (7) (2001) 829–867.

[43] P. Guyenne, S. T. Grilli, Numerical study of three-dimensional overturning waves in shallow water, Journal of Fluid Mechanics 547 (2006) 361–388.

[44] W. Bai, R. Eatock Taylor, Higher-order boundary element simulation of fully nonlinear wave radiation by oscillating vertical cylinders, Applied Ocean Research 28 (4) (2006) 247–265.

[45] W. Bai, R. E. Taylor, Fully nonlinear simulation of wave interaction with fixed and floating flared structures, Ocean Engineering 36 (3–4) (2009) 223–236.

[46] E. Guerber, M. Benoit, S. T. Grilli, C. Buvat, A fully nonlinear implicit model for wave interactions with submerged structures in forced or free motion, Engineering Analysis with Boundary Elements 36 (2012) 1151–1163.

[47] M. Hannan, W. Bai, K. Ang, Modeling of fully nonlinear wave radiation by submerged moving structures using the higher order boundary element method, Journal of Marine Science and Application 13 (1) (2014) 1–10.

[48] E. Dombre, M. Benoit, D. Violeau, C. Peyrard, S. T. Grilli, Simulation of floating structure dynamics in waves by implicit coupling of a fully non-linear potential flow model and a rigid body motion approach, Journal of Ocean Engineering and Marine Energy 1 (1) (2014) 55–76.

[49] D. G. Dommermuth, D. K. P. Yue, W. M. Lin, R. J. Rapp, E. S. Chan, W. K. Melville, Deep-water plunging breakers: a comparison between potential theory and experiments, Journal of Fluid Mechanics 189 (1988) 423–442.

[50] A. Goumilevski, J. Cheng, G. L. Chahine, Wave breaking on a sloping beach: comparisons between experiments and simulations, in: Proc. 14th ASCE Engr. Mech. Conf., Austin, TX, 2000, p. .

[51] J. Harris, E. Dombre, M. Benoit, S. Grilli, A comparison of methods in fully nonlinear boundary element numerical wave tank development, in: 14émes Journées de l'Hydrodynamique, 2014, p. .

[52] Autodesk, T-splines, Inc, http://www.tsplines.com.

[53] L. Piegls, W. Tiller, The NURBS Book, 2nd Edition, Springer, 1996.

[54] M. A. Scott, T-splines as a design-through-analysis technology, Ph.D. thesis, The University of Texas at Austin (2011).

[55] Y. Bazilevs, V. Calo, J. Cottrell, J. Evans, T. Hughes, S. Lipton, M. Scott, T. Sederberg, Isogeometric analysis using T-splines, Computer Methods in Applied Mechanics and Engineering 199 (5-8) (2010) 229–263.

[56] X. Li, M. A. Scott, Analysis-suitable T-splines: characterization, refineability, and approximation, Mathematical Models and Methods in Applied Sciences 24 (06) (2014) 1141–1164.

[57] M. Scott, M. Borden, C. Verhoosel, T. Sederberg, T. Hughes, Isogeometric finite element data structures based on Bézier extraction of T-splines, International Journal for Numerical Methods in Engineering 88 (2) (2011) 126–156.

[58] M. Taus, G. J. Rodin, T. J. Hughes, Isogeometric analysis of boundary integral equations: High-order collocation methods for the singular and hyper-singular equationsac, Mathematical Models and Methods in Applied Sciences pr 26 (08) (2016) 1447–1480.

[59] T. Takacs, B. Jüttler, Existence of stiffness matrix integrals for singularly parameterized domains in isogeometric analysis, Computer Methods in Applied Mechanics and Engineering 200 (49) (2011) 3568–3582.

[60] S.-M. Hu, Conversion between triangular and rectangular Bézier patches, Computer Aided Geometric Design 18 (7) (2001) 667–671.

[61] L. Yan, X. Han, J. Liang, Conversion between triangular Bézier patches and rectangular Bézier patches, Applied Mathematics and Computation 232 (2014) 469–478.

[62] S. T. Grilli, S. Vogelmann, P. Watts, Development of a 3D numerical wave tank for modeling tsunami generation by underwater landslides, Engineering Analysis with Boundary Elements 26 (4) (2002) 301–313.

[63] N. Mizutani, A. M. Mostafa, K. Iwata, Nonlinear regular wave, submerged breakwater and seabed dynamic interaction, Coastal Engineering 33 (2–3) (1998) 177–202.

[64] H. K. Johnson, T. V. Karambas, I. Avgeris, B. Zanuttigh, D. Gonzalez-Marco, I. Caceres, Modelling of waves and currents around submerged breakwaters, Coastal Engineering 52 (10–11) (2005) 949–969.

[65] S. Sun, G. Wu, Fully nonlinear simulation for fluid/structure impact: A review, Journal of Marine Science and Application 13 (3) (2014) 237–244.

[66] M. Au, C. Brebbia, Diffraction of water waves for vertical cylinders using boundary elements, Applied Mathematical Modelling 7 (2) (1983) 106–114.

[67] W. Koo, M. Kim, Numerical simulation of nonlinear wave and force generated by a wedge-shape wave maker, Ocean Engineering 33 (8-9) (2006) 983–1006.

[68] G. Ducrozet, F. Bonnefoy, D. L. Touzé, P. Ferrant, A modified High-Order Spectral method for wavemaker modeling in a numerical wave tank, European Journal of Mechanics - B/Fluids 34 (2012) 19 – 34.

[69] P. Ferrant, D. L. Touzé, K. Pelletier, Non-linear time-domain models for irregular wave diffraction about offshore structures, International Journal for Numerical Methods in Fluids 43 (2003) 1257–1277.

[70] S. Jeon, Y. Cho, M. Seo, J. Cho, W. Jeong, Dynamic response of floating substructure of spar-type offshore wind turbine with catenary mooring cables, Ocean Engineering 72 (2013) 356–364.

[71] T. Shivaji Ganesan, D. Sen, Time-domain simulation of large-amplitude wave–structure interactions by a 3D numerical tank approach, Journal of Ocean Engineering and Marine Energy 1 (3) (2015) 299–324.

[72] R. A. Watai, F. Ruggeri, C. M. P. Sampaio, A. N. Simos, Development of a time domain boundary element method for numerical analysis of floating bodies' responses in waves, Journal of the Brazilian Society of Mechanical Sciences and Engineering 37 (5) (2015) 1569–1589.

[73] W. Koo, M. Kim, D. Lee, S. Hong., Nonlinear time-domain simulation of pneumatic floating breakwater, International Journal of Offshore and Polar Engineering 16 (1) (2006) 25–32.

[74] M. S. Longuet-Higgins, E. D. Cokelet, The Deformation of Steep Surface Waves on Water. I. A Numerical Method of Computation, Proceedings of the Royal Society of London A: Mathematical, Physical and Engineering Sciences 350 (1660) (1976) 1–26.

[75] T. Nakayama, K. Washizu, The boundary element method applied to the analysis of two-dimensional nonlinear sloshing problems, International Journal for Numerical Methods in Engineering 17 (11) (1981) 1631–1646.

[76] T. Nakayama, Boundary element analysis of nonlinear water wave problems, International Journal for Numerical Methods in Engineering 19 (7) (1983) 953–970.

[77] D. Skyner, A comparison of numerical predictions and experimental measurements of the internal kinematics of a deep-water plunging wave, Journal of Fluid Mechanics 315 (1996) 51–64.

[78] S. Maiti, D. Sen, Computation of solitary waves during propagation and runup on a slope, Ocean Engineering 26 (11) (1999) 1063–1083.

[79] M. Abou-Dina, M. Helal, Boundary integral method applied to the transient, nonlinear wave propagation in a fluid with initial free surface elevation, Applied Mathematical Modelling 24 (8–9) (2000) 535–549.

[80] S. T. Grilli, J. Skourup, I. Svendsen, An efficient boundary element method for nonlinear water waves, Engineering Analysis with Boundary Elements 6 (2) (1989) 97–107.

[81] S. T. Grilli, I. A. Svendsen, Corner problems and global accuracy in the boundary element solution of nonlinear wave flows, Engineering Analysis with Boundary Elements 7 (4) (1990) 178–195.

[82] K. Tanizawa, The state of the art on numerical wave tank, Proceedings of the 4th Osaka Colloquium on seakeeping performance of ships (2000) 95–114.

[83] W. Bai, R. E. Taylor, Numerical simulation of fully nonlinear regular and focused wave diffraction around a vertical cylinder using domain decomposition, Applied Ocean Research 29 (1–2) (2007) 55–71.

[84] H. G. Sung, S. T. Grilli, BEM Computations of 3-D Fully Nonlinear Free-Surface Flows Caused by Advancing Surface Disturbances, International Journal of Offshore and Polar Engineering 18 (2008) 292–301.

[85] W. Bai, M. Hannan, K. Ang, Numerical simulation of fully nonlinear wave interaction with submerged structures: Fixed or subjected to constrained motion, Journal of Fluids and Structures 49 (2014) 534–553.

[86] G. Chen, C. Kharif, S. Zaleski, J. Li, Two-dimensional Navier–Stokes simulation of breaking waves, Physics of Fluids 11 (1) (1999) 121–133.

[87] S. Guignard, R. Marcer, V. Rey, C. Kharif, P. Fraunié, Solitary wave breaking on sloping beaches: 2-D two phase flow numerical simulation by SL-VOF method, European Journal of Mechanics - B/Fluids 20 (1) (2001) 57–74.

[88] I. Hadžić, J. Hennig, M. Perić, Y. Xing-Kaeding, Computation of flow-induced motion of floating bodies, Applied Mathematical Modelling 29 (12) (2005) 1196–1210.

[89] M. A. Rahman, N. Mizutani, K. Kawasaki, Numerical modeling of dynamic responses and mooring forces of submerged floating breakwater, Coastal Engineering 53 (10) (2006) 799–815.

[90] Y. Li, M. Lin, Regular and irregular wave impacts on floating body, Ocean Engineering 42 (2012) 93–101.

[91] A. Ghasemi, A. Pathak, M. Raessi, Computational simulation of the interactions between moving rigid bodies and incompressible two-fluid flows, Computers & Fluids 94 (2014) 1–13.

[92] H. G. Sung, H. S. Choi, Implicit formulation with the boundary element method for nonlinear radiation of water waves, Engineering Analysis with Boundary Elements 34 (5) (2010) 511–529.

[93] V. Mantic, A new formula for the C-matrix in the Somigliana identity, Journal of Elasticity 33 (3) (1993) 191–201.

[94] C. A. Brebbia, J. Domínguez, Boundary Elements: An Introductory Course, second edition Edition, WIT Press, Computational Mechanics, 1992.

[95] J. Lachat, J. Watson, Effective numerical treatment of boundary integral equations: A formulation for three-dimensional elastostatics, International Journal for Numerical Methods in Engineering 10 (5) (1976) 991–1005.

[96] C. Adam, T. Hughes, S. Bouabdallah, M. Zarroug, H. Maitournam, Selective and reduced numerical integrations for NURBS-based isogeometric analysis, Computer Methods in Applied Mechanics and Engineering 284 (2015) 732–761.

[97] G. Xie, J. Zhang, Y. Dong, C. Huang, G. Li, An improved exponential transformation for nearly singular boundary element integrals in elasticity problems, International Journal of Solids and Structures 51 (6) (2014) 1322–1329.

[98] G. Xie, F. Zhou, J. Zhang, X. Zheng, C. Huang, New variable transformations for evaluating nearly singular integrals in 3D boundary element method, Engineering Analysis with Boundary Elements 37 (9) (2013) 1169–1178.

[99] B. I. Yun, A generalized non-linear transformation for evaluating singular integrals, International Journal for Numerical Methods in Engineering 65 (12) (2006) 1947–1969.

[100] J. Telles, R. Oliveira, Third degree polynomial transformation for boundary element integrals: Further improvements, Engineering Analysis with Boundary Elements 13 (2) (1994) 135–141.

[101] X.-W. Gao, The radial integration method for evaluation of domain integrals with boundary-only discretization, Engineering Analysis with Boundary Elements 26 (10) (2002) 905–916.

[102] X.-W. Gao, An effective method for numerical evaluation of general 2D and 3D high order singular boundary integrals, Computer Methods in Applied Mechanics and Engineering 199 (45–48) (2010) 2856–2864.

[103] J. C. F. Telles, A self-adaptive co-ordinate transformation for efficient numerical evaluation of general boundary element integrals, International Journal for Numerical Methods in Engineering 24 (5) (1987) 959–973.

[104] J. Balaš, J. Sládek, V. Sládek, Stress Analysis by Boundary Element Methods, Vol. 23, Elsevier, 1989.

[105] A. Brancati, M. Aliabadi, I. Benedetti, Hierarchical adaptive cross approximation GMRES technique for solution of acoustic problems using the boundary element method, Computer Modeling in Engineering and Sciences 43 (2) (2009) 149–172.

[106] G. Wu, R. Taylor, The coupled finite element and boundary element analysis of nonlinear interactions between waves and bodies, Ocean Engineering 30 (3) (2003) 387–400.

[107] S. Boo, C. Kim, Fully nonlinear diffraction due to a vertical circular cylinder in a 3-D HOBEM numerical wave tank, Proceedings of the International Offshore and Polar Engineering Conference 3 (1996) 23–30.

[108] J. D. Fenton, A high-order cnoidal wave theory, Journal of Fluid Mechanics 94 (1979) 129–161.

[109] M. Rienecker, J. Fenton, A Fourier approximation method for steady water waves, J. Fluid Mech 104 (1981) 119–137.

[110] J. D. Fenton, A Fifth-Order Stokes Theory for Steady Waves, Journal of Waterway, Port, Coastal, and Ocean Engineering 111 (2) (1985) 216–234.

[111] S. R. Massel, Hydrodynamics of Coastal Zones, Vol. 48, Elsevier, 1989.

[112] M. Tanaka, The stability of solitary waves, Physics of Fluids 29 (3) (1986) 650–655.

[113] D. Dutykh, D. Clamond, Efficient computation of steady solitary gravity waves, Wave Motion 51 (1) (2014) 86–99.

[114] H. G. Sung, S. T. Grilli, Numerical modeling of Nonlinear Surface Waves caused by Surface Effect Ships Dynamics and Kinematics, Procedings of The Fifteenth International Offshore and Polar Engineering Conference (2005) 124–131.

[115] J. Wehausen, The Wave Resistance of Ships, Advances in Applied Mechanics 13 (C) (1973) 93–245.

[116] H. E. Guanghua, An iterative Rankine BEM for wave-making analysis of submerged and surface-piercing bodies in finite water depth, Journal of Hydrodynamics, Ser. B 25 (6) (2013) 839–847.

[117] P. Yulin, D. Xiaoxia, Z. Qiang, D. K. P. Yue, Boundary-element method for the prediction of performance of flapping foils with leading-edge separation, Journal of Fluid Mechanics 698 (2012) 446–467.

[118] B. Prasad, T. Hino, K. Suzuki, Numerical simulation of free surface flows around shallowly submerged hydrofoil by OpenFOAM, Ocean Engineering 102 (2015) 87–94.

[119] D. A. Andrews, P. S. Low, Role of red blood cells in thrombosis, Current opinion in hematology 6 (2) (1999) 76.

[120] S. Bansode, S. Banarjee, D. Gaikwad, S. Jadhav, R. Thorat, Microencapsulation: a review, International Journal of Pharmaceutical Sciences Review and Research 1 (2) (2010) 38–43.

[121] D. Barthès-Biesel, Motion of a spherical microcapsule freely suspended in a linear shear flow, Journal of Fluid Mechanics 100 (04) (1980) 831–853.

[122] D. Barthès-Biesel, J. Rallison, The time-dependent deformation of a capsule freely suspended in a linear shear flow, Journal of Fluid Mechanics 113 (1981) 251–267.

[123] P. Bagchi, P. C. Johnson, A. S. Popel, Computational fluid dynamic simulation of aggregation of deformable cells in a shear flow, Journal of biomechanical engineering 127 (7) (2005) 1070–1080.

[124] A. Kilimnik, W. Mao, A. Alexeev, Inertial migration of deformable capsules in channel flow, Physics of Fluids (1994-present) 23 (12) (2011) 123302.

[125] T. Gao, H. H. Hu, P. P. Castañeda, Rheology of a suspension of elastic particles in a viscous shear flow, Journal of Fluid Mechanics 687 (2011) 209.

[126] M. Villone, G. d'Avino, M. Hulsen, P. Maffettone, Dynamics of prolate spheroidal elastic particles in confined shear flow, Physical Review E 92 (6) (2015) 062303.

[127] K. Sugiyama, S. Ii, S. Takeuchi, S. Takagi, Y. Matsumoto, A full Eulerian finite difference approach for solving fluid–structure coupling problems, Journal of Computational Physics 230 (3) (2011) 596–627.

[128] C. D. Eggleton, A. S. Popel, Large deformation of red blood cell ghosts in a simple shear flow, Physics of Fluids (1994-present) 10 (8) (1998) 1834–1845.

[129] P. Bagchi, Mesoscale simulation of blood flow in small vessels, Biophysical journal 92 (6) (2007) 1858–1877.

[130] C. Song, S. J. Shin, H. J. Sung, K.-S. Chang, Dynamic fluid-structure interaction of an elastic capsule in a viscous shear flow at moderate Reynolds number, Journal of Fluids and Structures 27 (3) (2011) 438–455.

[131] W.-X. Huang, C. B. Chang, H. J. Sung, Three-dimensional simulation of elastic capsules in shear flow by the penalty immersed boundary method, Journal of Computational Physics 231 (8) (2012) 3340–3364.

[132] Y. Sui, Y.-T. Chew, P. Roy, H.-T. Low, A hybrid method to study flow-induced deformation of three-dimensional capsules, Journal of Computational Physics 227 (12) (2008) 6351–6371.

[133] R. M. MacMeccan, J. R. Clausen, G. P. Neitzel, C. K. Aidun, Simulating deformable particle suspensions using a coupled lattice-Boltzmann and finite-element method, Journal of Fluid Mechanics 618 (2009) 13–39.

[134] Y. Sui, X. Chen, Y. Chew, P. Roy, H. Low, Numerical simulation of capsule deformation in simple shear flow, Computers & Fluids 39 (2) (2010) 242–250.

[135] A. Leyrat-Maurin, D. Barthès-Biesel, Motion of a deformable capsule through a hyperbolic constriction, Journal of Fluid Mechanics 279 (1994) 135–163.

[136] C. Quéguiner, D. Barthès-Biesel, Axisymmetric motion of capsules through cylindrical channels, Journal of Fluid Mechanics 348 (1997) 349–376.

[137] A. Diaz, N. Pelekasis, D. Barthès-Biesel, Transient response of a capsule subjected to varying flow conditions: effect of internal fluid viscosity and membrane elasticity, Physics of Fluids (1994-present) 12 (5) (2000) 948–957.

[138] A. Diaz, D. Barthès-Biesel, Entrance of a bioartificial capsule in a pore, Computer Modeling in Engineering and Sciences 3 (3) (2001) 321–338.

[139] E. Lac, D. Barthès-Biesel, Deformation of a capsule in simple shear flow: effect of membrane prestress, Physics of Fluids (1994-present) 17 (7) (2005) 072105.

[140] W. Dodson III, P. Dimitrakopoulos, Spindles, cusps, and bifurcation for capsules in Stokes flow, Physical review letters 101 (20) (2008) 208102.

[141] W. Dodson, P. Dimitrakopoulos, Dynamics of strain-hardening and strain-softening capsules in strong planar extensional flows via an interfacial spectral boundary element algorithm for elastic membranes, Journal of Fluid Mechanics 641 (2009) 263–296.

[142] L. Zhu, J. Rabault, L. Brandt, The dynamics of a capsule in a wall-bounded oscillating shear flow, Physics of Fluids (1994-present) 27 (7) (2015) 071902.

[143] C. Rorai, A. Touchard, L. Zhu, L. Brandt, Motion of an elastic capsule in a constricted microchannel, The European Physical Journal E 38 (5) (2015) 1–13.

[144] P. Zarda, S. Chien, R. Skalak, Interaction of viscous incompressible fluid with an elastic body, Computational Methods for Fluid-Solid Interaction Problems (1977) 65–82.

[145] R. Skalak, A. Tozeren, R. Zarda, S. Chien, Strain energy function of red blood cell membranes, Biophysical Journal 13 (3) (1973) 245.

[146] R. Skalak, N. Ozkaya, T. C. Skalak, Biofluid mechanics, Annual review of fluid mechanics 21 (1) (1989) 167–200.

[147] G. Pieper, H. Rehage, D. Barthès-Biesel, Deformation of a capsule in a spinning drop apparatus, Journal of colloid and interface science 202 (2) (1998) 293–300.

[148] M. Carin, D. Barthès-Biesel, F. Edwards-Lévy, C. Postel, D. C. Andrei, Compression of biocompatible liquid-filled HSA-alginate capsules: Determination of the membrane mechanical properties, Biotechnology and bioengineering 82 (2) (2003) 207–212.

[149] M. Husmann, H. Rehage, E. Dhenin, D. Barthès-Biesel, Deformation and bursting of nonspherical polysiloxane microcapsules in a spinning-drop apparatus, Journal of colloid and interface science 282 (1) (2005) 109–119.

[150] C. Pozrikidis, Numerical simulation of the flow-induced deformation of red blood cells, Annals of Biomedical Engineering 31 (10) (2003) 1194–1205.

[151] H. Zhao, A. H. Isfahani, L. N. Olson, J. B. Freund, A spectral boundary integral method for flowing blood cells, Journal of Computational Physics 229 (10) (2010) 3726–3744.

[152] Z. Peng, R. J. Asaro, Q. Zhu, Multiscale simulation of erythrocyte membranes, Phys. Rev. E 81 (2010) 031904.

[153] Z. Peng, Y.-L. Chen, H. Lu, Z. Pan, H.-C. Chang, Mesoscale simulations of two model systems in biophysics: from red blood cells to DNAs, Computational Particle Mechanics 2 (4) (2015) 339–357.

[154] C. Dupont, A.-V. Salsac, D. Barthès-Biesel, M. Vidrascu, P. Le Tallec, Influence of bending resistance on the dynamics of a spherical capsule in shear flow, Physics of Fluids (1994-present) 27 (5) (2015) 051902.

[155] D. Barthès-Biesel, Motion and Deformation of Elastic Capsules and Vesicles in Flow, Annual Review of Fluid Mechanics 48 (2016) 25–52.

[156] E. Foessel, J. Walter, A.-V. Salsac, D. Barthès-Biesel, Influence of internal viscosity on the large deformation and buckling of a spherical capsule in a simple shear flow, Journal of Fluid Mechanics 672 (2011) 477–486.

[157] J. Walter, A.-V. Salsac, D. Barthès-Biesel, Ellipsoidal capsules in simple shear flow: prolate versus oblate initial shapes, Journal of Fluid Mechanics 676 (2011) 318–347.

[158] X.-Q. Hu, A.-V. Salsac, D. Barthès-Biesel, Flow of a spherical capsule in a pore with circular or square cross-section, Journal of Fluid Mechanics 705 (2012) 176–194.

[159] T. Omori, T. Ishikawa, Y. Imai, T. Yamaguchi, Membrane tension of red blood cells pairwisely interacting in simple shear flow, Journal of biomechanics 46 (3) (2013) 548–553.

[160] C. Dupont, F. Delahaye, A.-V. Salsac, D. Barthès-Biesel, Off-plane motion of an oblate capsule in a simple shear flow, Computer methods in biomechanics and biomedical engineering 16 (sup1) (2013) 4–5.

[161] S. K. Boey, D. H. Boal, D. E. Discher, Simulations of the erythrocyte cytoskeleton at large deformation. I. Microscopic models, Biophysical Journal 75 (3) (1998) 1573–1583.

[162] D. E. Discher, D. H. Boal, S. K. Boey, Simulations of the erythrocyte cytoskeleton at large deformation. II. Micropipette aspiration, Biophysical Journal 75 (3) (1998) 1584–1597.

[163] C. Pozrikidis, Numerical simulation of the flow-induced deformation of red blood cells, Annals of Biomedical Engineering 31 (10) (2003) 1194–1205.

[164] C. Pozrikidis, Numerical simulation of cell motion in tube flow, Annals of biomedical engineering 33 (2) (2005) 165–178.

[165] I. V. Pivkin, G. E. Karniadakis, Accurate coarse-grained modeling of red blood cells, Physical review letters 101 (11) (2008) 118105.

[166] D. A. Fedosov, B. Caswell, G. E. Karniadakis, A multiscale red blood cell model with accurate mechanics, rheology, and dynamics, Biophysical journal 98 (10) (2010) 2215–2225.

[167] H. Zhao, A. H. Isfahani, L. N. Olson, J. B. Freund, A spectral boundary integral method for flowing blood cells, Journal of Computational Physics 229 (10) (2010) 3726–3744.

[168] X. Li, Z. Peng, H. Lei, M. Dao, G. E. Karniadakis, Probing red blood cell mechanics, rheology and dynamics with a two-component multi-scale model, Phil. Trans. R. Soc. A 372 (2021) (2014) 20130389.

[169] D. Barthès-Biesel, A. Diaz, E. Dhenin, Effect of constitutive laws for two-dimensional membranes on flow-induced capsule deformation, Journal of Fluid Mechanics 460 (2002) 211–222.

[170] C. Pozrikidis, A practical guide to boundary element methods with the software library BEMLIB, CRC Press, 2002.

[171] C. Pozrikidis, Effect of membrane bending stiffness on the deformation of capsules in simple shear flow, Journal of Fluid Mechanics 440 (2001) 269–291.

[172] Y. Wang, P. Dimitrakopoulos, A three-dimensional spectral boundary element algorithm for interfacial dynamics in Stokes flow, Physics of Fluids (1994-present) 18 (8) (2006) 082106.

[173] A. Joneidi, C. Verhoosel, P. Anderson, Isogeometric boundary integral analysis of drops and inextensible membranes in isoviscous flow, Computers & Fluids 109 (2015) 49–66.

[174] A. T. Chwang, T. Y.-T. Wu, Hydromechanics of low-Reynolds-number flow. Part 2. Singularity method for Stokes flows, Journal of Fluid Mechanics 67 (04) (1975) 787–815.

[175] B. Bentley, L. Leal, An experimental investigation of drop deformation and breakup in steady, two-dimensional linear flows, Journal of Fluid Mechanics 167 (1986) 241–283.

[176] J. R. Womersley, Method for the calculation of velocity, rate of flow and viscous drag in arteries when the pressure gradient is known, The Journal of physiology 127 (3) (1955) 553.

[177] X.-Q. Hu, A.-V. Salsac, D. Barthès-Biesel, Flow of a spherical capsule in a pore with circular or square cross-section, Journal of Fluid Mechanics 705 (2012) 176–194.

[178] H. Goldsmith, Red cell motions and wall interactions in tube flow., in: Federation Proceedings, Vol. 30, 1971, pp. 1578–1590.

[179] A. Helmy, D. Barthès-Biesel, Migration of a spherical capsule freely suspended in an unbounded parabolic flow, Journal de Mécanique théorique et appliquée 1 (5) (1982) 859–880.

[180] G. Coupier, B. Kaoui, T. Podgorski, C. Misbah, Noninertial lateral migration of vesicles in bounded Poiseuille flow, Physics of Fluids (1994-present) 20 (11) (2008) 111702.

[181] S. K. Doddi, P. Bagchi, Lateral migration of a capsule in a plane Poiseuille flow in a channel, International Journal of Multiphase Flow 34 (10) (2008) 966–986.

[182] L. Shi, T.-W. Pan, R. Glowinski, Numerical simulation of lateral migration of red blood cells in Poiseuille flows, International Journal for Numerical Methods in Fluids 68 (11) (2012) 1393–1408.

[183] R. K. Singh, X. Li, K. Sarkar, Lateral migration of a capsule in plane shear near a wall, Journal of Fluid Mechanics 739 (2014) 421–443.

[184] T. Greenstein, J. Happel, Theoretical study of the slow motion of a sphere and a fluid in a cylindrical tube, Journal of Fluid Mechanics 34 (04) (1968) 705–710.

[185] H. Brenner, Pressure drop due to the motion of neutrally buoyant particles in duct flows, Journal of Fluid Mechanics 43 (04) (1970) 641–660.

[186] D. R. Forsey, R. H. Bartels, Hierarchical B-spline refinement, Computer Graphics (ACM) 22 (4) (1988) 205–212.

[187] P. Hennig, S. Müller, M. Kästner, Bézier extraction and adaptive refinement of truncated hierarchical NURBS, Computer Methods in Applied Mechanics and Engineering 305 (2016) 316–339.

[188] E. Evans, M. Scott, X. Li, D. Thomas, Hierarchical T-splines: Analysis-suitability, Bézier extraction, and application as an adaptive basis for isogeometric analysis, Computer Methods in Applied Mechanics and Engineering 284 (2014) 1–20.

[189] S.-M. Hu, Conversion of a triangular Bézier patch into three rectangular Bézier patches, Computer Aided Geometric Design 13 (3) (1996) 219–226.

UNIVERSITAT ROVIRA I VIRGILI
TOWARDS THE APPLICATION OF THE ISOGEOMETRIC BOUNDARY ELEMENT ANALYSIS TO FLUID MECHANICS:
NON-LINEAR GRAVITY WAVES AND DYNAMICS OF DEFORMABLE CAPSULES IN SHEAR FLOWS
Jorge Maestre Heredia

UNIVERSITAT ROVIRA I VIRGILI
TOWARDS THE APPLICATION OF THE ISOGEOMETRIC BOUNDARY ELEMENT ANALYSIS TO FLUID MECHANICS:
NON-LINEAR GRAVITY WAVES AND DYNAMICS OF DEFORMABLE CAPSULES IN SHEAR FLOWS
Jorge Maestre Heredia

UNIVERSITAT ROVIRA I VIRGILI
TOWARDS THE APPLICATION OF THE ISOGEOMETRIC BOUNDARY ELEMENT ANALYSIS TO FLUID MECHANICS:
NON-LINEAR GRAVITY WAVES AND DYNAMICS OF DEFORMABLE CAPSULES IN SHEAR FLOWS
Jorge Maestre Heredia

UNIVERSITAT
ROVIRA i VIRGILI